Novel aspects of electromagnetic radiation in isotropic and anisotropic media

A Thesis

by

Nilamoni Daloi
Reg. no. 166121016

Supervisor:
Prof. Tarak Nath Dey

Submitted in partial fulfilment of the requirements for the award of

Doctor of Philosophy

Department of Physics
Indian Institute of Technology Guwahati

July 2022

Dedication

Dedicated

to

my family

Declaration

I hereby declare that the contents of this thesis are original and have not been submitted for consideration for any other degree or qualification in this, or any other university. This dissertation is my own work and contains nothing which is the outcome of work done by others, except for the collaboration as specified in the text and acknowledgments.

Nilamoni Daloi
July 2022

Certificate

This is to certify that the work contained in the thesis entitled "**Novel aspects of electromagnetic radiation in isotropic and anisotropic media**" submitted by Nilamoni Daloi in the partial fulfillment of the requirement for the award of the degree of Doctor of Philosophy in Physics, Department of Physics, Indian Institute of Technology Guwahati, is a record of the candidate's own work carried out by him under my supervision and guidance. The matter embodied in this report has not been submitted in part or full to any other university or institute for the award of any degree.

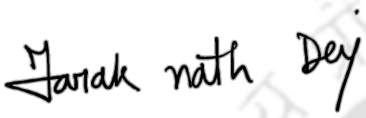

Dr. Tarak Nath Dey
Professor
Department of Physics
Indian Institute of Technology Guwahati
Guwahati - 781039
Assam, India.

Acknowledgment

I would like to express my sincere gratitude to my supervisor, Prof. Tarak Nath Dey for his constructive criticism, guidance and encouragement in completing the research work in this thesis.

I would like to thank my doctoral committee members, Dr. Kanhaiya Pandey, Dr. Soumitra Nandi and Dr. Ashok Kuman Dasmahapatra for their insightful comments and suggestion during my review seminars.

I thank Dr. Pardeep Kumar, Max Planck Institute for the Science of Light, Staudtstrasse 2, 91058 Erlangen, Germany, for a wonderful collaboration in one of my research work.

I take this opportunity to sincerely acknowledge the financial assistance from MHRD which helped me in completing my research work successfully.

I thank my seniors Dr. Sandeep Sharma and Dr. Nawaz Sarif Mallick for their insightful comments and suggestions on different topics related to my research work. I would also like to thank my junior Partha Das, Samit Kumar Hazra, and Sanket Das for their fruitful discussions. I thank all my batch mates Ritupan Borah, Apurba Das, Dangka Shylla, and Abhilasha Bora, for their encouragement and entertaining company during my Ph.D. period.

Lastly I am greatly indebted to my parents, my cousin sister Sneha Baro and my friend Sagar Dutta for their constant support and encouragement throughout this period. Without their support and encouragement, this work would not have been possible.

Abstract

The study of light-atom interaction has led to many novel discoveries, having applications in a wide range of areas such as biophysics, microscopy, optical communication, quantum computing, and fundamental physics research. It is well known from quantum physics that atoms possess various quantized energy states or levels. These atomic states can be coupled with a coherent electromagnetic field (light) such as lasers. This coupling gives rise to a quantity known as the "*atomic coherence*" in the literature. The atomic coherence can be manipulated by changing parameters such as the laser frequency, intensity, and temperature of the atomic vapor. By controlling the atomic coherence, it is possible to change the medium's optical properties such as refractive index, absorption, isotropy, anisotropy, and group velocity of a pulse inside the medium, etc. One of the popular phenomenon associated with light-atom interaction is the *Electromagnetically induced transparency* (EIT); first proposed by Harris *et al.* in 1990. In EIT, a three-level atomic level configuration is driven by a weak probe field and another strong field called the control field. The two fields couple two different transitions of the three-level system with a common higher energy atomic state, giving it an appearance of the Greek alphabet, Λ. The atomic coherences generated between the different transition pathways of the three-level configuration can interfere destructively, under appropriate parameters. This renders the medium transparent for the probe field within a narrow spectral range near the resonance of the probe transition. The narrow transparency window is accompanied by strong dispersion which can be used to produce "*slow light*" *i.e.*, reduction of light's velocity inside the medium. Additionally, a light pulse can also be stored and retrieved in an EIT system by exploiting the atomic coherence. In this thesis, we have formulated four research problems based on the the concepts of EIT and atomic coherence. The first two problems are concerned with pulse amplification and the rest two are related to waveguiding and polarization manipulation of optical beams inside atomic vapor medium.

This thesis consists of mainly six chapters. In chapter 1, we briefly discuss the theoretical formalism of light-matter interaction used in this thesis. Throughout the thesis we have used, what is known as a "*semiclassical*" theory of light-matter interaction. In this framework, atoms are treated as "*quantum mechanical*" entities whereas light is considered "*classical*". The dynamical properties of atomic coherence and atomic population in different quantum mechanical states are studied using the well known "*density matrix*" analysis. The spatio-temporal evolution of the electromagnetic fields are studied using "*Maxwell-Bloch*" equations which is a merger of the Maxwell's equations with atomic coherences appearing in the density matrix formalism. Later in this chapter we provide the theory of light interacting with a two and three-level atomic media, describing some of the relevant associated phenomena. Finally we provide an introduction to vector beams, their salient features, and applications.

In chapter 2, we propose a shape preserving pulse amplification scheme in atomic vapor medium. We use a three-level Λ type atomic system which under appropriate condition can cause pulse amplification and enable distortion free pulse propagation posterior to the amplification. The whole process has been explained using the density matrix formalism, discussed in chapter 1.

In chapter 3, we investigate a similar pulse amplification scheme, but with polar

molecules instead of atoms. We show that, with an appropriate molecular level system, the permanent dipole moments (PDMs) in polar molecules can be leveraged to amplify pulses in the Infrared region. In addition, it has been shown that presence of PDMs leads to something called as "*multiphoton*" excitation which are otherwise forbidden. A multi-photon transition is the one where a transition between two molecular energy states, $|i\rangle$ and $|j\rangle$ can be coupled by a laser of frequency, say ω_{ij}/n. Here, n is an integer, and ω_{ij} is frequency separation between states, $|i\rangle$ and $|j\rangle$. We call it a one-photon transition when $n = 1$, and two-photon when $n = 2$. We show that this enables amplification of pulses with the aid of a continuous wave field (field constant in time) whose frequency is half of the carrier frequency of the pulse.

In chapter 4, we segue to a different research area dealing with "*vector beams*" and illustrate how atomic coherence can be used for manipulating the polarization and propagation aspects of a vector beam. Vector beams (VBs) are a special kind of beams that have a nonuniform polarization distribution on their transverse plane. Vector beams exhibit some interesting properties *e.g.*, a class of VBs known as cylindrical VB, can generate a strong longitudinal field component at the focus of a high numerical aperture lens, producing a very small spot size. This focusing property has applications in microscopy, laser cutting and optical trapping of particles. Our work is concentrated on the nonuniform polarization distribution of VBs, which can be used for polarization-based measurements. In such scenarios, it would be preferable to have a controllable rotation of the VB's transverse polarization structure. In this chapter we propose a scheme to dynamically control the polarization rotation of a VB using a four level tripod shaped atomic level system. The proposed method enables polarization rotation control at any given propagation length with minimum absorption.

In chapter 5, we discusses a scheme to guide a vector beam using optically written waveguides in atomic vapor medium. The concept of "*optically written waveguides*" in atomic media was first experimentally demonstrated by Truscott *et al.* [Phys. Rev. Lett. **82**, 1438 (1999)]. Since then it has been studied for achieving diffraction free propagation and image resolution enhancement. In this work, we theoretically show that a VB can be guided for a comparatively longer distance, inside a four level tripod atomic system in presence of a strong zeroth-order Bessel beam. The atomic coherence associated with the Bessel beam creates a radially outward core-cladding type refractive index gradient on the VB's transverse plane. This refractive index gradient remains constant throughout the atomic vapor medium, due to the non-diffracting property of Bessel beams, enabling VB guiding.

In chapter 6, we provide the conclusion of this thesis along with future prospective of related research work.

Contents

List of Figures

List of Tables

Chapter 1

Introduction

One of the earliest theories of light was developed by Sir Isaac Newton and is known as the "*corpuscular theory*". According to this theory, the reflection and refraction of light are due to light being made of particles known as "*corpuscles*". However, the corpuscular theory could not explain polarization, diffraction, and interference of light. Later, Thomas Young proved experimentally that light is indeed a wave and developed the wave theory of light. Eventually, James Clerk Maxwell mathematically formulated the earliest form of what is now known as the "*Maxwell's equations*", suggesting light is a propagating wave of oscillating electric and magnetic fields, also called Electromagnetic (EM) radiation. Maxwell's formalism is now referred to as the classical theory of light. The particle nature of light re-emerged when Einstein explained the famous "*photoelectric effect*" by considering light to be made of particles called "*photons*" with discrete energy that is proportional to the frequency of light. For the first two decades of the 20^{th} century, the dual nature of light was not clearly understood. It was the advent of quantum mechanics that commenced the development of a theory explaining the particle nature of light. In the late 1920s and 30s, Paul Dirac [1], Werner Heisenberg, Wolfgang Pauli, and others laid down the foundations for a quantum mechanical theory of light and its interaction with matter. Presently, a fully developed quantum mechanical theory of light is known as "*quantum electrodynamics*" (QED), developed by Richard Feynman [2], Julian S. Schwinger, and Tomonaga Shin'ichirō, who were jointly awarded the 1965 Nobel prize in physics for their contributions to QED.

In essence, the quantum mechanical version of light considers each mode of the EM wave as a quantized simple harmonic oscillator. This approach could explain phenomena such as spontaneous emission [3], Lamb shift [3], and Casimir effect [4] etc.. Also, vacuum fluctuations or zero point energy which are energy fluctuations at absolute zero temperature can only be explained through the quantization of light. Furthermore, without going into details, the existence of non-classical states of light such as squeezed states, sub-Poissonian photon statistics, strongly support the quantization of light. The study of quantized light [5, 6] interacting with atoms and molecules is now popularly known as "*quantum optics*" [3, 7, 8].

In this thesis we have opted for the classical description of light, *i.e.*, we treat light as EM waves satisfying the Maxwell's equations. The atoms interacting with light are however considered to be quantum mechanical, having discrete energy levels. This formalism is known as the "*semiclassical*" [3] theory of light-matter interaction and suffices to explain many well known phenomena in quantum optics. One of such

phenomena is "*Electromagnetically induced transparency*" (EIT) which is discussed in detail, later in this chapter.

This chapter is dedicated to the semiclassical theory of light-matter interaction. We start with the derivation of the EM wave propagation equation through atomic vapor. We then discuss light-atom interaction followed by the "*density matrix*" formalism; a robust mathematical tool for studying the dynamics of light-matter interaction. After that we explain the interaction of a two, three-level atomic system, with light using the density matrix formalism. Lastly, we provide an introduction to vector beams, their generation, and applications.

1.1 Propagation Equation

The propagation of light through an optical medium can be described by the four fundamental Maxwell's equations [9]. The Maxwell's equations in Gaussian units are written as:

$$\vec{\nabla} \cdot \vec{D} = 4\pi\varrho, \qquad \text{(Gauss's Law)} \tag{1.1a}$$

$$\vec{\nabla} \cdot \vec{B} = 0, \tag{1.1b}$$

$$\vec{\nabla} \times \vec{E} = -\frac{1}{c}\frac{\partial \vec{B}}{\partial t}, \qquad \text{(Faraday's Law)} \tag{1.1c}$$

$$\vec{\nabla} \times \vec{H} = \frac{4\pi}{c}\vec{J} + \frac{1}{c}\frac{\partial \vec{D}}{\partial t}, \qquad \text{(Ampere's Law).} \tag{1.1d}$$

We have adopted Gaussian units throughout this thesis considering the symmetry properties and physical usefulness. In the above equations, $\vec{E}$, $\vec{H}$ represent the electric and magnetic field vectors at a given point in space and time, $(\vec{r}, t)$, c is the speed of light in free space, and ϱ, $\vec{J}$ represent the free charge density and current density, respectively. The electric displacement, $\vec{D}$ and the magnetic induction, $\vec{B}$ are related by the equations:

$$\vec{D} = \vec{E} + 4\pi\vec{P}, \tag{1.2a}$$

$$\vec{B} = \vec{H} + 4\pi\vec{\mathcal{M}}, \tag{1.2b}$$

where $\vec{P}$ and $\vec{\mathcal{M}}$ are the electric and magnetic polarization of the medium, respectively. In free space, both $\vec{P}$ and $\vec{\mathcal{M}}$ are zero. In this thesis, we have assumed a non-magnetic ($\vec{\mathcal{M}} = 0$), and non-conducting ($\vec{J} = 0$) medium with no free charge ($\varrho = 0$). We now present a brief derivation of the relevant EM wave propagation equations used in this thesis:

Taking the curl of Eq. (1.1c), and using Eqs. (1.1d), (1.2b) we obtain,

$$\vec{\nabla} \times \left(\vec{\nabla} \times \vec{E}\right) + \frac{1}{c^2}\frac{\partial^2}{\partial t^2}(\vec{E} + 4\pi\vec{P}) = 0. \tag{1.3}$$

Using the identity, $\vec{\nabla} \times (\vec{\nabla} \times \vec{A}) = \vec{\nabla}(\vec{\nabla} \cdot \vec{A}) - \nabla^2\vec{A}$, we get, $\vec{\nabla} \times \left(\vec{\nabla} \times \vec{E}\right) = \vec{\nabla}(\vec{\nabla}\cdot\vec{E}) - \nabla^2\vec{E}$. For a charge free isotropic medium, it can be shown that, $\vec{\nabla}\cdot\vec{E} = 0$. Therefore, Eq. (1.3) can be written as:

$$\vec{\nabla}^2\vec{E} - \frac{1}{c^2}\frac{\partial^2\vec{E}}{\partial t^2} = \frac{4\pi}{c^2}\frac{\partial^2\vec{P}}{\partial t^2}. \tag{1.4}$$

The above equation is the Maxwell's equation of EM wave propagation through a dielectric medium. The term on the right hand side of Eq. (1.4) is the source term with $\vec{P}$ being the polarization induced by the electric field, $\vec{E}$ inside the medium. In practice, it is difficult to find analytical solutions of Eq. (1.4). Hence, Eq. (1.4) is solved numerically after simplifying it using certain approximations, discussed below. Let us consider a quasi-monochromatic (having a single frequency) wave propagating along the z-direction inside a dielectric medium. The electric field and corresponding polarization of such a wave can be written as:

$$\vec{E}(x,y,z,t) = \hat{e}\mathcal{E}(x,y,z,t)e^{-i(\omega t - kz)} + \text{c.c.}, \tag{1.5a}$$

$$\vec{P}(x,y,z,t) = \hat{e}\mathcal{P}(x,y,z,t)e^{-i(\omega t - kz)} + \text{c.c.}, \tag{1.5b}$$

where, "c.c." stands for complex conjugate, $\hat{e}$ is unit polarization vector, ω is the carrier angular frequency of the field, $k = \omega/c$, is the wave number and $\mathcal{E}(\mathcal{P})$ is the envelope functions of the field (polarization). The relevant derivatives of electric field and polarization from Eq. (1.5) are:

$$\nabla^2\vec{E} = \hat{e}\left(\nabla_\perp^2\mathcal{E} + \frac{\partial^2\mathcal{E}}{\partial z^2} + 2ik\frac{\partial\mathcal{E}}{\partial z} - k^2\mathcal{E}\right)e^{i(kz-\omega t)} + \text{c.c.}, \tag{1.6a}$$

$$\frac{\partial^2\vec{E}}{\partial t^2} = \hat{e}\left(\frac{\partial^2\mathcal{E}}{\partial t^2} - 2i\omega\frac{\partial\mathcal{E}}{\partial t} - \omega^2\mathcal{E}\right)e^{i(kz-\omega t)} + \text{c.c.}, \tag{1.6b}$$

$$\frac{\partial^2\vec{P}}{\partial t^2} = \hat{e}\left(\frac{\partial^2\mathcal{P}}{\partial t^2} - 2i\omega\frac{\partial\mathcal{P}}{\partial t} - \omega^2\mathcal{P}\right)e^{i(kz-\omega t)} + \text{c.c.}, \tag{1.6c}$$

where $\nabla_\perp^2 = \partial^2/\partial x^2 + \partial^2/\partial y^2$ represents the spatial derivative in transverse direction. We then assume that the variation of the envelope functions $\mathcal{E}$ and $\mathcal{P}$ in space and time within the time period and wavelength are very slow. This assumption is called the "*slowly varying envelope approximation*" (SVEA) and is mathematically written as:

$$|k\mathcal{E}| \gg \left|k^2\frac{\partial\mathcal{E}}{\partial z}\right| \gg \left|\frac{\partial\mathcal{E}^2}{\partial^2 z}\right|, \quad |\omega\mathcal{E}| \gg \left|\omega^2\frac{\partial\mathcal{E}}{\partial t}\right| \gg \left|\frac{\partial\mathcal{E}^2}{\partial^2 t}\right|, \tag{1.7a}$$

$$|k\mathcal{P}| \gg \left|k^2\frac{\partial\mathcal{P}}{\partial z}\right| \gg \left|\frac{\partial\mathcal{P}^2}{\partial^2 z}\right|, \quad |\omega\mathcal{P}| \gg \left|\omega^2\frac{\partial\mathcal{P}}{\partial t}\right| \gg \left|\frac{\partial\mathcal{P}^2}{\partial^2 t}\right|. \tag{1.7b}$$

Substituting the above equations in Eq. (1.4) and neglecting the higher order time and space derivative we get:

$$\frac{1}{2ik}\nabla_\perp^2\mathcal{E} + \frac{\partial\mathcal{E}}{\partial z} + \frac{1}{c}\frac{\partial\mathcal{E}}{\partial t} = 2\pi ik\mathcal{P}. \tag{1.8}$$

For ease of numerical integration, the above equation is further simplified by considering a frame of reference moving at the speed of light in vacuum, c. The necessary coordinate transformation equations for that are:

$$\tau = t - z/c, \quad \zeta = z, \tag{1.9}$$

so that

$$\partial/\partial z + c^{-1}\partial/\partial t = \partial/\partial\zeta, \quad \partial/\partial t = \partial/\partial\tau. \tag{1.10}$$

Substituting the above equation in Eq. (1.8) we get,

$$\frac{1}{2ik}\nabla_{\perp}^{2}\mathcal{E} + \frac{\partial \mathcal{E}}{\partial \zeta} = 2\pi ik\mathcal{P}. \tag{1.11}$$

The above wave equation is known as the inhomogeneous "*paraxial Helmholtz equation*" [10] and is the most common equation for studying the propagation of laser beam. The first term on the left hand side of the equation describes the diffraction of the beam. A field of laser beam is also called a "*continuous wave*" (CW) field due to the fact that, $\partial\mathcal{E}/\partial t = 0$. For a laser pulse, the transverse spatial variation of the laser pulse is often considered to be small, *i.e.*, $\nabla_{\perp}^{2}\mathcal{E} \approx 0$ such that, Eq. (1.11) becomes,

$$\frac{\partial \mathcal{E}}{\partial \zeta} = 2\pi ik\mathcal{P}. \tag{1.12}$$

The spatio-temporal evolution of the induced polarization, $\mathcal{P}$ will be discussed in the subsequent sections with the introduction of the density matrix formalism.

1.2 Induced polarization of the medium

Atoms of can be visualized as a cloud of electrons with charge $-q$, surrounding the nucleus with charge, $+q$, thus making the atom neutral. In absence of any external force, the center of masses of the positive and negative charges coincide with each other. But upon application of an external electric field, $\vec{E}$ with moderate to small amplitude; the positive and negative charges are pulled apart by the equal and opposite electric force. At some equilibrium separation, say r_e, the attractive force between the positive and negative charge centers become equal to the force exerted by the external electric field. Thus creating an induced dipole moment, $\vec{d} = q\vec{r}_e$. The induced dipole moment and $\vec{E}$ are related by a proportionality constant as,

$$\vec{d} = \alpha\vec{E}, \tag{1.13}$$

where, α is called the "*atomic polarizability*". Due to the symmetric nature of atoms, $\vec{d}$ and $\vec{E}$ have same direction. But in case of molecules, if $\vec{E}$ is applied at an angle to the symmetry axis of the molecule, then $\vec{d}$ and $\vec{E}$ will have different directions. Thus, the generalized version of Eq. (1.13) is, $d_i = \sum_{j=1}^{3}\alpha_{i,j}E_j$ $(i = 1, 2, 3)$. If we assume all atoms to be identical and non interacting then the macroscopic induced polarization, $\vec{P}$ inside a homogeneous medium of atomic vapor, is given as

$$\vec{P} = \mathcal{N}\vec{d}, \tag{1.14}$$

where $\mathcal{N}$ denotes the number of atoms per unit volume.

We consider the external electric field, $\vec{E}$ to have a very small amplitude. Under this condition, the interaction of electrons with $\vec{E}$ is very weak compared to the strong electrostatic interaction between the nucleus and electrons of the atom. Hence, the interaction of an atom with the external electric field can be studied as a perturbation, *i.e.*, the induced polarization can written as a Taylor series, in powers of the applied electric field, $\vec{E}$:

$$P_i(x,y,z,t) = P_i\Big|_{E=0} + \sum_j \left(\frac{\partial P_i}{\partial E_j}\right)\Big|_{E=0} E_j + \frac{1}{2!}\sum_{j,k}\left(\frac{\partial^2 P_i}{\partial E_j \partial E_k}\right)\Big|_{E=0} E_j E_k + \cdots . \tag{1.15}$$

The indices in the above equation represent the Cartesian coordinates. The first term in Eq. (1.15) represents the permanent dipole moment, which is zero for atoms but nonzero for polar molecules. The second term represents the induced linear polarization. The round bracketed coefficient in the second term of Eq. (1.15) is called the linear susceptibility of the atomic medium. The third term and above generate the nonlinear susceptibility of the medium. These higher-order terms become relevant at high amplitudes of $\vec{E}$. The study of higher-order susceptibility comes under the subject of "*nonlinear optics*" [11]. In this chapter, we will limit our discussion to small amplitudes of $\vec{E}$.

For small amplitude of the external electric field, $\vec{E}$, the macroscopic polarization can be studied using "*linear response theory*", according to which the induced polarization can then be written as

$$P_i(\vec{r},t) = \sum_j \int_{-\infty}^{t} dt' \chi_{i,j}(t-t') E_j(\vec{r},t'), \tag{1.16}$$

where $\chi_{i,j}$ is rank two tensor, representing the linear response or susceptibility of an anisotropic medium. For an anisotropic medium, the medium properties are dependent on the direction of observation. Here, $\chi_{i,j}(t-t')$ gives the contribution to the polarization produced at time, t by an electric field applied at an earlier time, t'. For simplicity, let us consider an isotropic medium (medium whose properties are direction independent), such that $\chi_{i,j} \equiv \chi$, is a scalar quantity. Thus, Eq. (1.16) can be written as:

$$\begin{aligned} \vec{P}(\vec{r},t) &= \int_{-\infty}^{t} dt' \chi(t-t') \vec{E}(\vec{r},t'), \\ &= \int_{0}^{\infty} d\tau \chi(\tau) \vec{E}(\vec{r},t-\tau). \quad \text{(Substituting, } t-t'=\tau) \end{aligned} \tag{1.17}$$

In writing Eq. (1.17), the lower limit of $\tau = t - t'$ is kept at zero to ensure the causality condition, $\chi_{i,j}(\tau) = 0$ for $\tau = t - t' < 0$, (*i.e.*, $t < t'$). This condition expresses the fact that $\vec{P}(\vec{r},t)$ depends only on past and not on future values of $\vec{E}(\vec{r},t)$. Writing $\vec{E}(\vec{r},t-\tau)$ and $\vec{P}(\vec{r},t)$ in terms of their Fourier transforms:

$$\vec{E}(\vec{r},t-\tau) = \int_{-\infty}^{\infty} E(r,\omega) e^{-i\omega(t-\tau)} d\omega, \quad \vec{P}(\vec{r},t) = \int_{-\infty}^{\infty} \vec{P}(\vec{r},\omega) e^{-i\omega t} d\omega, \tag{1.18}$$

and substituting Eq. (1.18) in Eq. (1.17) we get,

$$\begin{aligned} \int_{-\infty}^{\infty} \vec{P}(\vec{r},\omega) e^{-i\omega t} d\omega &= \int_{0}^{\infty} d\tau \chi(\tau) E(r,\omega) e^{-i\omega(t-\tau)} d\omega, \\ \implies \int_{-\infty}^{\infty} \vec{P}(\vec{r},\omega) e^{-i\omega t} d\omega &= \int_{-\infty}^{\infty} d\omega \int_{0}^{\infty} d\tau \chi(\tau) e^{i\omega\tau} E(r,\omega) e^{-i\omega t} d\omega. \end{aligned} \tag{1.19}$$

In Eq. (1.19), the equality must be maintained for each frequency ω, thus we can eliminate the integral sign on both sides to get

$$\vec{P}(\vec{r},\omega) = \chi(\omega) \vec{E}(\vec{r},\omega), \tag{1.20}$$

where

$$\chi(\omega) = \int_{0}^{\infty} d\tau \chi(\tau) e^{i\omega\tau}. \tag{1.21}$$

The susceptibility or response, $\chi(\tau)$ is a measurable quantity, *i.e.,* it must be a real number. Therefore, Eq. (1.21), can be written as,

$$\begin{aligned}\chi(\omega) &= \int_0^\infty \chi(\tau)\cos(\omega\tau)d\tau + i\int_0^\infty \chi(\tau)\sin(\omega\tau)d\tau, \\ &= \chi'(\omega) + i\chi''(\omega),\end{aligned} \tag{1.22}$$

where, χ', χ'' represent the real and imaginary parts of $\chi(\omega)$, respectively. The imaginary part of susceptibility, $\chi''(\omega)$ is called the dissipative or absorptive part of the response function and represent absorption of the incident electric field at frequency ω. It is also known as the spectrum of the response function. The real part of susceptibility, $\chi'(\omega)$ is called the reactive part of the response function and represents the refractive index of the medium.

In the steady state limit, Eq.(1.12) is written as:

$$\frac{\partial \mathcal{E}}{\partial z} = 2\pi i k \chi \mathcal{E}. \tag{1.23}$$

where $\mathcal{P} = \chi(\omega)\mathcal{E}$ is the linear response of the medium to the electric field. The solution for the above equation at a propagation length, L can be written as:

$$\begin{aligned}\vec{E}_{\text{out}}(z=L,t) &= \hat{e}\mathcal{E}(z=0)e^{2\pi i k L\chi}e^{-i(\omega t - kL)} + \text{c.c.}, \\ &= \hat{e}\mathcal{E}_0 e^{ikL(1+2\pi\chi')}e^{-2\pi k\chi'' L}e^{-i\omega t} + \text{c.c.}, \\ &= \hat{e}\mathcal{E}_0 e^{ikLn(\omega)}e^{-2\pi k\chi'' L}e^{-i\omega t} + \text{c.c.}.\end{aligned} \tag{1.24}$$

Where $\mathcal{E}_0$ is the field amplitude. In the optical frequency spectrum, $\chi \ll 1$, and refractive index, $n(\omega)$ can be written as:

$$n(\omega) = 1 + 2\pi \text{Re}[\chi(\omega)], \tag{1.25}$$

The field intensity is given by, $I_{\text{out}} \equiv |\vec{E}_{\text{out}}|^2$. Therefore the absolute square of Eq. (1.24) gives Beer's Law for the intensity

$$I_{\text{out}} = I_0 e^{-\alpha L}, \tag{1.26}$$

where α is the absorption coefficient (absorption per unit length)

$$\alpha(\omega) = 4\pi k \text{Im}[\chi(\omega)]. \tag{1.27}$$

1.3 Atom-field interaction Hamiltonian

In this section, we provide the theoretical formalism for studying the interaction of an atom with light. Experiments in quantum optics typically involve studying the interaction of lasers with an atomic vapor of alkali metals, *e.g.* rubidium-87. All Alkali metals have a single valence electron in the s-orbital which, being at a large distance from the nucleus, experiences the least Coulomb force. The loosely held single valence electron, together with the nucleus of alkali metal atoms can be modeled after the hydrogen atom. In presence of an external EM field, the nucleus being heavy, remains stationary inside the atom, while the orbitals of the valence electron are deformed, inducing a dipole moment. Thus to explain the interaction of

an alkali atom with EM field, it is sufficient to study the interaction of their single valence electron with the EM field. We shall now derive the interaction Hamiltonian of an atom inside EM field.

We first consider the motion of an isolated electron with charge, $-e$ and mass, m inside an EM field. From classical theory of electromagnetism, the electric field, $\vec{E}$ and magnetic field, $\vec{B}$ associated with an EM field can be expressed in terms of the scalar and vector potentials $\Phi(\vec{r},t)$ and $\vec{A}(\vec{r},t)$, respectively as:

$$\vec{E}(\vec{r},t) = -\vec{\nabla}\Phi(\vec{r},t) - \frac{1}{c}\frac{\partial}{\partial t}\vec{A}(\vec{r},t), \tag{1.28}$$

$$\vec{B}(\vec{r},t) = \vec{\nabla} \times \vec{A}(\vec{r},t), \tag{1.29}$$

Substituting the above equations in the Lorentz force experienced by the electron, $\vec{F} = -e[\vec{E} + (\vec{V} \times \vec{B})/c]$ and comparing it with the classical Lagrange's equation, the electron-field interaction Hamiltonian can be written as:

$$\mathcal{H}' = \frac{1}{2m}\left[\vec{p} + \frac{e}{c}\vec{A}(\vec{r},t)\right]^2 - e\Phi(\vec{r},t), \tag{1.30}$$

where, $\vec{p}$ is the mechanical linear momentum of the electron. Now, the valence electron inside the atom is also under the influence of a Coulomb interaction potential due to the nucleus. Hence the total Hamiltonian of the atom-light system is given by:

$$\mathcal{H} = \mathcal{H}' + V(\vec{r}). \tag{1.31}$$

where, $V(\vec{r})$ is the Coulomb interaction potential, $\vec{r}$ being the position vector of the valence electron from the nucleus. In the quantum mechanical version of the above equation, we replace the momentum and total energy of the system with the corresponding quantum mechanical operators, $\vec{p} \rightarrow \hat{\mathbf{p}} = -i\hbar\vec{\nabla}$, and $E \rightarrow \hat{\mathbf{E}} = i\hbar\partial/\partial t$, respectively. The Hamiltonian, $\mathcal{H}$ in Eq. (1.31) can be derived for a quantum system from a gauge invariant point of view. For this, we first study the system using the non-relativistic Schrödinger equation:

$$i\hbar\frac{\partial}{\partial t}\Psi(\vec{r},t) = \hat{\boldsymbol{\mathcal{H}}}\Psi, \tag{1.32}$$

where $\Psi(\vec{r},t)$ is the wave function of the quantum system so that quantity $|\Psi(\vec{r},t)|^2$ gives the probability density of finding an electron at position $\vec{r}$ and time t. The electronic motion under Coulomb potential is described by,

$$i\hbar\frac{\partial}{\partial t}\Psi(\vec{r},t) = \left[\frac{-\hbar^2}{2m_e}\nabla^2 + V(\vec{r})\right]\Psi(\vec{r},t). \tag{1.33}$$

The general solution of Eq. (1.32) can be written as:

$$\Psi(\vec{r},t) = \psi(\vec{r},t)\exp\left[i\chi(\vec{r},t)\right], \tag{1.34}$$

If the phase,$\chi(\vec{r},t)$ is a function of both space and time variables, then the above solution does not satisfy the Schrödinger equation Eq. (1.32), but the probability density still remains invariant under this transformation. Hence to satisfy the phase invariance the Schrödinger equation has to be modified in the following form

$$i\hbar\frac{\partial}{\partial t}\Psi(\vec{r},t) = \left\{\frac{1}{2m}\left[-i\hbar\vec{\nabla} + \frac{e}{c}\vec{A}(\vec{r},t)\right]^2 - e\Phi(\vec{r},t) + V(\vec{r})\right\}\Psi(\vec{r},t), \tag{1.35}$$

where the functions $\vec{A}(\vec{r},t)$ and $\Phi(\vec{r},t)$ on right hand side of Eq. (1.35) represent the usual vector and scalar potentials of the external electromagnetic field, respectively.

In order to make Eq. (1.35) invariant under the transformation as in Eq. (1.34), the scalar and vector potentials $\Phi(\vec{r},t)$ and $\vec{A}(\vec{r},t)$ has to be replaced by the following gauge transformations

$$\vec{A}(\vec{r},t) \rightarrow \vec{A}'(\vec{r},t) = \vec{A}(\vec{r},t) - \frac{\hbar c}{e}\vec{\nabla}\chi(\vec{r},t), \tag{1.36}$$

$$\Phi(\vec{r},t) \rightarrow \Phi'(\vec{r},t) = \Phi(\vec{r},t) + \frac{\hbar}{e}\frac{\partial\chi(\vec{r},t)}{\partial t}. \tag{1.37}$$

It is to be noted that under the above gauge transformations the fields $\vec{E}$ and $\vec{B}$ remain invariant. We simplify the Hamiltonian in Eq. (1.35) using the Coulomb gauge or radiation gauge given by $\Phi(\vec{r},t) = 0$ and $\vec{\nabla}\cdot\vec{A}(\vec{r},t) = 0$. The total Hamiltonian in radiation gauge reduces to,

$$\hat{\boldsymbol{\mathcal{H}}} = -\frac{\hbar^2}{2m}\nabla^2 - \frac{ie\hbar}{2mc}\vec{A}(\vec{r},t)\cdot\vec{\nabla} + \frac{e^2}{2mc^2}\vec{A}(\vec{r},t)\cdot\vec{A}(\vec{r},t) + V(\vec{r}). \tag{1.38}$$

Now we introduce an approximation known as "*dipole approximation*" which leads to substantial simplification of the interaction Hamiltonian.

1.3.1 Electric dipole approximation

The vector potential describing the incident plane electromagnetic wave is expressed by a vector $\vec{A}(\vec{r},t)$ defined as

$$\begin{aligned}\vec{A}(\vec{r},t) &= \vec{A}(t)\exp\left(i\vec{k}\cdot\vec{r}\right),\\ &= \vec{A}(t)\exp\left(i\vec{k}\cdot\vec{r}_0\right)\exp\left[i\vec{k}\cdot(\vec{r}-\vec{r}_0)\right],\\ &= \vec{A}(t)\exp\left(i\vec{k}\cdot\vec{r}_0\right)\left[1+i\vec{k}\cdot(\vec{r}-\vec{r}_0)+\cdots\right],\end{aligned} \tag{1.39}$$

where $\vec{r}_0$ is location of nucleus of the atom and $\vec{r}$ is the position vector of any given point inside the atom. In most cases, the wavelength of the interacting EM field, λ is much larger than the size of an atom, *i.e.*, $\vec{k}\cdot(\vec{r}-\vec{r}_0) \ll 1$, where $|k| = 2\pi/\lambda$. Therefore, the above equation can be written as

$$\vec{A}(\vec{r},t) \approx \vec{A}(t)\exp(i\vec{k}\cdot\vec{r}_0). \tag{1.40}$$

This is known as the "*electric dipole approximation*" in the literature. The total Hamiltonian for the atom-field interaction under the dipole approximation is given by:

$$\hat{\boldsymbol{\mathcal{H}}} = -\frac{\hbar^2}{2m}\nabla^2 + V(\vec{r}) - \frac{ie\hbar}{2mc}\vec{A}(\vec{r}_0,t)\cdot\vec{\nabla} + \frac{e^2}{2mc^2}\vec{A}^2(\vec{r}_0,t). \tag{1.41}$$

We now perform a gauge transformation using $\chi(\vec{r},t) = (-e/\hbar c)\vec{A}(r_0,t)\cdot\vec{r}$. This transforms the wave function $\Psi(\vec{r},t)$ into the new form

$$\Psi(\vec{r},t) = \exp\left[\frac{-ie}{\hbar c}\vec{A}(\vec{r}_0,t)\cdot\vec{r}\right]\psi(\vec{r},t). \tag{1.42}$$

The electric field $\vec{E}$ at $\vec{r}_0$ in terms of the Coulomb potential is $\vec{E}(\vec{r}_0,t) = -\frac{1}{c}\frac{\partial}{\partial t}\vec{A}(\vec{r}_0,t)$. Substituting this along with Eqs. [(1.42), (1.41)] in Eq. (1.35) we get,

$$\begin{aligned} i\hbar\frac{\partial}{\partial t}\psi(\vec{r},t) &= \left\{-\frac{\hbar^2}{2m}\nabla^2 + V(\vec{r}) + e\vec{r}\cdot\vec{E}(\vec{r}_0,t)\right\}\psi(\vec{r},t) \\ &= (\hat{\boldsymbol{\mathcal{H}}}_0 + \hat{\boldsymbol{\mathcal{H}}}_I)\psi(\vec{r},t), \end{aligned} \tag{1.43}$$

where $\hat{\boldsymbol{\mathcal{H}}}_0$ and $\hat{\boldsymbol{\mathcal{H}}}_I$ denote the unperturbed and interaction parts of the Hamiltonian, respectively. The interaction Hamiltonian, $\hat{\boldsymbol{\mathcal{H}}}_I$ is written in terms of the dipole operator, $\hat{\boldsymbol{d}} = -e\hat{\boldsymbol{r}}$ as:

$$\hat{\boldsymbol{\mathcal{H}}}_I = -\hat{\boldsymbol{d}}\cdot\vec{E}. \tag{1.44}$$

Throughout this thesis, the above Hamiltonian describes the atom-field interaction. In the next section, we present the density matrix analysis; a popular formalism to study the dynamics of light-matter interaction.

1.4 Density matrix formalism

In this section, we will discuss the "*density matrix formalism*" used throughout the thesis. We shall skip the formalism of quantum mechanics and start with the relevant derivations right away. Details on the formalism of quantum mechanics can be found in the book by David J. Griffiths or R. Shankar.

Pure state

Let $|i\rangle$ represent an orthonormal basis set for the Hilbert space of a quantum system. Any vector, $|\psi\rangle$ in this Hilbert space, is called a state of the quantum system and can be written as a linear superposition of $|i\rangle$;

$$|\psi\rangle = \sum_i C_i|i\rangle, \quad \left(\langle\psi| = \sum_i C_i^*\langle i|\right) \tag{1.45}$$

Such a state is called a "*pure state*". In the above equation, C_i is a complex number, representing the probability amplitude of $|i\rangle$ in $|\psi\rangle$, so that $|C_i|^2$ gives the probability of finding the system in state, $|i\rangle$. The state, $|\psi\rangle$ is normalized provided, $\langle\psi|\psi\rangle = 1$, implying, $\sum_i |C_i|^2 = 1$, which represents the fact that total probability is conserved. Now, from Eq. (1.45),

$$C_i = \langle i|\psi\rangle, \quad C_j^* = \langle\psi|j\rangle \quad \text{such that, } C_iC_j^* = \langle i|\psi\rangle\langle\psi|j\rangle. \tag{1.46}$$

The operator, $|\psi\rangle\langle\psi|$ in the above equation is defined as the density operator or density matrix;

$$\hat{\boldsymbol{\rho}} = |\psi\rangle\langle\psi|. \tag{1.47}$$

The density matrix elements, ρ_{ij} are given as, $\rho_{ij} = \langle i|\hat{\boldsymbol{\rho}}|j\rangle = \langle i|\psi\rangle\langle\psi|j\rangle = C_iC_j^*$. Thus, diagonal elements of the density matrix, $\rho_{ii} = |C_i|^2$, are the probability of the finding the system in state, $|i\rangle$. Due to conservation of probability, $\mathrm{Tr}[\hat{\boldsymbol{\rho}}] = \sum|C_i|^2 = 1$. For a pure state, it can be shown that, $\hat{\boldsymbol{\rho}}^2 = \hat{\boldsymbol{\rho}}$, implying, $\mathrm{Tr}[\hat{\boldsymbol{\rho}}^2] = \mathrm{Tr}[\hat{\boldsymbol{\rho}}] = 1$.

The expectation value of an operator $\hat{\boldsymbol{\mathcal{O}}}$ in the state, $|\psi\rangle$ is given as:

$$\begin{aligned}\langle\hat{\boldsymbol{\mathcal{O}}}\rangle &= \langle\psi|\hat{\boldsymbol{\mathcal{O}}}|\psi\rangle, \\ &= \langle\psi|\sum_{ij}\mathcal{O}_{ij}|i\rangle\langle j|\psi\rangle \quad \left(\text{Writing, } \hat{\boldsymbol{\mathcal{O}}} = \sum\mathcal{O}_{ij}|i\rangle\langle j|\right), \\ &= \sum_{ij}\mathcal{O}_{ij}\langle\psi|i\rangle\langle j|\psi\rangle = \sum_{ij}\mathcal{O}_{ij}\langle j|\psi\rangle\langle\psi|i\rangle = \sum_{ij}\mathcal{O}_{ij}\langle j|\hat{\boldsymbol{\rho}}|i\rangle, \\ &= \sum_{ij}\mathcal{O}_{ij}\rho_{ji} = \mathrm{Tr}\{\hat{\boldsymbol{\mathcal{O}}}\hat{\boldsymbol{\rho}}\}, \end{aligned} \tag{1.48}$$

The expectation value of the operator, $\hat{\boldsymbol{\mathcal{O}}}$ can be written in terms of wave functions, $\psi(\vec{r})$ as,

$$\langle\hat{\boldsymbol{\mathcal{O}}}\rangle = \int\psi^*(\vec{r})\mathcal{O}\psi(\vec{r})d\vec{r}, \tag{1.49}$$

where, $\mathcal{O}$ is the representation of the operator, $\hat{\boldsymbol{\mathcal{O}}}$ in position basis, $|\vec{r}\rangle$ and the wave functions $\psi(\vec{r})$ are nothing but the probability amplitude in position basis, $\psi(\vec{r}) = \langle\vec{r}|\psi\rangle$. In Eq. (1.49), the mathematical expression of $\psi(\vec{r})$ must be known, whereas, in Eq. (1.48), knowing the density matrix elements is sufficient to find the expectation value of any observable, which simplifies the calculation. The density matrix approach is a robust technique for extracting information about a system without knowing the expression of the wave functions.

Equation of motion

Next, we derive the equation of motion for the density matrix. Let $\hat{\boldsymbol{\mathcal{H}}}$ be the Hamiltonian of the quantum system. The Schrödinger equation [Eq. (1.32)] for a state, $|\psi\rangle$ is then given as

$$\frac{\partial|\psi\rangle}{\partial t} = -\frac{i}{\hbar}\hat{\boldsymbol{\mathcal{H}}}|\psi\rangle, \tag{1.50a}$$

$$\implies \frac{\partial\langle\psi|}{\partial t} = \frac{i}{\hbar}\langle\psi|\hat{\boldsymbol{\mathcal{H}}}^\dagger = \frac{i}{\hbar}\langle\psi|\hat{\boldsymbol{\mathcal{H}}}, \tag{1.50b}$$

again,

$$\begin{aligned}\frac{\partial\hat{\boldsymbol{\rho}}}{\partial t} = \frac{\partial|\psi\rangle\langle\psi|}{\partial t} &= \left(\frac{\partial|\psi\rangle}{\partial t}\right)\langle\psi| + |\psi\rangle\left(\frac{\partial\langle\psi|}{\partial t}\right), \\ \implies \frac{\partial\hat{\boldsymbol{\rho}}}{\partial t} &= -\frac{i}{\hbar}\left(\hat{\boldsymbol{\mathcal{H}}}|\psi\rangle\langle\psi| - |\psi\rangle\langle\psi|\hat{\boldsymbol{\mathcal{H}}}\right), \quad \text{[substituting, Eq. (1.50)]}, \\ \implies \frac{\partial\hat{\boldsymbol{\rho}}}{\partial t} &= -\frac{i}{\hbar}\left(\hat{\boldsymbol{\mathcal{H}}}\hat{\boldsymbol{\rho}} - \hat{\boldsymbol{\rho}}\hat{\boldsymbol{\mathcal{H}}}\right) = -\frac{i}{\hbar}\left[\hat{\boldsymbol{\mathcal{H}}}, \hat{\boldsymbol{\rho}}\right]. \end{aligned} \tag{1.51}$$

Equation, (1.51) is called "*Liouville-Von Neumann*" equation. However, the above form of the Liouville equation describes only the coherent interaction processes. In a physical system, there exist various incoherent processes, such as spontaneous emission, collisional mechanism, etc. So to completely understand the light-matter interaction, one has to account for all these incoherent processes in the Liouville equation. Thus the modified Liouville equation takes the following form

$$\frac{\partial\hat{\boldsymbol{\rho}}}{\partial t} = -\frac{i}{\hbar}\left[\hat{\boldsymbol{\mathcal{H}}}, \hat{\boldsymbol{\rho}}\right] + \sum_i\frac{\gamma_i}{2}\left(2\hat{\boldsymbol{\mathcal{L}}}_i\hat{\boldsymbol{\rho}}\hat{\boldsymbol{\mathcal{L}}}_i^\dagger - \{\hat{\boldsymbol{\mathcal{L}}}_i^\dagger\hat{\boldsymbol{\mathcal{L}}}_i, \hat{\boldsymbol{\rho}}\}\right). \tag{1.52}$$

Where, $\hat{\boldsymbol{\mathcal{L}}}_i$ are called the "*Lindblad*" operators or jump operators [12], associated with various transitions from one state to another and γ_i are the decay rates corresponding to those transitions. In Eq. (1.52), the round bracketed terms with summation included is known as the "*decay matrix*", which describes all the incoherent decay process in a quantum system. In the last term of Eq. (1.52), the curly bracket represents anticommutator, $\{\hat{\boldsymbol{A}}, \hat{\boldsymbol{B}}\} = \hat{\boldsymbol{A}}\hat{\boldsymbol{B}} + \hat{\boldsymbol{B}}\hat{\boldsymbol{A}}$, for any two operators, $\hat{\boldsymbol{A}}$ and $\hat{\boldsymbol{B}}$. The evaluation of the decay matrix is included in the next two sections for two and three-level systems, respectively.

1.5 Two level atom

The simplest non-trivial quantum system imaginable is a two-level atom. A two-level system consists of a ground state, say $|1\rangle$ and an excited state, $|2\rangle$, coupled by an EM field, say $\vec{E}$. The electric field is defined as:

$$\vec{E}(\vec{r}, t) = \hat{e}\mathcal{E}(\vec{r}, t)e^{i(\vec{k}\cdot\vec{r}-\omega t)} + \text{c.c.}, \tag{1.53}$$

where $\mathcal{E}(\vec{r}, t)$ is the slowly varying amplitude, $\hat{e}$ and $\vec{k}$ are the polarization unit vector and the wave vector of the probe field, respectively. An ideal two-level system does not exist in nature, however, a laser tuned close to the resonant frequency of an atomic transition while being highly detuned from all other transitions; behaves like a two-level atom. In this section, we will briefly discuss the relevant equations governing the dynamics of a two-level atom interacting with an EM field. The Hamiltonian of the two-level atom in absence of the external EM field can be

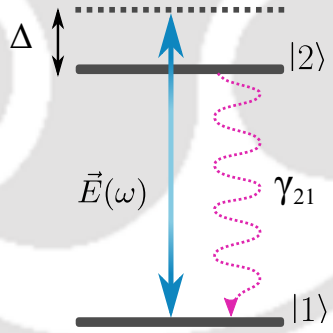

Figure 1.1: Shows a schematic diagram of the level system. An EM field, $\vec{E}$ with carrier frequency ω couples the transition $|1\rangle \leftrightarrow |2\rangle$. Here, γ_{21} denotes the radiative decay rate from the excited state $|2\rangle$ to the ground state $|1\rangle$.

represented as

$$\hat{\boldsymbol{\mathcal{H}}}_0 = \hbar\omega_1|1\rangle\langle 1| + \hbar\omega_2|2\rangle\langle 2|, \tag{1.54}$$

where, $\hbar\omega_1$ and $\hbar\omega_2$ are the energy Eigen states of the $\mathcal{H}_0$. For convenience, the energy of the ground state, $|1\rangle$ is set to zero such that, Eq. (1.54) can be simplified as, $\hat{\boldsymbol{\mathcal{H}}}_0 = \hbar\omega_{21}|2\rangle\langle 2|$ with, $\omega_{21} = \omega_2 - \omega_1$, being the resonant frequency of the transition, $|2\rangle \leftrightarrow |1\rangle$. A general state of the system obeying the Schrödinger equation can be written as: and the wave function in the picture is as fellow:

$$|\psi\rangle = C_1|1\rangle + C_2|2\rangle, \tag{1.55}$$

where C_i $(i = 1, 2)$ are complex numbers, representing the probability amplitude of the atom being in state $|i\rangle$. The density matrix operator for the two level atom is defined as, $\hat{\boldsymbol{\rho}} = |\psi\rangle\langle\psi|$, *i.e.*,

$$\hat{\boldsymbol{\rho}} = \begin{pmatrix} \rho_{11} & \rho_{12} \\ \rho_{21} & \rho_{22} \end{pmatrix}, \tag{1.56}$$

where the density matrix elements can be written in terms of C_i as

$$\rho_{11} = C_1 C_1^*, \quad \rho_{22} = C_2 C_2^*, \quad \rho_{12} = \rho_{21}^* = C_1 C_2^*. \tag{1.57}$$

Here, the diagonal elements of the density matrix, ρ_{ii}, give the probability of the atom being in the state, $|i\rangle$. The non-diagonal elements of ρ_{ij} $(i \neq j)$ are called "*atomic coherence*" or "*induced coherence*". The dipole moments of the system are represented by a dipole moment operator, $\hat{\boldsymbol{d}}$;

$$\hat{\boldsymbol{d}} = \vec{d}_{11}|1\rangle\langle 1| + \vec{d}_{22}|2\rangle\langle 2| + \vec{d}_{12}|1\rangle\langle 2| + \vec{d}_{21}|2\rangle\langle 1|, \tag{1.58}$$

where the diagonal element, $\vec{d}_{ii}$ represent the permanent dipole moments associated with state, $|i\rangle$ and the non-diagonal elements, $\vec{d}_{ij}$ $(i \neq j)$ represent the induced dipole moments due to coupling of the field, $\vec{E}$ with $|1\rangle \leftrightarrow |2\rangle$ transition. Since atoms do not possess any permanent dipole moment, the diagonal elements, $\vec{d}_{ii}$ are zero. They are nonzero for polar molecules such as water, H_2O. The interaction Hamiltonian of the two-level atom in the dipole moment approximation can be written as :

$$\begin{aligned} \hat{\boldsymbol{\mathcal{H}}}_I &= -\hat{\boldsymbol{d}} \cdot \vec{E} \\ &= -(\vec{d}_{12}|1\rangle\langle 2| + \vec{d}_{21}|2\rangle\langle 1|) \cdot \vec{E}, \qquad (1.59) \\ &= -\left[\vec{d}_{12} \cdot \hat{e}\mathcal{E}(\vec{r}, t)e^{i(\vec{k}\cdot\vec{r}-\omega t)} + \vec{d}_{12} \cdot \hat{e}\mathcal{E}^*(\vec{r}, t)e^{-i(\vec{k}\cdot\vec{r}-\omega t)}\right]|1\rangle\langle 2|, \\ &\quad -\left[\vec{d}_{21} \cdot \hat{e}\mathcal{E}(\vec{r}, t)e^{i(\vec{k}\cdot\vec{r}-\omega_p t)} + \vec{d}_{21} \cdot \hat{e}\mathcal{E}^*(\vec{r}, t)e^{-i(\vec{k}\cdot\vec{r}-\omega t)}\right]|2\rangle\langle 1|, \qquad (1.60) \end{aligned}$$

Therefore the total Hamiltonian of the atom is given by:

$$\hat{\boldsymbol{\mathcal{H}}} = \hat{\boldsymbol{\mathcal{H}}}_0 + \hat{\boldsymbol{\mathcal{H}}}_I = \hbar\omega_{12}|1\rangle\langle 1| - (\vec{d}_{12}|1\rangle\langle 2| + \vec{d}_{21}|2\rangle\langle 1|) \cdot \vec{E}, \tag{1.61}$$

Now, get rid of any explicit time dependence as seen in Eq. (1.59), we make the following unitary transformation:

$$|\psi(t)\rangle = \hat{\boldsymbol{U}}|\phi(t)\rangle \quad \left(\hat{\boldsymbol{U}} = e^{-i\omega t|1\rangle\langle 1|}\right), \tag{1.62}$$

The Schrödinger equation in the transformed basis can then be written as:

$$i\hbar\frac{\partial|\phi(t)\rangle}{\partial t} = \hat{\boldsymbol{\mathcal{H}}}_{\text{eff}}|\phi(t)\rangle. \tag{1.63}$$

where, $\hat{\boldsymbol{\mathcal{H}}}_{\text{eff}}$ is called the "*effective Hamiltonian*" and is given as, $\hat{\boldsymbol{\mathcal{H}}}_{\text{eff}} = \hat{\boldsymbol{U}}^\dagger\hat{\boldsymbol{\mathcal{H}}}\hat{\boldsymbol{U}} - i\hbar\hat{\boldsymbol{U}}^\dagger\partial_t\hat{\boldsymbol{U}}$ which simplifies to,

$$\hat{\boldsymbol{\mathcal{H}}}_{\text{eff}}/\hbar = -\Delta|1\rangle\langle 1| - (\Omega|1\rangle\langle 2| + \text{h.c.}) - (\tilde{\Omega}e^{-2i\omega t}|1\rangle\langle 2| + \text{h.c.}), \tag{1.64}$$

where h.c. stands for "*Hermitian conjugate*", $\Delta = \omega - \omega_{12}$, is called the field "*detuning*" and is the difference in frequency of the external EM field and the resonance

frequency of $|1\rangle \leftrightarrow |2\rangle$ transition. The terms in Eq. (1.65) are known as the Rabi frequency and are given by

$$\Omega = \frac{\vec{d}_{12} \cdot \hat{e}\mathcal{E}}{\hbar} e^{-i\vec{k}\cdot\vec{r}}, \quad \tilde{\Omega} = \frac{\vec{d}_{12} \cdot \hat{e}^* \mathcal{E}^*}{\hbar} e^{-i\vec{k}\cdot\vec{r}}, \tag{1.65}$$

Where, the exponential term, $e^{-i\vec{k}\cdot\vec{r}} \approx 1$ ($\vec{r}$ is the position vector of the valence electron with respect to the nucleus of the atom) in the visible spectrum. This approximation is known as the electric dipole approximation as mentioned in Eq. sec. 1.3.1. When integrating Eq. (1.63), to solve for $|\phi\rangle$, the integral $\int \tilde{\Omega} e^{-2i\omega t} dt \equiv \tilde{\Omega} e^{-2i\omega t}/2\omega$ in Eq. (1.64). In the optical frequency range of the EM spectrum, $\tilde{\Omega} \ll 2\omega$, *i.e.*, $\int \tilde{\Omega} e^{-2i\omega t} dt \equiv \tilde{\Omega} e^{-2i\omega t}/2\omega \to 0$. Therefore, Therefore, the highly oscillatory term $\tilde{\Omega}$ in Eq. (1.64) can be neglected at optical frequency domain. This approximation is known as the "*rotating wave approximation*" (RWA) [13] which is used thoughout this thesis. The effective Hamiltonian under RWA is given by

$$\hat{\boldsymbol{\mathcal{H}}}_{\text{eff}}/\hbar = -\Delta|1\rangle\langle 1| - (\Omega|1\rangle\langle 2| + \Omega^*|2\rangle\langle 1|). \tag{1.66}$$

Now, we use the density matrix equation derived earlier in Eq. (1.51) without the decay matrix, for simplicity;

$$\frac{\partial \hat{\boldsymbol{\rho}}}{\partial t} = -\frac{i}{\hbar}[\hat{\boldsymbol{\mathcal{H}}}_{\text{eff}}, \hat{\boldsymbol{\rho}}]. \tag{1.67}$$

The dynamics of population and polarization of the atoms in the two-level configuration is given by

$$\dot{\rho}_{11} = -\dot{\rho}_{22} = i\Omega^* \rho_{21} - i\Omega\rho_{12}, \tag{1.68a}$$
$$\dot{\rho}_{12} = \dot{\rho}_{21}^* = -i\Delta\rho_{12} - i\Omega\left(\rho_{11} - \rho_{22}\right), \tag{1.68b}$$

where dot denotes $\partial/\partial t$. The above equations are known as the optical Bloch equations (OBE), analogous to the Bloch equations in nuclear magnetic resonance (NMR). The equation, $\dot{\rho}_{11} = -\dot{\rho}_{22}$, indicates that the two-level system is closed. A closed two-level system means that the excited state decays only to the ground state. Contrarily, in an open system, the excited state decays to the ground state as well to the environment, thus the total population is not conserved. For the closed two-level system, the total atomic population remains conserved, *i.e.*, $(\rho_{11} + \rho_{22} = 1)$.

The initial condition for the Eqs. (1.68) is taken as $\rho_{11}(t = 0) = 1$, *i.e.*, at time, $t = 0$, all atoms are in the ground state, $|1\rangle$. With this initial condition, solutions for Eqs. (1.68) are given as:

$$\rho_{22} = \frac{4\Omega^2}{\Omega_g^2} \sin^2\left(\frac{\Omega_g t}{2}\right), \quad \rho_{11} = 1 - \rho_{22} = 1 - \frac{4\Omega}{\Omega_g^2} \sin^2\left(\frac{\Omega_g t}{2}\right) \tag{1.69}$$

$$\rho_{12} = \frac{2\Omega}{\Omega_g^2} \sin\left(\frac{\Omega_g t}{2}\right) \left\{\Delta \sin\left(\frac{\Omega_g t}{2}\right) + i\Omega_g \cos\left(\frac{\Omega_g t}{2}\right)\right\}, \tag{1.70}$$

where $\Omega_g = \sqrt{(\Delta^2 + 4|G|^2)}$ is called the "*generalized Rabi frequency*". At resonance, the detuning, $\Delta = \omega - \omega_{21} = 0$, implying, $\Omega_g = 2\Omega$. This makes, Eq. (1.69)

$$\rho_{11} = \cos^2\left(\frac{\Omega t}{2}\right), \quad \rho_{22} = \sin^2\left(\frac{\Omega t}{2}\right) \tag{1.71}$$

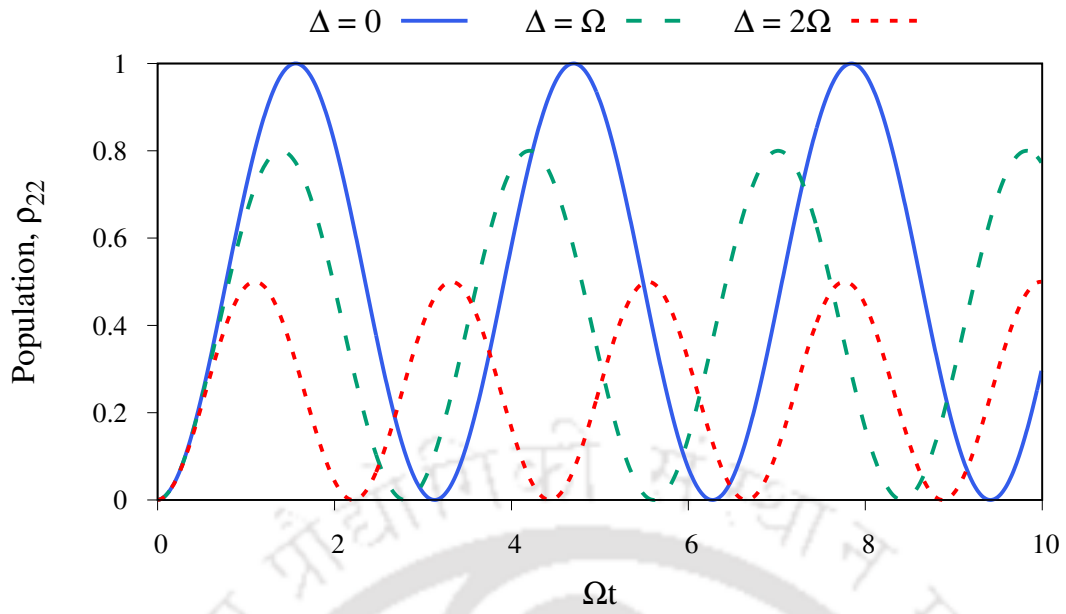

Figure 1.2: Plot showing population in excited state, $|2\rangle$ at different detunings, Δ

Equation, (1.71) suggests that the atom oscillates symmetrically between states, $|1\rangle$ and $|2\rangle$ frequency Ω. This is known as Rabi oscillation. Increasing the detuning, Δ leads to increases number of oscillations and reduction in amplitude of oscillation as show in Fig. 1.2. A comprehensive discussion on two-level atom is available in the book by Allen and Eberly [14].

Spontaneous emission

According to Einstein's theory of light-matter interaction, an atom can transition from the excited state, $|2\rangle$ to the ground state, $|1\rangle$ by the following processes:

Stimulated emission: A photon of energy, $\hbar\omega_{21}$, incident on an atom in the excited state, $|2\rangle$ can lead to deexcitation of the atom to the ground state, $|1\rangle$ by emission of a photon of same energy as that of the incident photon. Since this process is induced by the incident photon, its known as stimulated emission.

Spontaneous emission: In the absence of any external radiation, an atom in the excited state, $|2\rangle$ can spontaneously transition to the ground state $|2\rangle$ by emitting a photon of energy $\hbar\omega_{12}$. This phenomenon is called spontaneous emission since it doesn't require any external influence .

Nonradiative deexcitation: The atom can also transition from $|2\rangle$ to $|1\rangle$ without emitting any radiation. This can happen due to collisions between atoms leading to an increase in vibrational or rotational energy in the case of molecules, or rearrangement of electrons in atoms.

The probability per unit time for the stimulated emission and spontaneous emission are denoted by $\mathcal{B}_{21}$ and $\mathcal{A}_{21}$, respectively; popularly known as Einstein's coefficients. A full quantum mechanical treatment for the two level atom relates the above probabilities to atomic properties:

$$\mathcal{A}_{21} = \frac{4|\vec{d}_{21}|^2\omega_{21}^3}{3\hbar c^3}, \quad \mathcal{B}_{21} = \frac{4\pi^2|\vec{d}_{21}|^2}{3\hbar^2}. \tag{1.72}$$

Using the Fermi golden rule it can be shown that the transition rate from a discrete atomic state to a continuum of electromagnetic modes is given by

$$\mathcal{A}_{21} = \frac{2\pi}{\hbar}|V_{12}|^2\rho(\omega), \tag{1.73}$$

where $|V_{12}|^2$ is the transition matrix element; it connects the initial and final states of an atomic system and $\rho(\omega)$ is the density of the mode of the final radiation states [5]. Therefore, the spontaneous emission rate can be changed by changing the density of modes or the coupling strength of the incident radiation. The density matrix

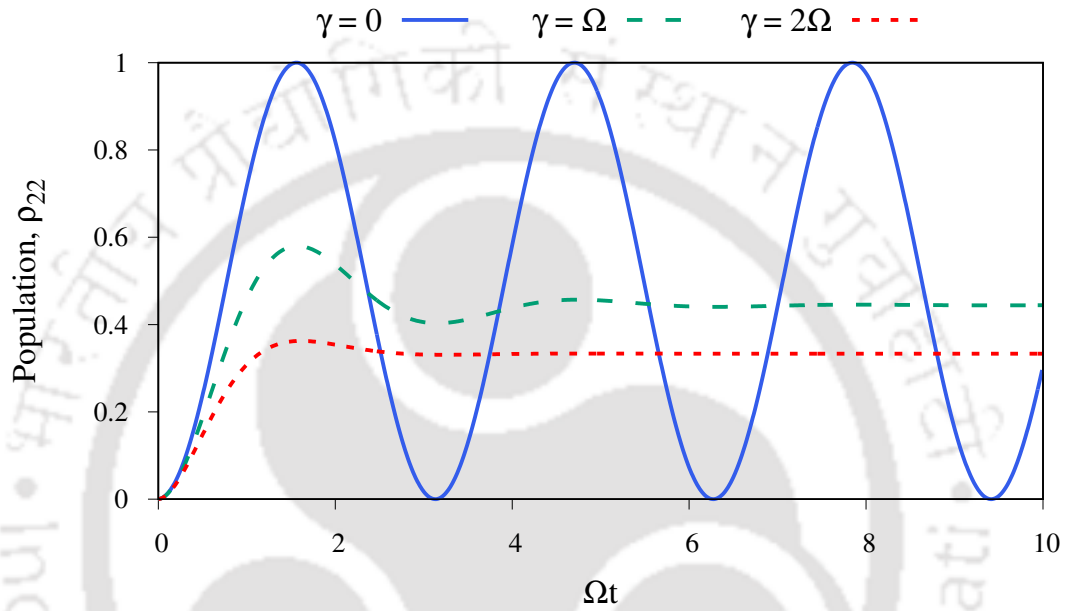

Figure 1.3: Plot showing population in excited state, $|2\rangle$ at different decay rates, γ

equation incorporating all the aforementioned decay processes is written as

$$\frac{\partial\hat{\boldsymbol{\rho}}}{\partial t} = -\frac{i}{\hbar}[\hat{\boldsymbol{\mathcal{H}}}_{\text{eff}}, \hat{\boldsymbol{\rho}}] + \hat{\boldsymbol{\mathcal{L}}}_{\rho}, \tag{1.74}$$

where, we have represented the decay matrix by, $\hat{\mathcal{L}}_{\rho}$. For the two-level atom, the Lindblad operator is defined as,

$$\hat{\mathcal{L}} = |2\rangle\langle 1|, \quad \hat{\mathcal{L}}^{\dagger} = |1\rangle\langle 2|, \tag{1.75}$$

such that $\hat{\mathcal{L}}|1\rangle = |2\rangle$ and $\hat{\mathcal{L}}^{\dagger}|2\rangle = |1\rangle$. Using, Eq. (1.75), in the definition of decay matrix [Eq. (1.52)], we get

$$\hat{\boldsymbol{\mathcal{L}}}\rho = -\frac{\gamma_{21}}{2}\left(|2\rangle\langle 2|\hat{\boldsymbol{\rho}} - 2|1\rangle\langle 1|\rho_{22} + \hat{\boldsymbol{\rho}}|1\rangle\langle 1|\right) \tag{1.76}$$

where γ_{21} is the radiative decay rate from excited state, $|2\rangle$ to ground state $|1\rangle$. The density matrix equations of the system are:

$$\dot{\rho}_{11} = \gamma_{21}\rho_{22} + i\Omega^*\rho_{21} - i\Omega\rho_{12}, \tag{1.77a}$$
$$\dot{\rho}_{22} = -\dot{\rho}_{11}, \tag{1.77b}$$

$$\dot{\rho}_{12} = -\left(\frac{\gamma_{21}}{2} - i\Delta\right)\rho_{12} - i\Omega\left(\rho_{11} - \rho_{22}\right), \tag{1.77c}$$

$$\dot{\rho}_{21} = \dot{\rho}^*_{12}, \tag{1.77d}$$

Figure 1.3 shows population in groud state, $|1\rangle$ for different values of decay rate, $\gamma_{21} = \gamma$. In Fig. 1.3, the Rabi oscillations damped out rapidly and after a certain time, the system reaches a steady state.

The steady state solutions of the density matrix equations are found by putting all time derivatives in Eq. (1.77) to zero. The steady state population in the excited state, $|2\rangle$ and the induced coherence are given as

$$\rho_{22} = \frac{|\Omega|^2}{(\gamma^2 + \Delta^2) + 2|\Omega|^2}, \quad \rho_{21} = \frac{i\Omega(\gamma + i\Delta)}{(\gamma^2 + \Delta^2) + 2|\Omega|^2}. \tag{1.78}$$

The induced polarization, say at frequency ω, is expressed in terms of the non-diagonal elements of the density matrix, ρ_{12} and ρ_{21}:

$$\vec{P} \equiv \mathcal{N}\langle\hat{\boldsymbol{d}}\rangle \equiv \mathcal{N}\mathrm{Tr}(\hat{\boldsymbol{d}}\hat{\boldsymbol{\rho}}) \equiv \mathcal{N}(\vec{d}_{21}\rho_{12} + \vec{d}_{12}\rho_{21}). \tag{1.79}$$

Relation between susceptibility and induced coherence

From, Eq. (1.20) and Eq. (1.79), we have

$$\vec{P}(\vec{r},\omega) = \chi(\omega)\vec{E}(\vec{r},\omega), \quad \text{and} \quad \vec{P}(\omega) = \mathcal{N}\vec{d}_{12}\rho_{21}, \tag{1.80}$$

Equating the above equations and using the expression of Rabi frequency, $\Omega = \vec{d}_{12}\cdot\vec{E}/\hbar$, we get:

$$\chi = \frac{\mathcal{N}|d_{12}|^2}{\hbar\Omega}\rho_{21}. \tag{1.81}$$

According to Weisskopf-Wigner theory, $|d_{12}|^2/\hbar = 3\gamma_{21}/2k^3$, using which, the above equation can be written as

$$\chi = \eta\frac{\rho_{21}}{\Omega/\gamma_{21}} \quad \left(\eta = \frac{3\mathcal{N}}{2k^3}\right). \tag{1.82}$$

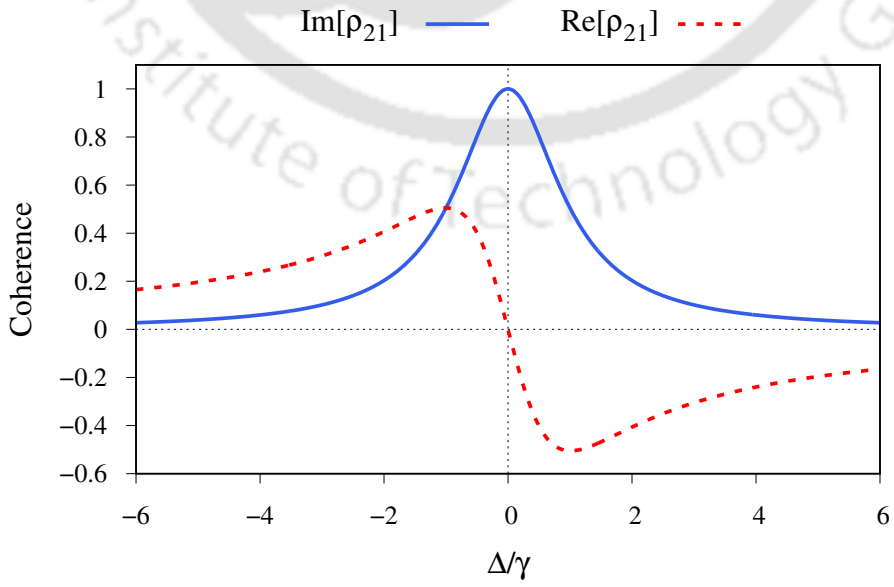

Figure 1.4: Real and imaginary part of ρ_{12} vs detuning, Δ for $\Omega = 0.1\gamma$.

Thus, the susceptibility, χ of the medium can be written in terms of the steady state coherence, ρ_{12} as

$$\chi = \frac{\mathcal{N}|d_{12}|^2}{\hbar\Omega}\rho_{21} = \frac{\mathcal{N}|d_{12}|^2}{\hbar}\frac{i(\gamma + i\Delta)}{(\gamma^2 + \Delta^2) + 2|\Omega|^2}, \tag{1.83}$$

The above expression of susceptibility is obtained using the exact analytical solution of the density matrix equations. Thus, Eq. (1.83) is valid for all intensities of $\vec{E}$ and not only low intensity. Figure 1.4 shows the real and imaginary part of atomic coherence, ρ_{21}. In Fig. 1.4, near the resonance of $|1\rangle \leftrightarrow |2\rangle$ transition, the imaginary part of atomic coherence, ρ_{21} has a maxima, indicating large absorption of the EM field, $\vec{E}$. This limits utilization of the high dispersion near the resonance as indicated by the real part of ρ_{21} in Fig. 1.4. To circumvent this, saturation absorption technique (SAT) is used, where an extra-strong field is applied which takes the medium into a saturation stage and prevents the absorption of a weak probe field. In the next section we discuss the three-level atomic system and explain the phenomenon of electromagnetically induced transparency.

1.6 Three level atom

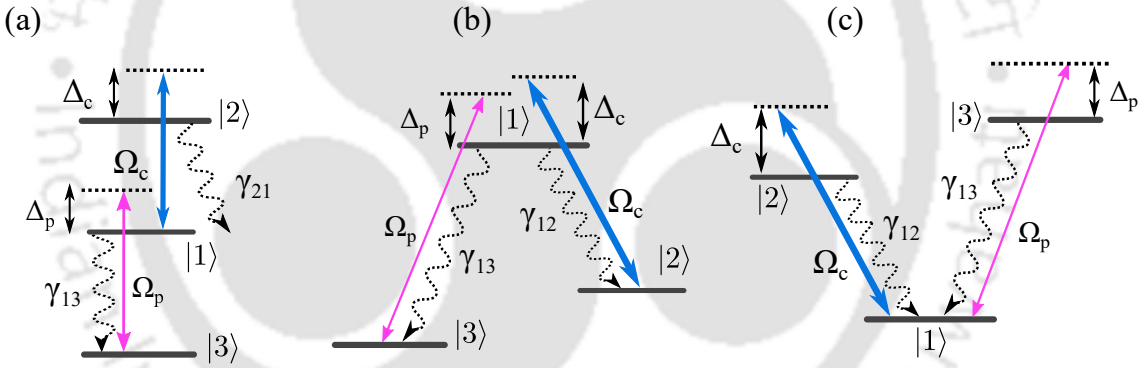

Figure 1.5: Schematic diagram of a three types of three level systems. (a), (b), and (c) are known as "Ladder" Ξ, "Lambda Λ", and "Vee V " systems, respectively.

The three-level system interacting with two monochromatic fields is considered a natural extension of the two-level atomic system. The atomic coherence effects in a three-level system are greatly enhanced compared to the two-level system which can change the absorption and dispersion of the system drastically. Depending on the level structure and the dipole-allowed transitions, there exist three types of three-level configurations as shown in Fig. 1.5. We will discuss only the 2$^{\text{nd}}$ configuration, *i.e.* "Lambda (Λ)" system [Fig. 1.5(b)]. In Fig. 1.5(b), a strong field, known as the control field, with frequency, ω_c, couples $|1\rangle \leftrightarrow |2\rangle$ transition and a weak probe field with frequency ω_p couples $|1\rangle \leftrightarrow |3\rangle$ transition. The probe and control fields are defined as,

$$\vec{E}_j(r,t) = \hat{e}_j\mathcal{E}_j(r,t)e^{-i(\omega_j t - \vec{k}_j.\vec{r})} + \text{c.c.}, \tag{1.84}$$

where $\hat{e}_j$ are the unit polarization vectors, $\mathcal{E}_j(r,t)$ are the slowly varying envelope functions, ω_j are the field carrier frequencies and $\vec{k}_j = k_j\hat{z}$ are the wave vectors of

the fields. The index $j \in p, c$ represents probe and control fields, respectively. The detuning and Rabi frequencies of the respective fields are defined as:

$$\Delta_c = \omega_c - \omega_{12}\ ,\ \Delta_p = \omega_p - \omega_{13}\ ,\ \Omega_p = \frac{\vec{d}_{13}\cdot\hat{e}_p\mathcal{E}_p}{\hbar}\ ,\ \Omega_c = \frac{\vec{d}_{12}\cdot\hat{e}_c\mathcal{E}_c}{\hbar}, \tag{1.85}$$

The total Hamiltonian for a Λ-system is given by

$$\hat{\boldsymbol{\mathcal{H}}}/\hbar = \omega_{13}|1\rangle\langle 1| + \omega_{12}|2\rangle\langle 2| - \left(\Omega_c|1\rangle\langle 2|e^{-i\omega_c t} + \Omega_p|1\rangle\langle 2|e^{-i\omega_p t} + \text{h.c.}\right), \tag{1.86}$$

where the state $|3\rangle$ is considered as a ground state. We then apply an unitary transformation,

$$\hat{\boldsymbol{U}} = \exp\left[i\omega_p t|1\rangle\langle 1| + i(\omega_p - \omega_c)t|2\rangle\langle 2|\right], \tag{1.87}$$

and apply RWA to get the effective Hamiltonian as

$$\hat{\boldsymbol{\mathcal{H}}}_{\text{eff}}/\hbar = -\Delta_p|1\rangle\langle 1| - (\Delta_p - \Delta_c)|2\rangle\langle 2| - (\Omega_c|1\rangle\langle 2| + \Omega_p|1\rangle\langle 3| + \text{h.c.}). \tag{1.88}$$

In the above equation, the round bracketed coefficient, $(\Delta_p - \Delta_c)$ in the 2^{nd} term is known as "*two-photon detuning*". The Lindblad operators for $|3\rangle \leftrightarrow |1\rangle$ and $|2\rangle \leftrightarrow |1\rangle$ transitions are $\hat{\boldsymbol{\mathcal{L}}}_1 = |1\rangle\langle 3|$, $\hat{\boldsymbol{\mathcal{L}}}_1^\dagger = |3\rangle\langle 1|$, and $\hat{\boldsymbol{\mathcal{L}}}_2 = |1\rangle\langle 2|$, $\hat{\boldsymbol{\mathcal{L}}}_2^\dagger = |2\rangle\langle 1|$, respectively, such that $\hat{\boldsymbol{\mathcal{L}}}_1|3\rangle = |1\rangle$, $\hat{\boldsymbol{\mathcal{L}}}_1^\dagger|1\rangle = |3\rangle$, $\hat{\boldsymbol{\mathcal{L}}}_2|2\rangle = |1\rangle$, and $\hat{\boldsymbol{\mathcal{L}}}_2^\dagger|1\rangle = |2\rangle$. The spontaneous emission decay rate from excited state, $|1\rangle$ to states, $|3\rangle$ and $|2\rangle$ are γ_{13} and γ_{12}, respectively. Using the above Lindblad operators and decay rates, the decay matrix for the three-level Λ system can be written as:

$$\hat{\boldsymbol{\mathcal{L}}}\rho = -\sum_{j=2}^{3}\frac{\gamma_{1i}}{2}\left(|1\rangle\langle 1|\hat{\boldsymbol{\rho}} - 2|j\rangle\langle j|\rho_{jj} + \hat{\boldsymbol{\rho}}|1\rangle\langle 1|\right), \tag{1.89}$$

With the Eqs. [(1.88), (1.89)], the density matrix equation for the Λ system are then given as:

$$\dot{\rho}_{11} = -\left(\gamma_{12} + \gamma_{13}\right)\rho_{11} + i\left(\Omega_c\rho_{21} - \Omega_c^*\rho_{12} + \Omega_p\rho_{31} - \Omega_p^*\rho_{13}\right), \tag{1.90a}$$

$$\dot{\rho}_{22} = \gamma_{12}\rho_{11} + i\left(\Omega_c^*\rho_{12} - \Omega_c\rho_{21}\right), \tag{1.90b}$$

$$\dot{\rho}_{33} = \gamma_{13}\rho_{11} + i\left(\Omega_p^*\rho_{13} - \Omega_p\rho_{31}\right), \tag{1.90c}$$

$$\dot{\rho}_{12} = -\left(\Gamma_{12} - i\Delta_c\right)\rho_{12} + i\Omega_p\rho_{32} + i\Omega_c\left(\rho_{22} - \rho_{11}\right), \tag{1.90d}$$

$$\dot{\rho}_{13} = -\left(\Gamma_{13} - i\Delta_p\right)\rho_{13} + i\Omega_c\rho_{23} + i\Omega_p\left(\rho_{33} - \rho_{11}\right), \tag{1.90e}$$

$$\dot{\rho}_{23} = -\left[\Gamma_{23} - i\left(\Delta_p - \Delta_c\right)\right]\rho_{23} + i\left(\Omega_c^*\rho_{13} - \Omega_p\rho_{21}\right) \tag{1.90f}$$

where, γ_{12} and γ_{13} are the spontaneous emission rates from the states $|1\rangle$ to the state $|2\rangle$ and $|3\rangle$, respectively. The decay rates of the induced coherences, ρ_{12}, ρ_{13}, and ρ_{23} are denoted by Γ_{12}, Γ_{13}, and Γ_{23}, respectively, where, $\Gamma_{12} = \Gamma_{13} = (\gamma_{12} + \gamma_{13})/2$. In the weak probe limit, $\Omega_p \ll \Omega_c$, the steady state atomic coherence associated with $|1\rangle \longleftrightarrow |3\rangle$ transition, can be written in first order of probe Rabi frequency, Ω_p as:

$$\rho_{13} = \frac{i\Omega_p(\Gamma_{23} - i(\Delta_p - \Delta_c))}{|\Omega_c|^2 + (\Gamma_{13} - i\Delta_p)(\Gamma_{23} - i(\Delta_p - \Delta_c))}. \tag{1.91}$$

The corresponding susceptibility of the medium for the probe field is:

$$\chi = \frac{\mathcal{N}|d_{31}|^2}{\hbar\Omega_p}\rho_{13} = \frac{i\mathcal{N}|d_{31}|^2}{\hbar}\frac{1}{\frac{|\Omega_c|^2}{(\Gamma_{23} - i(\Delta_p - \Delta_c))} + (\gamma - i\Delta_p)}, \tag{1.92}$$

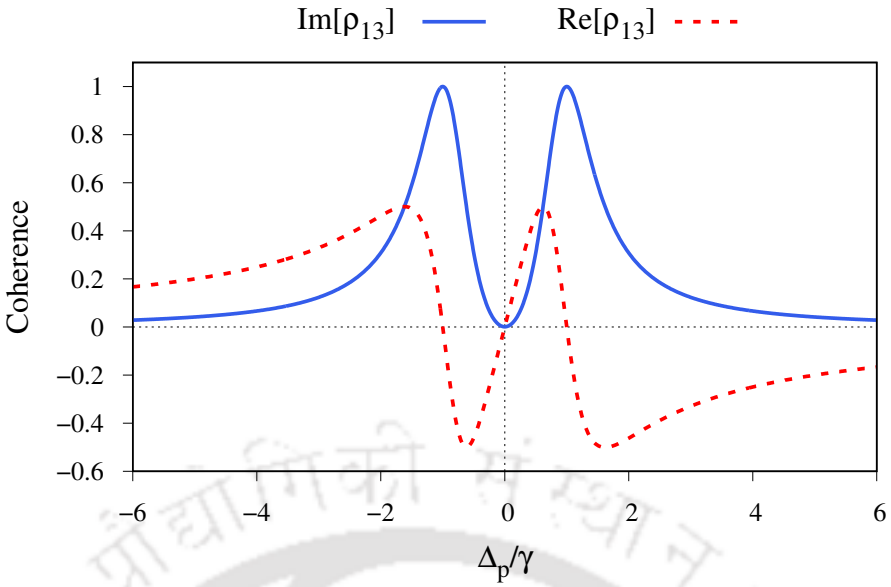

Figure 1.6: Real and imaginary part of ρ_{13} vs probe detuning, Δ_p. Note that the plots have been normalized with maximum value of ρ_{13}

where we have assumed $\gamma = \gamma_{13} = \gamma_{12}$, for simplicity. In the absence of the control field ($|\Omega_c|^2 = 0$), Eq. (1.91) gives the same result as the two level system as shown in Fig. 1.4. Figure, 1.6 shows the real and imaginary part of ρ_{13} with nonzero control field. In Fig. 1.6, the probe absorption is suppressed within a narrow frequency range, near the resonance of $|3\rangle \leftrightarrow |1\rangle$ transition. This phenomenon is know as *"Electromagnetically Induced Transparency"* (EIT) [15], first experimentally observed by Harris *et al.* [16] in 1991. The vanishing of absorption at the line center can be understood by using the quantum interference theory. In quantum mechanics, the probability amplitudes associated with several alternate pathways corresponding to a transition can interfere constructively or destructively. For example, in the Λ system, an atom from the ground state $|3\rangle$ can excite to the excited state, $|1\rangle$, in the following ways: The direct path $|3\rangle \rightarrow |1\rangle$, or via $|3\rangle \rightarrow |1\rangle \rightarrow |2\rangle \rightarrow |1\rangle$. When the two-photon detuning is zero, *i.e.*, $\Delta_p - \Delta_c = 0$, the probability amplitudes of these two transition pathways interfere destructively, resulting in the transparency seen in Fig. 1.6.

Dressed state analysis

EIT can also be explained in terms of "*dressed states*", which are the Eigen states of the effective RWA Hamiltonian given in Eq. (1.88);

$$\hat{\boldsymbol{\mathcal{H}}}_{\text{eff}} = -\hbar \begin{pmatrix} \Delta_p & 0 & \Omega_p \\ 0 & (\Delta_p - \Delta_c) & \Omega_c \\ \Omega_p^* & \Omega_c^* & 0 \end{pmatrix}. \tag{1.93}$$

Keeping the analysis simple, we consider the "*two photon resonance condition*", $\Delta_p - \Delta_c = 0$. The eigenvalues of $\hat{\boldsymbol{\mathcal{H}}}_{\text{eff}}$ at two photon resonance are given as:

$$\epsilon_0 = 0, \tag{1.94}$$

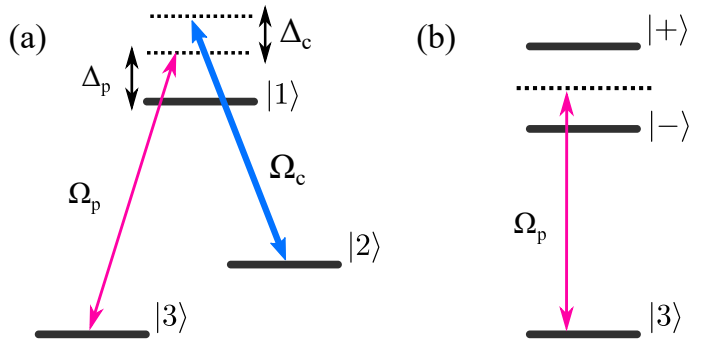

Figure 1.7: (a) Three-level Λ system in terms of bare states. (b) The dressed states representation of Λ system.

$$\epsilon_+ = \frac{\hbar}{2}\left[\Delta_p + \sqrt{\Delta_p^2 + 4(|\Omega_p|^2 + |\Omega_c|^2)}\right], \tag{1.95}$$

$$\epsilon_- = \frac{\hbar}{2}\left[\Delta_p - \sqrt{\Delta_p^2 + 4(|\Omega_p|^2 + |\Omega_c|^2)}\right], \tag{1.96}$$

and the corresponding eigenvectors are:

$$|0\rangle = \cos\theta|3\rangle - \sin\theta|2\rangle, \tag{1.97a}$$

$$|+\rangle = \sin\theta\sin\phi|3\rangle + \cos\theta\sin\phi|2\rangle + \cos\phi|1\rangle, \tag{1.97b}$$

$$|-\rangle = \sin\theta\cos\phi|3\rangle + \cos\theta\cos\phi|2\rangle - \sin\phi|1\rangle, \tag{1.97c}$$

where θ and ϕ are defined as:

$$\tan\theta = \frac{\Omega_p}{\Omega_c}, \quad \tan(2\phi) = \frac{2\sqrt{|\Omega_p|^2 + |\Omega_c|^2}}{\Delta_p}. \tag{1.98}$$

The Eigen state, $|0\rangle$ is a linear combination of the two ground states, $|3\rangle$ and $|2\rangle$, and does not contain the excited state $|1\rangle$. Thus, the transition probability from $|0\rangle \rightarrow |1\rangle$ is zero, *i.e.*, an atom prepared in the state, $|0\rangle$ will is trapped in this state, even in the presence of the probe and control fields. This phenomenon is known as *Coherent Population Trapping* (CPT) and the state, $|0\rangle$ is known as a "*dark state*". CPT was first observed by Alzetta *et al.* [17] in sodium fluorescent cell. In their experiment with sodium atoms in Λ-configuration, a dark line was observed inside a bright fluorescent cell, hence the name dark resonance is associated with CPT phenomena. Later on, Erimondo and Orriols theoretically explained the CPT phenomenon using induced atomic coherence and interference effects [18]. CPT has important applications in coherent population transfer [19], lasing without inversion [20], atomic clocks [21], etc.

We now consider a special case where the probe field is very weak compared to the control field *i.e.*, $\Omega_p \ll \Omega_c$. The dressed states under this weak probe approximation are given by

$$|0\rangle = |3\rangle, \quad |+\rangle = \frac{1}{\sqrt{2}}(|1\rangle + |2\rangle), \quad |-\rangle = \frac{1}{\sqrt{2}}(|1\rangle - |2\rangle). \tag{1.99}$$

From Eq. (1.99), under a weak probe approximation, the ground state $|3\rangle$ becomes a dark state, *i.e.*, atoms in the ground state, $|3\rangle$ are trapped and cannot be excited

to the state $|1\rangle$, thus resulting in the dip in absorption seen in Fig. 1.6. Moreover, a coherent dressing of the $|2\rangle \rightarrow |3\rangle$ transition by a strong control field results in two superposed states $|+\rangle$ and $|-\rangle$. Each of these states are equally spaced from the excited state $|1\rangle$ by a factor of $\pm\Omega_c$ as shown in Fig. 1.7. Hence transition from $|3\rangle$ to the dressed states $|+\rangle$ and $|-\rangle$ results in the formation of the two absorption peaks at $\Delta_p = \pm\Omega_c$ as in Fig. 1.6. Also with the increase in control field strength, the spacing between the dressed state increases. This leads to the increase in the width of the transparency window, also known as "*Autler Town splitting*" [22] as shown in Fig. 1.8.

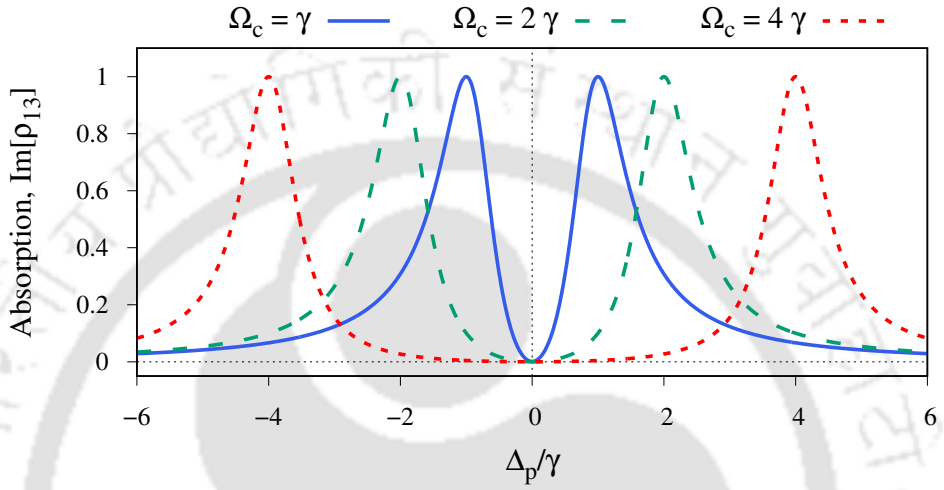

Figure 1.8: Absorption, $\mathrm{Im}[\rho_{13}]$ spectrum for different control Rabi frequencies. The seperation between absorption peaks corresponding to a particular Rabi frequency is equal to $2\Omega_c$.

1.7 Doppler effect and induced coherence

In this section, we discuss the effect of atomic velocity on induced coherence. In an atomic vapor, due to "*Doppler effect*", the component of the atom's velocity along the laser propagation direction causes a laser frequency shift in the atom's rest frame. This leads to detuning of the laser as discussed below:

Consider a laser beam with frequency, ω_s and detuning, $\Delta_{ij} = \omega_{ij} - \omega_s$, coupled to an atomic transition, $|i\rangle \leftrightarrow |j\rangle$ with resonance frequency, ω_{ij}. Let ω_a be the laser frequency as seen by the atom. The relation between ω_a and ω_s is given by:

$$\omega_o = \frac{v + v_a}{v + v_s}\omega_s, \tag{1.100}$$

where, v_{atom} is the component of atom's velocity along the laser propagation direction, v is the speed of light inside the medium, and v_s is the speed of the laser source; all with respect to the laboratory frame. The laser source is stationary, *i.e.* $v_s = 0$ and $v = \omega_s/k$, where k is the magnitude of the laser propagation vector. Thus, Eq. (1.100) can be written as:

$$\omega_a = \frac{\omega_s + kv_a}{\omega_s}\omega_s,$$

$$
\begin{aligned}
&\implies \omega_a = \omega_s + kv_a, \\
&\implies \omega_a - \Delta_{ij} = \omega_s - \Delta_{ij} + kv_a, \\
&\implies \omega_a - \Delta_{ij} = \omega_{ij} + kv_a, \qquad \text{(Putting, } \omega_{ij} = \omega_s - \Delta_{ij}\text{)}, \\
&\implies \omega_a - \omega_{ij} = \Delta_{ij} + \vec{k} \cdot \vec{v}_{\text{atom}}, \quad (\vec{v}_{\text{atom}} \text{ is the atom's velocity}), \\
&\implies \tilde{\Delta}_{ij} = \Delta_{ij} + \vec{k} \cdot \vec{v}_{\text{atom}}, \qquad (1.101)
\end{aligned}
$$

where, $\tilde{\Delta}_{ij} = \omega_a - \omega_{ij}$ is the detuning for $|i\rangle \rightarrow |j\rangle$ transition as seen by the atom. Since different atoms have different velocity, they see an inhomogenous frequency shift of the laser. This causes an increase in the linewidth of an atomic transition; a phenomenon known as "*inhomogeneous broadening*" [23]. With the modified detuning, $\tilde{\Delta}_{ij}$, the steady-state coherences, ρ_{ij} are given by their average over the Maxwell-Boltzmann velocity distribution [23]:

$$
f(v)dv = \sqrt{\frac{M}{2\pi k_B T}} \exp\left(-\frac{Mv^2}{2k_B T}\right) dv, \qquad (1.102)
$$

where T is the temperature of the gas, M is the mass of each atom, and k_B is the Boltzmann constant. The velocity averaged coherences are then given by $< \rho_{ij} >= \int_{-\infty}^{\infty} \rho_{ij}(v) f(v) dv$. At ultracold [24] temperatures (several tens of μK), the effect of atomic velocity can be ignored and the spectrum broadening is referred as "*homogeneous broadening*" [23]. The coherence plots in Figs. [1.4, 1.6], correspond to homogeneous broadening. Figures 1.9(a) and 1.9(b) show the corresponding inhomogeneously broadened coherence plots for two and three level system, respectively. In Fig. 1.9(a), the absorption spectrum of a two level atom is broadened compared to homogenous broadening; shown earlier in Fig. 1.4. In case of the three-level atom, the width of the EIT window shrinks in case of inhomogenous broadening as shown in Fig. 1.9(b).

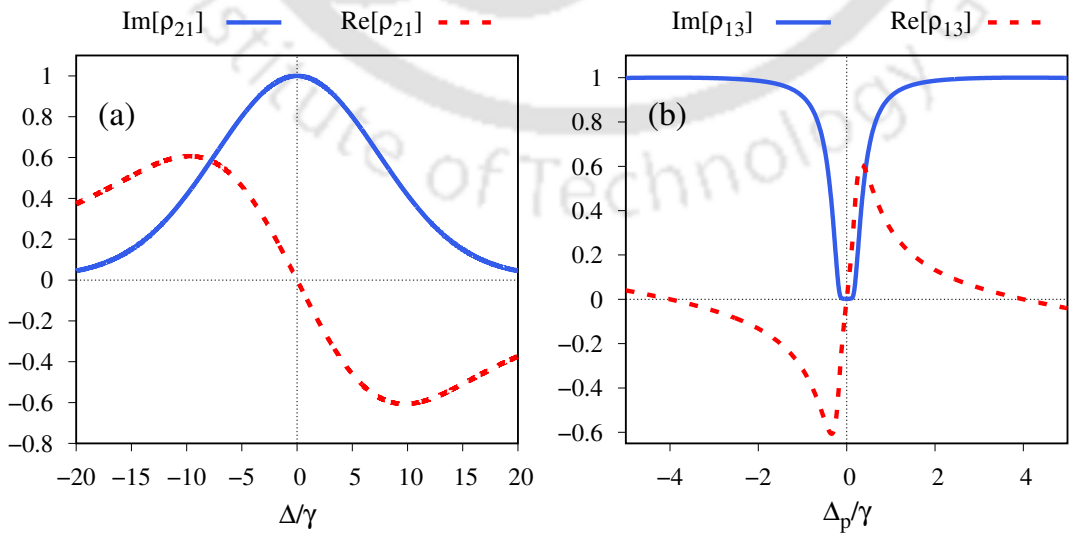

Figure 1.9: Real and imaginary part of Normalized coherences, for (a) Two level atom, and (b) Three level Λ system. Temperature of the atomic vapor, $T = 300K$

1.8 Pulse propagation in dispersive medium

A light pulse is a superposition of waves with different frequencies. The range of frequencies possessed by a pulse is called its "*bandwidth*". In vacuum, all of the frequency components travel with a constant speed, $c = 299792458\ m/s$. Whereas, inside a transparent medium such as glass, each frequency corresponds to a different speed of light, a phenomenon known as "*dispersion*". A light pulse traveling through a medium consists of mainly two kinds of velocities; "*phase*" and "*group*" velocity. The phase velocity of light is the velocity with which phase fronts of each of the frequency components propagate in a medium. For example, consider a basic sinusoidal wave traveling along z direction, $\sin(\omega t - kz)$. Its phase is given by, $\phi(z,t) = \omega t - kz$. Thus, a plane of constant phase in time would be represented as:

$$\frac{d\phi(z,t)}{dt} = \omega - k\frac{dz}{dt} = 0, \implies \frac{dz}{dt} = \frac{\omega}{k} \implies v_p = \frac{\omega}{k}, \tag{1.103}$$

On the other hand, group velocity is the velocity with which the envelope of a pulse propagates in a medium. In vacuum, all of the frequency components of a pulse travel with speed, c and phase velocity becomes equal to the group velocity. The expression of group velocity is derived below:

The susceptibility $\chi(\omega)$ can be expanded in the Taylor series as

$$\chi(\omega) = \chi(\omega_0) + (\omega - \omega_0)\frac{\partial\chi}{\partial\omega}\bigg|_{\omega_0} + \cdots, \tag{1.104}$$

where ω_0 is the center frequency of a pulse as well as resonance frequency of some atomic transition. From Eq. (1.20), we have

$$\vec{P}(\omega) = \chi(\omega)\vec{E}(\omega), \tag{1.105}$$

Multiplying both sides of the above equation with $e^{-i(\omega-\omega_0)t}$ and integrating from $-\infty$ to ∞ we get,

$$\begin{aligned}
\int_{-\infty}^{\infty}\vec{P}(\omega)e^{-i(\omega-\omega_0)t}d\omega &= \int_{-\infty}^{\infty}\left[\chi(\omega_0) + (\omega-\omega_0)\frac{\partial\chi}{\partial\omega}\bigg|_{\omega_0}\right]\vec{E}(\omega)e^{-i(\omega-\omega_0)t}d\omega \\
\implies \vec{P}(t) &= \int_{-\infty}^{\infty}\left[\chi(\omega_0) + (\omega-\omega_0)\frac{\partial\chi}{\partial\omega}\bigg|_{\omega_0}\right]\vec{E}(\omega)e^{-i(\omega-\omega_0)t}d\omega \\
&= \chi(\omega_0)\int_{-\infty}^{\infty}\vec{E}(\omega)e^{-i(\omega-\omega_0)t}d\omega + \frac{\partial\chi}{\partial\omega}\bigg|_{\omega_0}\int_{-\infty}^{\infty}(\omega-\omega_0)\vec{E}(\omega)e^{-i(\omega-\omega_0)t}d\omega \\
&= \chi(\omega_0)\int_{-\infty}^{\infty}\vec{E}(\omega)e^{-i(\omega-\omega_0)t}d\omega + \frac{\partial\chi}{\partial\omega}\bigg|_{\omega_0} i\frac{\partial}{\partial t}\int_{-\infty}^{\infty}\vec{E}(\omega)e^{-i(\omega-\omega_0)t}d\omega \\
\implies \vec{P}(t) &= \left[\chi(\omega_0) + i\frac{\partial\chi}{\partial\omega}\bigg|_{\omega_0}\frac{\partial}{\partial t}\right]\vec{E}(t),
\end{aligned} \tag{1.106}$$

where, we have replaced

$$\vec{E}(t) = \int_{-\infty}^{\infty}\vec{E}(\omega)e^{-i(\omega-\omega_0)t}d\omega.$$

Equation, (1.106) can be written in terms of the field envelop functions as:

$$\mathcal{P}(z,t) = \chi(\omega_0)\mathcal{E} + i\frac{\partial\chi(\omega)}{\partial\omega}\bigg|_{\omega_0}\frac{\partial\mathcal{E}(z,t)}{\partial t}, \tag{1.107}$$

Substituting Eq. (1.107) in Eq. (1.12) we get,

$$\frac{\partial\mathcal{E}}{\partial z} + \frac{1}{c}\frac{\partial\mathcal{E}}{\partial t} = 2\pi ik\left[\chi(\omega_0)\mathcal{E} + i\frac{\partial\chi(\omega)}{\partial\omega}\bigg|_{\omega_0}\frac{\partial\mathcal{E}}{\partial t}\right], \tag{1.108}$$

which can be rearranged as:

$$\frac{\partial\mathcal{E}}{\partial z} + \frac{1}{v_g}\frac{\partial\mathcal{E}}{\partial t} = 0, \tag{1.109}$$

where v_g is the group velocity of the pulse:

$$v_g = \mathrm{Re}\left[\frac{c}{1 + 2\pi\chi(\omega_0) + 2\pi\omega_0\,\frac{\partial\chi}{\partial\omega}\big|_{\omega_0}}\right] = \frac{c}{n_g}, \tag{1.110}$$

Since, refractive index n can be approximated as $n(\omega) \approx 1 + 2\pi\mathrm{Re}[\chi(\omega)]$. Thus the above equation can be written in terms of refractive index as:

$$v_g = \mathrm{Re}\left[\frac{c}{n(\omega) + \omega_0\,\frac{\partial n(\omega)}{\partial\omega}\big|_{\omega_0}}\right] = \frac{c}{n_g}, \tag{1.111}$$

where the term in the denominator is called "*group index*", $n_g = n + \omega\partial n/\partial\omega$, in the literature. The dependence of group velocity on χ [Eq. (1.110)] can be used for controlling the group velocity of the light pulses through an atomic vapor medium. For *e.g.*, a large refractive index, n can obtained by tuning the laser in the neighborhood of an optical resonance [see Figs. 1.4 and 1.6]. However, the usual dispersion-absorption relation suggests that the large refractive index near resonance is accompanied by nonvanishing absorption. It was demonstrated that a large refractive index along with vanishing absorption can be achieved by preparing atoms in coherent superposition states called "*phaseonium*" [25]. In a phaseonium gas, without population in the excited states, the zero absorption is always accompanied by a vanishing refractive index. However, with a small population in the excited states, absorption is suppressed in the neighborhood of resonance, with nonzero refractive index [26, 27, 28, 29, 30].

Another way of controlling the group velocity is by changing the slope of the temporal dispersion $\partial n/\partial\omega$. For a normally dispersive medium, $\partial n/\partial\omega > 0$ which gives, $v_g < c$, *i.e.*, the light pulse travels with "*subluminal*" velocity (light traveling slower in the medium than in vacuum). For anomalous dispersion, $\partial n/\partial\omega < 0$ implying $n + \partial n/\partial\omega < 1$. This results in light pulse propagation at a "*superluminal*" velocity (light traveling at a velocity faster than in the vacuum). One example of this case is $v_g = \infty$ when the condition of $n + \partial n/\partial\omega = 0$ is satisfied. This corresponds to a rare situation where the response of the medium to the applied field is local.

Therefore, manipulation of medium susceptibility is the key to controlling the group velocity of a light pulse.

1.9 Introduction to vector beams

In this section, we give an introduction to vector beams and their salient features. We start with their generation, the concept of "*optical singularities*" and then briefly discuss the singularities associated with vector beams. In the last paragraph, we discuss the applications of vector beams, highlighting their relevance.

1.9.1 Vector beam generation

Recall, the paraxial Helmholtz equation [see, Eq. (1.11)] from Sec. 1.1. In free space, Eq. (1.11) is written as:

$$\frac{1}{2ik}\nabla_{\perp}^{2}\mathcal{E}(x,y,z)+\frac{\partial\mathcal{E}(x,y,z)}{\partial z}=0. \tag{1.112}$$

For a laser with a cylindrically symmetric optical resonator, the above equation is preferably written in the cylindrical coordinate system as:

$$\left[\frac{\partial^{2}}{\partial r^{2}}+\frac{1}{r}\frac{\partial}{\partial r}+\frac{1}{r^{2}}\frac{\partial^{2}}{\partial\phi^{2}}+2ik\frac{\partial}{\partial z}\right]\mathcal{E}(r,\phi,z)=0. \tag{1.113}$$

The solutions of the above equation are known as Laguerre-Gaussian (LG) modes which are given as:

$$\begin{aligned}\mathcal{E}_{p}^{l}(r,\phi,z)=\mathcal{E}_{0}\frac{w_{0}}{w(z)}\left(\frac{r\sqrt{2}}{w(z)}\right)^{|l|}L_{p}^{|l|}\left(\frac{2r^{2}}{w^{2}(z)}\right)\exp\left[\frac{ikr^{2}}{2R(z)}-\frac{r^{2}}{w^{2}(z)}\right]\\ \times\exp\left[-i\left(2p+l+1\right)\tan^{-1}\left(\frac{z}{z_{R}}\right)+il\phi\right],\end{aligned} \tag{1.114}$$

where,

$$w(z)=w_{0}\sqrt{1+\left(\frac{z}{z_{R}}\right)^{2}},\quad R(z)=z\left[1+\left(\frac{z}{z_{R}}\right)^{2}\right],\quad\text{and } z_{R}=\frac{\pi w_{0}^{2}}{\lambda}. \tag{1.115}$$

In Eq. (1.114), $\mathcal{E}_0$ is the field amplitude, ϕ is the azimuthal angle, $L_p^{|l|}$ is the generalized Lagurre polynomial, where the indices, l and p are known as the orbital angular momentum (OAM) index and radial index, respectively. In Eq. (1.115), $w(z)$ and $R(z)$ are the beam radius and the radius of curvature of the beam's wavefront at a propagation distance, z, respectively. The parameter, z_R is called the "*Rayleigh length*" [10], it is the propagation distance at which $w(z)=\sqrt{2}w_0$, where, $w_0=w(0)$ is called the beam waist [10]. The concept of OAM index is explained in the next section. For simplicity, we have assumed, the radial index, p to be zero throughout this thesis. Vector beams (VBs) are generated by the vector superposition of two orthogonally polarized LG modes. This results in a heterogeneous distribution of polarization on the transverse plane. The polarization distribution is radially symmetric namely radial, spiral, and azimuthal when the two constituent LG modes have equal and opposite OAM indexes. These types of VBs have a net-zero OAM index and are called cylindrical vector (CV) beams [31]. The polarization distribution has both azimuthal and radial variation, *e.g.*, lemon, star, and web polarization

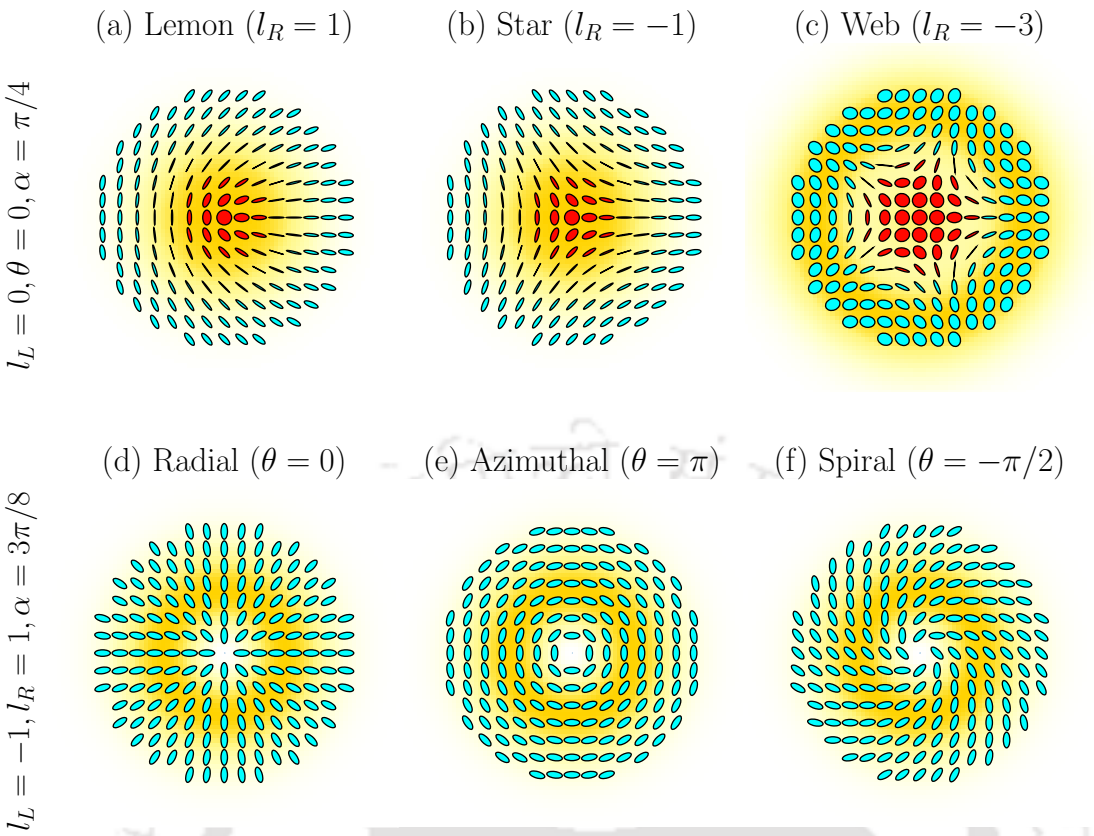

Figure 1.10: Transverse intensity and polarization distribution of (a) Lemon, (b) Star, (c)Web, (d) Radial, (e) Azimuthal, and (f) Spiral vector beams respectively.

distribution when the two LG modes have a zero and a non-zero OAM index, respectively. Such beams are called full Poincaré (FP) beams [32]. In the circular polarization basis, a VB is written as:

$$\vec{E}(r,\phi,z) = \mathcal{E}_L(r,\phi,z)\hat{e}_L + \mathcal{E}_R(r,\phi,z)\hat{e}_R, \tag{1.116}$$

where,

$$\mathcal{E}_L(r,\phi,z) = \cos(\alpha)LG_0^{l_L}, \text{ and } \mathcal{E}_R(r,\phi,z) = e^{i\theta}\sin(\alpha)LG_0^{l_R}, \tag{1.117}$$

are the left and right circularly polarized components of the VB. Here, α and θ determines the relative amplitude and phase between the two modes, respectively, and $LG_0^{l_i}$ $(i = R, L)$ are the LG modes, with the radial index set to zero;

$$LG_0^{l_i}(r,\phi,z) = \mathcal{E}_0\left(\frac{r\sqrt{2}}{w(z)}\right)^{|l_i|}\exp\left[\frac{-r^2}{w(z)^2}\right]\exp\left[\frac{ikr^2z}{2(z^2+z_R^2)}\right] \times \exp\left[il_i\phi - i(|l_i|+1)\tan^{-1}\left(\frac{z}{z_R}\right) + ikz\right]. \tag{1.118}$$

Figure, 1.10 shows the intensity and polarization distribution on the transverse plane of CVBs and FP beams. In the next section we discuss the orbital angular momentum of light and the concept of "*optical singularities*".

1.9.2 Singularities

A singular point is characterized by an undefined physical parameter surrounded by a region of high gradient. For example, the north and south poles are coordinate singularities as longitudes are not defined at these two places. In the next two paragraphs, we will briefly discuss two kinds of singularities encountered in optics.

Phase singularity

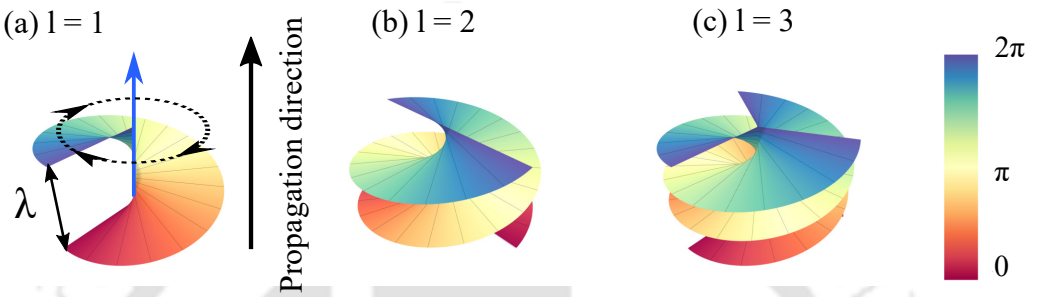

Figure 1.11: (a), (b), (c) Wavefronts of Laguerre-Gaussian beams with radial index, $p = 0$ and OAM index, $l = 1, 2, 3$ respectively.

It is well known that, right (left) circularly polarized light carries a spin angular momentum (SAM) of $+(-)\hbar$ per photon. In 1992, Allen *et al.* [33] discovered that light beams can also carry orbital angular momentum (OAM) [34]. Such beams have a transverse phase distribution of the form, $\exp(il\theta)$ where θ is the azimuthal angle on the beam's transverse plane and l is an integer, called the topological charge or winding number. These beams are a solution to the paraxial wave equation [Eq. (1.112)] and are known as Laguerre-Gaussian modes as mentioned earlier in Sec. 1.9.1. LG modes have two indices attributed to them, one being the index, l associated with OAM of the beam and another index called the radial index, p [Sec. 1.9.1]. The wavefronts of these LG modes are a set of intertwined helicoids [35] as shown in Fig. 1.11 which shows the wavefronts of LG modes for different values of l with $p = 0$. The number and handedness of the helicoids are determined by the value and sign of l, respectively. For example, in Fig. 1.11(a), for $l = +1$ the phase front of the beam consists of one helicoid rotating in an anticlockwise sense when looked at from the top. In Fig. 1.11(a), the circular loop encircling the beam axis (blue arrow) the phase along the azimuthal direction changes by 2π upon propagation for one wavelength, λ as indicated in Fig. 1.11(a). Similarly, for $l = 2(3)$, the phase along the azimuthal direction changes by 2π, two (three) times within one wavelength; generating two (three) helicoids in the process as shown in Figs. [1.11(b), 1.11(c)]. The imaginary circular loop as shown in Fig. 1.11(a) reduces to a point on the beam axis [blue arrow in Fig. 1.11(a)]. The phase at all points on the beam axis can take on any value between 0 and l times 2π, in other words, the phase is undefined. This phase ambiguity is avoided only if the field amplitude is zero on the beam axis. Thus OAM carrying beams are hollow at their beam center, giving the m their doughnut irradiance profile. The aforementioned phenomenon of phase being undefined on the beam axis is known as phase singularity [36] and the

topological index, l is given by:

$$l = \frac{1}{2\pi} \oint \vec{\nabla}\phi \cdot \vec{dl} \tag{1.119}$$

where $\phi(x, y) = l\theta$, is the phase distribution on the beam's transverse plane. In the vicinity of the optic axis (phase singularity), the azimuthal component of phase gradient $\vec{\nabla}\phi$ is maximum and hence the integral, $\oint$ is taken over a closed non-self-intersecting path around the phase singularity (beam axis) in its immediate vicinity.

The phase singularity is also known as a phase vortex or a scalar vortex in literature. The word scalar comes from the fact that phase singularity is associated with phase, which is a scalar quantity. This is true for scalar beams which are a class of beams having a homogeneous distribution of polarization on their transverse plane. On the other hand, vector beams (VBs) that have a non-uniform distribution of polarization on their transverse plane possess polarization singularity, which is discussed in the next section.

Polarization singularity

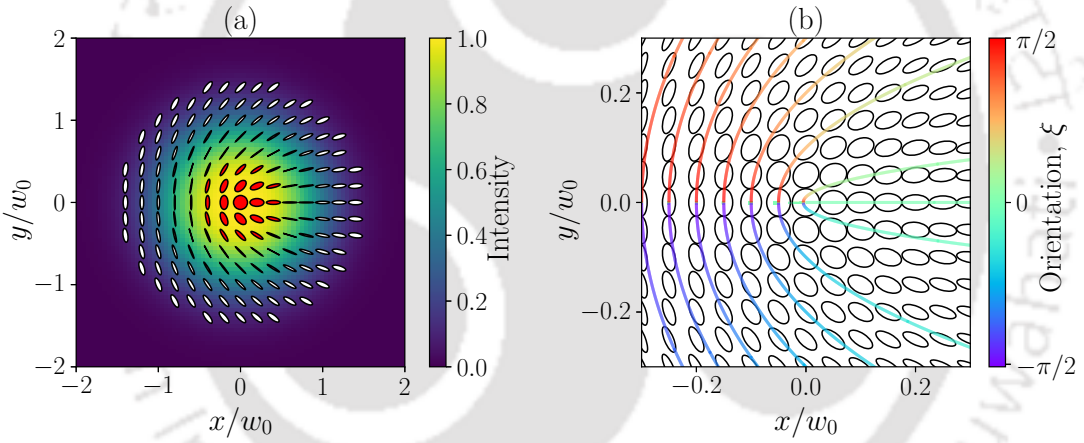

Figure 1.12: (a) Intensity and polarization distribution on the transverse plane of a "lemon" VB. (b) Streamlines of the polarization orientation field, $\xi(x, y)$ for a "lemon" vector beam, overlaid with its polarization distribution. In Fig. 1.13(a), the polarization ellipses filled in red color are right-handed (RH) while those filled with white color are lefthanded (LH) and the black straight lines represent linear polarization.

Similar to phase singularity, there is polarization singularity [36] which is associated with vector beams. Vector beams have a nonuniform distribution of polarization on the transverse plane as shown in Fig. 1.12(a), which shows the intensity and polarization distribution on the transverse plane of a "lemon" vector beam. Figure 1.12(b) shows a zoomed plot consisting of polarization ellipses around the beam center and streamlines associated with the polarization ellipse orientation field, $\xi(x, y)$. In Figs. 1.12(a), 1.12(b), at the beam center (or beam axis), the eccentricity of the polarization ellipse is 0, *i.e.*, the polarization state is circular. This means the polarization orientation, $\xi(0, 0)$ with respect to say, x axis is undefined, such a singularity is known as C-point singularity (C stands for circular). Just like phase singularity,

polarization singularity also has its index, *e.g.* C-point singularity has a C-point singularly index, I_C associated with it which is given by:

$$I_C = \frac{1}{2\pi} \oint \vec{\nabla}\xi \cdot \vec{dl} \tag{1.120}$$

The integral, $\oint$ is taken over a closed non-self-intersecting path around the polariza-

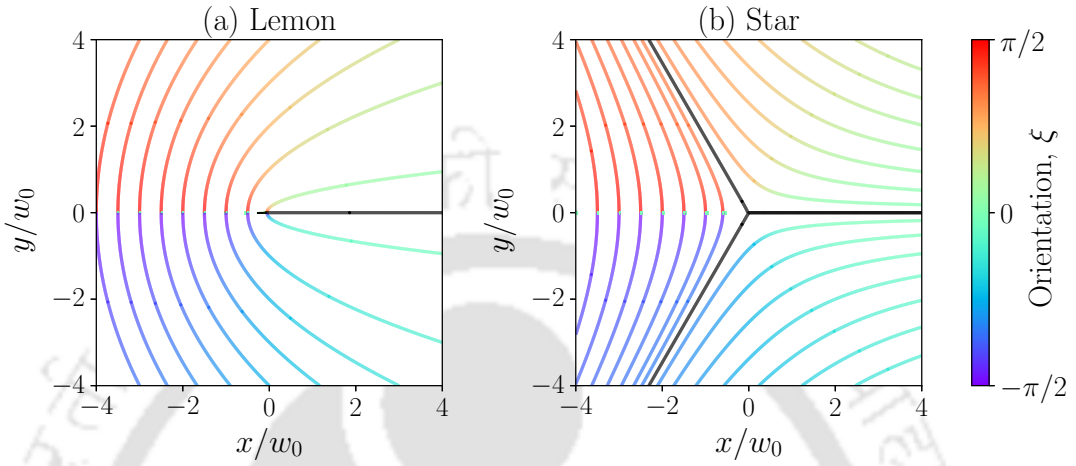

Figure 1.13: (a), (b) Streamlines of "Lemon" and "Star" vector beam respectively. Here, w_0 is simply a normalization parameter.

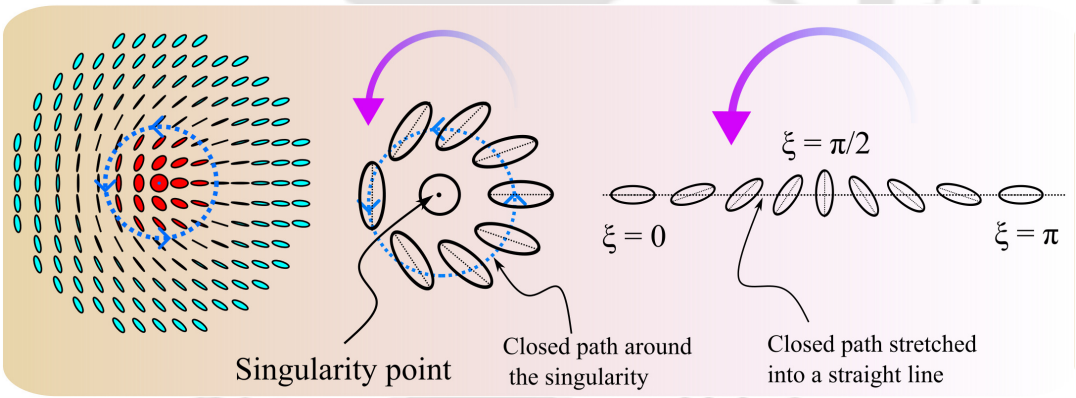

Figure 1.14: Figure illustrating the meaning of C-point singularity index, I_C.

tion singularity in its immediate vicinity. The C-point singularity index of "lemon" VB is $I_C = +1/2$. Figures 1.13(a), 1.13(b) shows a comparison between the streamlines of the polarization orientation field, $\xi(x, y)$ for "lemon" and "star" VBs respectively. For a "star" VB shown in Fig. 1.13(b) $I_C = -1/2$ and unlike "lemon" VB, it has three lines (black colored lines in Fig. 1.13) ending on the singularity instead of one. The index, I_C gives the amount of rotation the polarization ellipse undergoes around a polarization singularity. For example, $I_C = 1/2$ for "lemon" VB means that orientation of the polarization ellipses changes by $I_C \times 2\pi = \pi$ along a closed path around the singularity as shown in Fig. 1.14. Unlike phase singularity, C-point singularity doesn't require the intensity to be zero at the singularity as can be seen in Fig 1.12(a). Beams such as the "lemon" VB, have a polarization distribution

of predominantly elliptical polarization, and thus are called ellipse fields. Another kind of field known as vector field has a non-uniform distribution of linear polarization. The singularity associated with vector fields is known as V-point singularity. V-point singularity occurs always occurs at intensity null just like phase singularity. Whereas C-point singularity can occur at any intensity as evident from Fig. 1.12(a). A comprehensive discussion on optical singularities is outside the purview of this thesis; however, the review article by Ruchi *et al.* [36] should suffice to give a general idea of optical singularities.

Applications of vector beam

VBs have drawn great attention for their varied applicability, *e.g.*, CV beams can produce a strong longitudinal field component [37] at the focus of a high numerical aperture (NA) lens, producing a spot size as small as $0.16\lambda^2$[38]. This focusing property of CV beams has applications in single-molecule spectroscopy, STED [39], confocal microscopy [40, 41, 42], efficient laser cutting [43],optical trapping of particles [44, 45], and atomic magnetometry [46, 47]. A high dimensional Hilbert space based on the polarization and OAM of a VB [48] can be leveraged to encode single-photon qubits for applications in quantum information [49, 50, 51]. In free space optical communication, the transverse polarization distribution of vector modes can be used to increase the transmission data rate [52]. The spatial degree of freedom of scaler OAM beams has been used to increase information content [53] in optical communication. However, scaler OAM beams bifurcate into multiple spatial solitons during nonlinear propagation [54, 55]. This fragmentation [56, 57, 58] can be prevented by using VBs, *e.g.*, CV beams can propagate in a saturable Kerr nonlinear medium for longer distances than scalar beams, without breakup [59].

The succeeding four chapters are dedicated to the four research problems included in this thesis.

Chapter 2

Shape preserving atomic pulse amplifier

2.1 Introduction

Light pulse generation, reshaping and shape preserving propagation has received considerable attention in multilevel atomic systems due to its potential applications in optical communication and information sciences [60, 61, 62]. Population inversion [63] and atomic coherences are two main constituents for the pulse generation and reshaping [64]. Coherently controlled light-matter interaction can produce desired atomic coherences and population among the various level systems. A variety of techniques based on stimulated Raman adiabatic processes (STIRAP)[65], EIT, coherent population trapping (CPT)[66], and saturated absorption [67] has been adopted to control the dynamics of population and coherences effectively. The induced coherence among the lower level states of a molecular system [68] or atomic system [69] are the central issue of producing pulse radiations. Various techniques have been proposed for the generation of optical pulses [70, 71].

Self induced transparency (SIT) is a prominent example for shape preserving ultrashort optical pulses propagating through a resonant medium [72, 73]. The physical explanation of SIT comes from re-radiation of atoms from the excited state of the two level system in the presence of pulse power which is beyond some critical value [73]. This lossless shape preserving propagation can be extended to two pulses in an otherwise opaque three level medium which are referred to as simultons [74]. Remarkably, the two pulses may copropagate as complementary pulse shapes in a three level Λ-system which is dictated by the input envelope shape [75]. An extensive study on co-existence of stable propagation of sech and tanh pulse envelopes have been investigated in three- and multilevel systems [76, 77, 78, 79, 80].

The three-level Λ configuration also offers the temporal cloning of an arbitrary shaped strong pulse envelope on to a weak field [81]. The predictions of simultons [74] have been experimental verified in a V-type thermal atomic system referred to as a quasisimulton [82]. In these studies, radiative and non-radiative decay is not taken into consideration due to the short duration of the pulse. However, the influence of various atomic relaxation processes plays a crucial role on spectral bandwidth of the generated pulse and the propagation velocity [83]. The weak probe pulse along with strong control field propagate as matched pulses through an absorptive medium [84]. All of these studies mostly requires optical pulses to be of some very specific

input forms or definite energy in order to demonstrate shape preserving propagation throughout the length of the medium [85].

Media which exhibit huge absorption, limits any realistic application based on pulse generation and shape preserving propagation. The absorptive medium accompanied by its inherent pulse broadening, distortion as well as suppression of output transmission, practically stops its usage [86]. Hence coherent manipulation of absorption of the medium is essential for arbitrary shaped optical-pulse propagation with controllable width and gain [87, 88]. Much attention has been paid to make an opaque medium transparent for supporting propagation of pulses without changing their initial profiles [89, 90, 91]. Nonetheless, most of the studies failed to support the long distance propagation of arbitrary shaped optical pulse. In this work we investigate the propagation of an arbitrary shaped probe pulse through the three level Λ system in presence of a strong continuous control field. Both the probe and control field experience absorption during initial length of propagation. However, the probe pulse is progressively amplified and retains its initial shape. The population transfer from ground state to excited state due to control field is the main reason behind the continuous energy transfer to the probe field. With suitable choice of parameters, the probe pulse retains its initial shape and propagates without any delay, distortion and absorption, after the amplification process. Conventionally the gain system manifests an instability due to the interplay between non-linearity and anomalous dispersion [92, 93], nevertheless the proposed system is immune from instability. The transmitted probe pulse display broadening which is in contrast to the gain associated with pulse narrowing [88].

The perspective of the current scheme is substantially different from the existing techniques in the following way. Usually shape preserving, distortion free pulse propagation is associated with a specific temporal shape such as sech, and is generated in a nonlinear medium by balancing the effects of dispersion and self-phase modulation [11]. SIT scheme requires the pulse area to be an integral multiple of 2π to achieve shape preserving, distortion free pulse propagation [72]. Again active Raman gain scheme [94] can be used to amplify a Gaussian pulse as well as produce solitons [95]. Raman scheme requires specific form of the input and also the signal to travel for a longer distance inside the gain media to achieve significant amplification and for the effects of nonlinearity to balance dispersion to produce stable solitons. Finally, chirped pulse amplification (CPA) method can be used for ultra-short pulse amplification by employing clever instrumental techniques that are applied outside the gain medium [96]. These processes are sensitive to the angle between signal and pump beams for phase-matching geometry. Our proposed scheme is based on intrinsic transient gain phenomena that can overcome above issues such as fine balance between non-linearity and dispersion of the medium, specific shape of input envelope, and strict phase-matching constraints, in order to form amplified stable shape preserving pulses. The broadening of the pulse during the amplification process can be beat by using compressors. Hence our scheme is able to amplify, propagate complicated pulse shapes without any dispersion, absorption and distortion.

This chapter is organized as follows. Sec. 2.2 contains the theoretical formulation of the relevant level system. Sec. 2.3 contains the results of numerical simulations along with detailed explanations. Sec. 2.4 contains the summary and conclusion.

2.2 Theoretical formulation

2.2.1 Level system

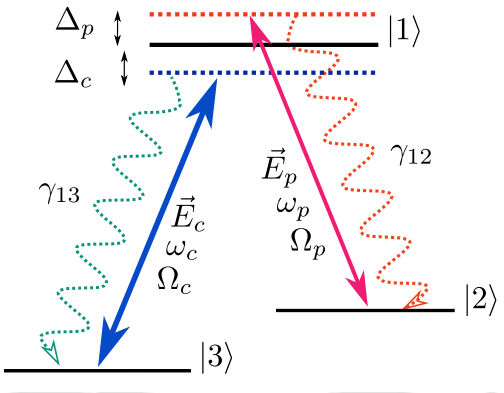

Figure 2.1: Schematic diagram of a three level Λ-system. Here, $|1\rangle$ is the excited state, $|2\rangle$ is an intermediate meta stable state and $|3\rangle$ the ground state with energy set to zero. The atomic transitions $|1\rangle \leftrightarrow |2\rangle$ and $|1\rangle \leftrightarrow |3\rangle$ are coupled by a weak probe field $\vec{E}_p$, with frequency ω_p, and a strong control field $\vec{E}_c$, with frequency ω_c, respectively. The spontaneous emission decay rate of $|1\rangle$ to $|j\rangle$ $(j \in 2, 3)$ transition is denoted by γ_{1j}. The detunings, and Rabi frequencies of the fields are denoted by Δ_i, and Ω_i, respectively ($i \in p, c$ represents probe and control field, respectively).

A Λ-system as shown in Fig. 2.1 can meet the desired criteria for achieving gain by considering that all population is kept at ground state $|3\rangle$ initially. Unlike the absorption based EIT configuration, in Fig. 2.1, the ground state $|3\rangle$ and excited state $|1\rangle$ are coupled by a strong control field $\vec{E}_c$ and the metastable state $|2\rangle$ and $|1\rangle$ are coupled by a weak probe field $\vec{E}_p$. This configuration leads to population transfer from $|3\rangle$ to $|1\rangle$ which spontaneously decays to $|2\rangle$. The decay from $|1\rangle$ to $|2\rangle$ makes provision for the probe field being resonantly enhanced by stimulated emission in presence of the control field, causing probe amplification. The three level Λ system in Fig. 2.1 can be realized with the ^{87}Rb D_2 $(5^2S_{1/2} \rightarrow 5^2P_{3/2})$ transition hyperfine structure, by considering the Zeeman sub-levels of the ground state hyperfine levels as, $|3\rangle = |5^2S_{1/2}, F = 1, m_F = -1\rangle$, $|2\rangle = |5^2S_{1/2}, F = 1, m_F = +1\rangle$, and the excited state as $|1\rangle = |5^2P_{3/2}, F = 0, m_F = 0\rangle$. The probe and control fields are considered to be propagating along z direction such that, under the plane wave approximation, the fields are defined as:

$$\vec{E}_j(r,t) = \hat{e}_j \mathcal{E}_j(r,t) e^{-i(\omega_j t - \vec{k}_j.\vec{r})} + \text{c.c.}, \tag{2.1}$$

where $\hat{e}_j$ are the unit polarization vectors, $\mathcal{E}_j(r,t)$ are the slowly varying envelope functions, ω_j are the field carrier frequencies and $\vec{k}_j = k_j \hat{z}$ are the wave vectors of the fields. The index $j \in p, c$ represents probe and control fields, respectively.

The time dependent Hamiltonian of the system, under the electric dipole approximation is given as:

$$\boldsymbol{H} = \boldsymbol{H}_0 + \boldsymbol{H}_I, \tag{2.2a}$$

$$\boldsymbol{H}_0 = \hbar(\omega_{13}|1\rangle\langle 1| + \omega_{23}|2\rangle\langle 2|), \tag{2.2b}$$
$$\boldsymbol{H}_I = |1\rangle\langle 2|\vec{\boldsymbol{d}}_{12}.\hat{e}_p\boldsymbol{\mathcal{E}}_p e^{-i(\omega_p t - k_p z)} + |1\rangle\langle 3|\vec{\boldsymbol{d}}_{13}.\hat{e}_c\boldsymbol{\mathcal{E}}_c e^{-i(\omega_c t - k_c z)} + \text{h.c.}, \tag{2.2c}$$

where ω_{j3} $(j \in 1, 2)$ denotes the resonance frequency of $|j\rangle \leftrightarrow |3\rangle$ transition and $\vec{\boldsymbol{d}}_{j3} = \langle j|\hat{\boldsymbol{d}}|3\rangle$ are matrix elements of the dipole moment operator $\hat{\boldsymbol{d}}$, representing the induced dipole moments, corresponding to $|j\rangle \leftrightarrow |3\rangle$ transition. To write the Hamiltonian in a time independent form, the following unitary transformation is used:

$$\boldsymbol{U} = e^{-i\boldsymbol{V}t}, \tag{2.3a}$$
$$\boldsymbol{V} = \omega_c|1\rangle\langle 1| + (\omega_c - \omega_p)|2\rangle\langle 2|. \tag{2.3b}$$

The effective Hamiltonian obeying the Schrödinger equation in the transformed basis is given as:

$$\mathcal{H} = \boldsymbol{U}^\dagger \boldsymbol{H}\boldsymbol{U} - \frac{i}{\hbar}\boldsymbol{U}^\dagger\frac{\partial \boldsymbol{U}}{\partial t}, \tag{2.4}$$

which under **RWA** (Rotating wave approximation) gives

$$\frac{\mathcal{H}}{\hbar} = -\Delta_c|1\rangle\langle 1| - (\Delta_c - \Delta_p)|2\rangle\langle 2| - \Omega_p|1\rangle\langle 2| - \Omega_c|1\rangle\langle 3| + \text{h.c.}. \tag{2.5}$$

The single photon detunings for the probe and control fields are defined as:

$$\Delta_p = \omega_p - \omega_{12}, \quad \Delta_c = \omega_c - \omega_{13}, \tag{2.6}$$

and the Rabi frequencies of probe and control fields are written as:

$$\Omega_p = \frac{\vec{\boldsymbol{d}}_{12}.\hat{e}_p\boldsymbol{\mathcal{E}}_p}{\hbar}e^{ik_p z}, \quad \Omega_c = \frac{\vec{\boldsymbol{d}}_{13}.\hat{e}_c\boldsymbol{\mathcal{E}}_c}{\hbar}e^{ik_c z}. \tag{2.7}$$

The dynamics of atomic state populations and coherences is governed by the following Liouville equation:

$$\frac{\partial \rho}{\partial t} = -i\hbar[\mathcal{H}, \rho] + \mathcal{L}_\rho. \tag{2.8}$$

The Liouville operator $\mathcal{L}_\rho$, describes all incoherent processes and can be expressed as:

$$\mathcal{L}_\rho = -\sum_{j=2}^{3}\frac{\gamma_{1j}}{2}\left(|1\rangle\langle 1|\rho - 2|j\rangle\langle j|\rho_{ii} + \rho|1\rangle\langle 1|\right), \tag{2.9}$$

where γ_{1j} represent the radiative decay rates from excited state $|1\rangle$ to $|j\rangle$. The radiative decay rate form $|2\rangle$ to $|3\rangle$ is dipole forbidden and thus $\gamma_{23} = 0$ for the Λ system in Fig. 2.1.

The equations of motion for atomic state populations and coherences of the three level Λ-system are then given as:

$$\dot{\rho}_{11} = -\Gamma\rho_{11} + i(\Omega_p\rho_{21} - \rho_{12}\Omega_p^*) + i(\Omega_c\rho_{31} - \Omega_c^*\rho_{13}), \tag{2.10a}$$
$$\dot{\rho}_{12} = -\left(\frac{\Gamma}{2} - i\Delta_p\right)\rho_{12} + i\Omega_c\rho_{32} + i\Omega_p(\rho_{22} - \rho_{11}), \tag{2.10b}$$
$$\dot{\rho}_{13} = -\left(\frac{\Gamma}{2} - i\Delta_c\right)\rho_{13} + i\Omega_c(\rho_{33} - \rho_{11}) + i\Omega_p\rho_{23}, \tag{2.10c}$$
$$\dot{\rho}_{22} = \gamma_{12}\rho_{11} + i(\Omega_p^*\rho_{12} - \rho_{21}\Omega_p), \tag{2.10d}$$

$$\dot{\rho}_{23} = -\Big[\Gamma_{23} - i(\Delta_c - \Delta_p)\Big]\rho_{23} + i(\Omega_p^*\rho_{13} - \Omega_c\rho_{21}), \tag{2.10e}$$

$$\dot{\rho}_{33} = \gamma_{13}\rho_{11} + i(\rho_{13}\Omega_c^* - \Omega_c\rho_{31}), \tag{2.10f}$$

$$\rho_{ij}^* = \rho_{ji}, \tag{2.10g}$$

with initial conditions

$$\rho_{11}(z,0) = \rho_{22}(z,0) = 0, \text{ and } \rho_{33}(z,0) = 1.$$

Assuming that the system is closed, the total population remains conserved; *i.e.*, $\rho_{11} + \rho_{22} + \rho_{33} = 1$. In (2.10), the overdots stand for time derivatives and "$*$" denotes complex conjugate. The decoherence rate of ρ_{23} is denoted by Γ_{23} and the total decay rate of excited state $|1\rangle$ is written as $\Gamma = \gamma_{12} + \gamma_{13}$. The decay rate of excited state $|1\rangle$, to states $|2\rangle$ and $|3\rangle$ are assumed to be equal; *i.e.*, $\gamma_{12} = \gamma_{13} = \gamma$.

2.2.2 Propagation equations

In order to explore the effects of populations and coherences on the propagation dynamics of probe pulse through the gain medium, the study of Maxwells equation is inevitable. Under the slowly varying envelope approximation, the propagation equations for the probe and control fields can be expressed as:

$$\left(\frac{\partial}{\partial z} + \frac{1}{c}\frac{\partial}{\partial t}\right)\Omega_p(z,t) = i\eta_p\rho_{12}(z,t), \tag{2.11a}$$

$$\left(\frac{\partial}{\partial z} + \frac{1}{c}\frac{\partial}{\partial t}\right)\Omega_c(z,t) = i\eta_c\rho_{13}(z,t), \tag{2.11b}$$

where η_i $(i \in p, c)$ are called the coupling constants of the respective fields. For practical purposes, the resonance frequencies of $|1\rangle \rightarrow |j\rangle$ $(j \in 2, 3)$ transitions can be assumed to be equal; *i.e.*, $\omega_{12} = \omega_{13}$. This makes $\eta_p = \eta_c = \eta$ with $\eta = 3N\lambda^2\gamma/8\pi$, where N is the number of atoms per unit volume inside the medium and λ is the wavelength of the fields. To facilitate numerical integration of (2.11), a frame moving at the speed of light in vacuum, c is used. The necessary coordinate transformations for that are $\tau = t - z/c$ and $\zeta = z$. This allows for the round bracketed terms of (2.11) to be replaced by partial derivatives with respect to the single independent variable ζ.

2.3 Numerical Results

In this section, we present the results obtained from numerically solving the coupled Maxwell-Bloch equations, (2.11a) and (2.11b). At first we consider the probe and control fields to be a Gaussian pulse and continuous wave (CW) field respectively, at the entrance of the medium, *i.e.*, at $z = 0$, the two fields are defined as:

$$\Omega_p(0,\tau) = \Omega_p^0 \exp\left[-\frac{(\tau - \tau_0)^2}{2\sigma_0^2}\right], \quad \Omega_c(0,\tau) = \Omega_c^0, \tag{2.12}$$

where, Ω_p^0, Ω_c^0 are the amplitudes of probe and control fields respectively and σ_0, τ_0 are the initial pulse width and peak position of the probe pulse, respectively. The

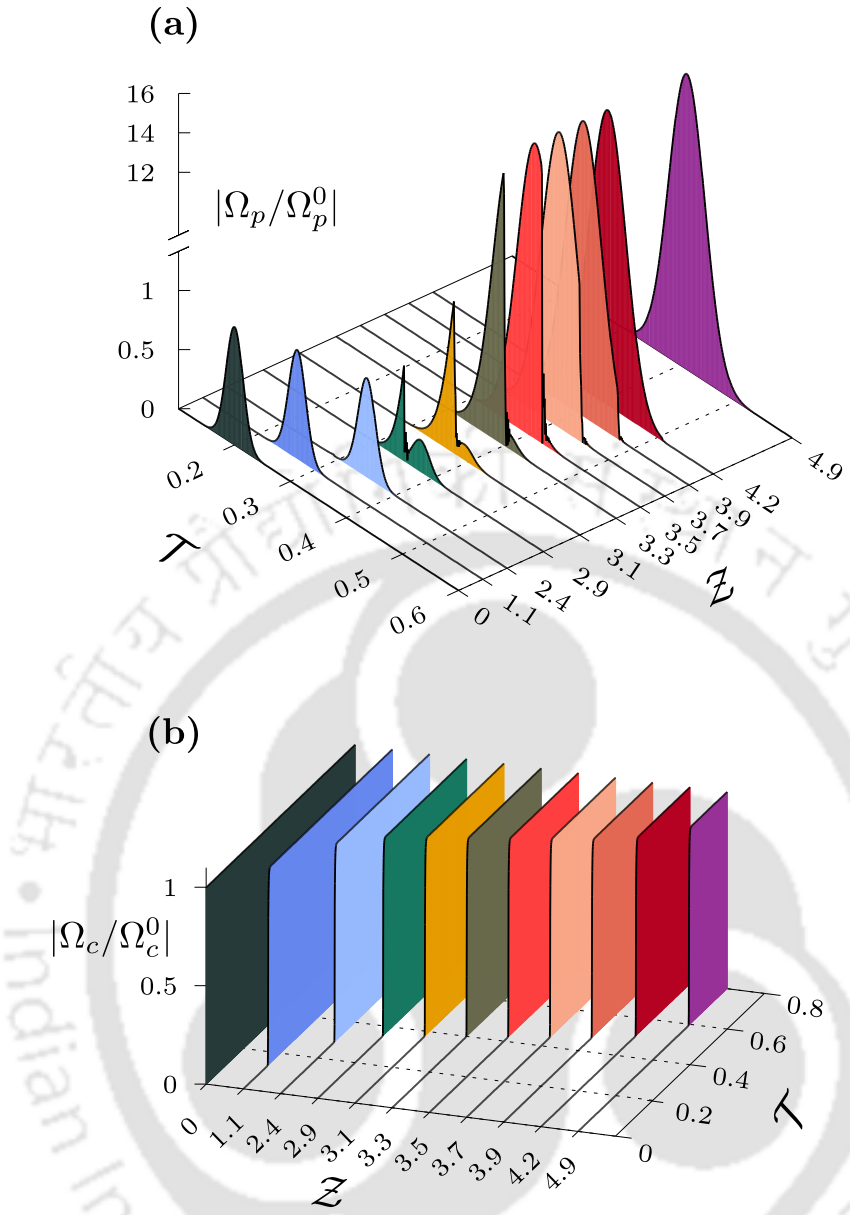

Figure 2.2: (a) Temporal profile of probe pulse at different propagation lengths $\mathcal{Z}$. (b) Temporal profile of control field corresponding to the propagation lengths mentioned in Fig. 2.2(a). Parameters used are: $\Omega_p^0 = 0.01\gamma$, $\Omega_c^0 = 4\gamma$, $\tau_0 = 200/\gamma$, $\sigma_0 = 15/\gamma$, $\Delta_p = \Delta_c = 0$, and $\Gamma_{23} = 0.001\gamma$. Field magnitudes are normalized by their respective field magnitudes at $\mathcal{Z} = 0$. Note that the $\mathcal{Z}$ axis is not made to scale for visibility purpose.

results are curated in Fig. 2.2, where the temporal profiles of probe and control fields are plotted at different propagation lengths. Throughout this chapter, time, and propagation length are normalized, made dimensionless as $\mathcal{T} = \gamma\tau \times 10^{-3}$ and $\mathcal{Z} = \eta\zeta/\gamma \times 10^{-3}$ respectively.

Both the probe pulse and the CW control field undergo observable reshaping during propagation. In Fig. 2.2(a), from $0 \leq \mathcal{Z} \leq 2.4$, the probe pulse experiences group delay, absorption and indiscernible broadening with increasing propagation length. From $2.4 \leq \mathcal{Z} \leq 4.2$, the probe undergoes substantial reshaping and am-

plification. Beyond $\mathcal{Z} \geq 4.2$, a broadened and amplified Gaussian probe pulse is obtained, which travels at the speed of light in vacuum, without experiencing any delay, absorption and dispersion. In Fig. 2.2(b), the control field undergoes absorption at its leading end as it propagates though the medium, giving it an appearance of experiencing delay at the leading end. The explanation for the results in Fig. 2.2 are provided in the following sections.

2.3.1 Absorption of control field

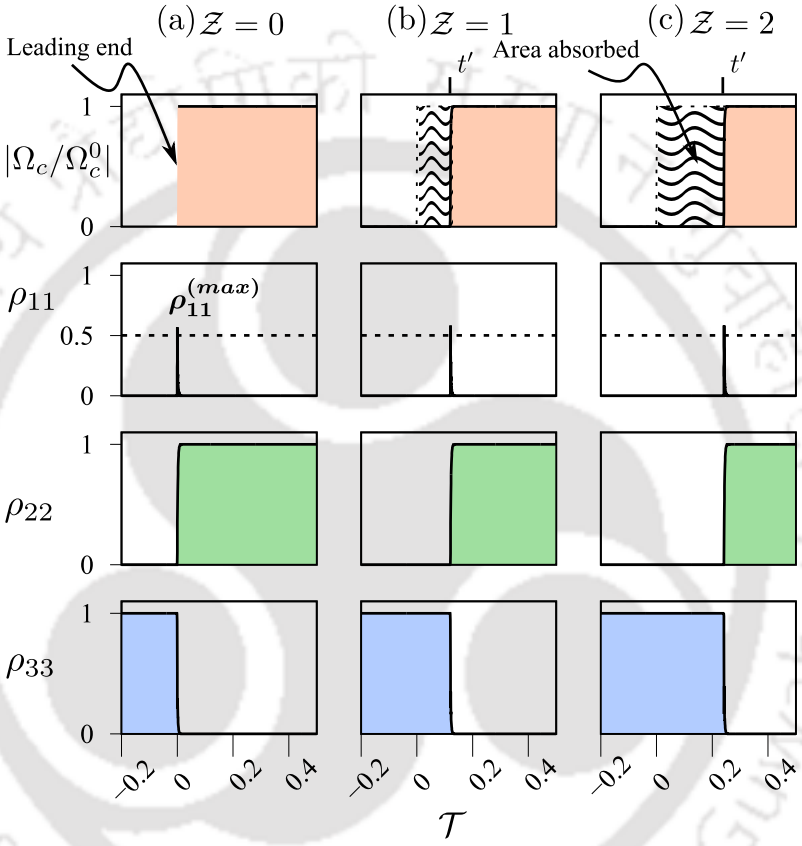

Figure 2.3: Temporal profile of control field and corresponding population distribution are plotted column wise at propagation lengths $\mathcal{Z} = 0$, 1, and 2 in (a), (b), (c), respectively. In the 1st row, t' represents the position of control field's leading end on time axis, $\mathcal{T}$ at any given propagation length, $\mathcal{Z}$. Control field magnitude normalization and parameters used are same as Fig. 2.2. Figures pertaining to a particular row and column have a common vertical and horizontal axes, respectively.

In the 1st row of Fig. 2.3(a), the control field is switched on at time $\mathcal{T} = 0$, at the entrance of the medium ($\mathcal{Z} = 0$). For time, $\mathcal{T} < 0$, all population is assumed to be in ground state $|3\rangle$ as shown in 3rd row of Fig. 2.3(a). The control field being resonant to $|3\rangle \leftrightarrow |1\rangle$ transition, causes a transient population transfer from ground state $|3\rangle$ to the excited state $|1\rangle$ in the vicinity of its "leading end", as shown in 2nd row of Fig. 2.3(a). Here, by "leading end" we simply mean the end of control field which arrives at $\mathcal{Z} = 0$, earliest in time as indicate in 1st row of Fig. 2.3(a). The transient population transfer from state $|3\rangle$ to $|1\rangle$ occurs within an infinitesimally

small time interval and after that the population decays to the metastable state $|2\rangle$, causing the transfer of all population from the ground state $|3\rangle$ to $|2\rangle$ as shown in 3$^{\text{rd}}$ and 4$^{\text{th}}$ row of Fig. 2.3(a). This whole process results in tiny absorption of control field energy from its "leading end". After the entire population is transferred from state $|3\rangle$ to $|2\rangle$, there is no absorption of the control field in the $|3\rangle \leftrightarrow |1\rangle$ channel, *i.e.*, in Fig. 2.3(a), from time, $\mathcal{T} = 0$ to ∞, there is no absorption of control field, due to the population of state $|3\rangle$ being zero from time, $\mathcal{T} = 0$ to ∞. The entire process illustrated in Fig. 2.3(a), repeats with each infinitesimal increment in the propagation length $\mathcal{Z}$, causing a tiny absorption of control field energy from its "leading end" at each step. Therefore, as $\mathcal{Z}$ increases, slices of control field area (in other words, energy) from its leading end gets absorbed (removed), giving it an appearance of experiencing delay as shown in 1$^{\text{st}}$ row of Figs. 2.3(b) and 2.3(c). If t' [see 1$^{\text{st}}$ row of Fig. 2.3(b) and 2.3(c)] represents the position of control field's "leading end" on time axis, $\mathcal{T}$ at any given propagation distance, $\mathcal{Z}$, then the amount of control field energy absorbed by the medium after propagating a distance $\mathcal{Z}$ would be proportional to the area, $\int_0^{t'} |\Omega_c/\Omega_c^0| d\mathcal{T}$ [see the wavy pattern in 1$^{\text{st}}$ row of Fig. 2.3(b) and 2.3(c)]. Notice once again, in Figs. 2.3(b) and 2.3(c), from time, $\mathcal{T} = t'$ to ∞, there is no absorption of control field, due to the population of state $|3\rangle$ being zero from time, $\mathcal{T} = t'$ to ∞. Hence, there is no depletion of control field's amplitude during propagation. Similar absorption phenomenon has been reported by Harris *et al.* [97], where they considered a Gaussian pulse instead of the time independent CW field considered here. The absorption of control field as shown in Fig. 2.3, was found to be linear with increasing propagation length, $\mathcal{Z}$. This conclusion can be made from Fig. 2.4, where the graph between the position of control field's leading end (t') on time axis vs $\mathcal{Z}$ gives a straight line.

A formula for the slope of the graph in Fig. 2.4 can be derived as follows. The energy density of control field is given as $|\mathcal{E}_c|^2/8\pi$. Therefore, if A is the area of cross section of the control laser beam, then the energy passing through the transverse plane at any given z, for a time interval say, $\tau' = t'/\gamma \times 10^3$ (see the definition of

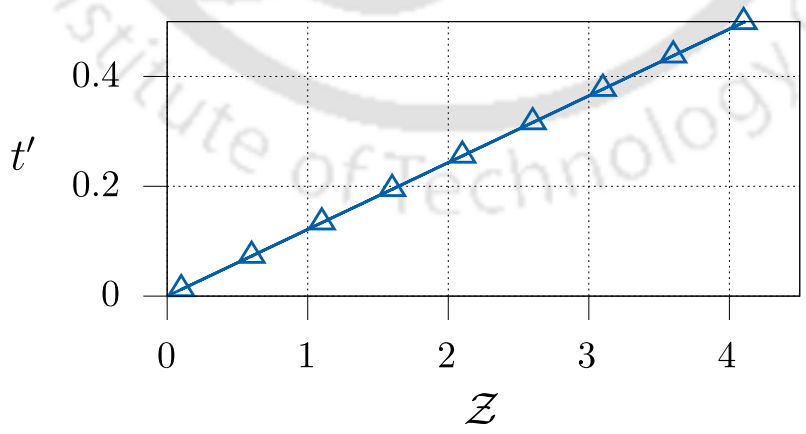

Figure 2.4: Position of control field's leading end t', on time axis ($\mathcal{T}$) vs propagation length, $\mathcal{Z}$. The slope of the graph, $\beta \approx 0.12168$, is the rate at which the control field's leading end appears to move forward along time axis, $\mathcal{T}$ with increasing $\mathcal{Z}$. Parameters used are same as Fig. 2.2.

normalized, dimensionless time, in 1st para. of sec. 2.3) is:

$$\int_0^{\tau'} \frac{cA|\mathcal{E}_c|^2}{8\pi} d\tau, \tag{2.13}$$

which is also the amount of control field energy that gets absorbed after propagating for a distance z, inside the medium. Now, let $\rho_{11}^{(max)}$ [see 2nd row of Fig. 2.3(a)] be the maximum value of the fraction of population that gets excited from the ground state $|3\rangle$ to excited state $|1\rangle$, due to the absorption of control field from its "leading end", at a propagation distance, z. Each atom can absorb only one control field photon of energy $\hbar\omega_{13}$, therefore inside a homogeneous medium with atomic number density N, the total control field energy absorbed by the medium would be:

$$E = \hbar\omega_{13}\rho_{11}^{(max)} NAz. \tag{2.14}$$

Equating Eqs. (2.13) and (2.14), and after some simple algebra; $t'(\mathcal{Z})$ and $\mathcal{Z}$ can be related as:

$$t' = \frac{4 \times \rho_{11}^{(max)}}{|\Omega_c/\gamma|^2} \mathcal{Z}. \tag{2.15}$$

From Fig. 2.3, we can roughly assume $\rho_{11}^{(max)} = 1/2$. Thus, from (2.15), the theoretical slope of t' vs $\mathcal{Z}$ plot is approximately, $\beta_{th} = 2/|\Omega_c/\gamma|^2$. The slopes obtained numerically (β_{nu}) for different input control magnitudes were found to be close to the theoretical (β_{th}) ones. As can be seen in Table 2.1, the ratio $\beta_{th}/\beta_{nu} \approx 1$, over a range of input control field Rabi frequency, thus countenancing the correctness of the numerical simulation. However, it is important to note that the value of $\rho_{11}^{(max)}$ need not necessarily be 1/2. The value of $\rho_{11}^{(max)}$ was found to have direct dependence on the input control field intensity. In general, higher the input control field intensity; higher is the value of $\rho_{11}^{(max)}$. Due to complicated time dependency of optical Bloch equation, an analytical formula for $\rho_{11}^{(max)}$ is intractable.

Table 2.1: Table showing comparison between β_{nu} and β_{th}

Ω_c^0/γ	β_{nu}	β_{th}	β_{th}/β_{nu}
2	0.492	0.5	1.02
3	0.219	0.22	1.00
4	0.123	0.125	1.02
5	0.077	0.08	1.04
6	0.053	0.056	1.06
7	0.039	0.041	1.05

2.3.2 Probe delay, dispersion and absorption

The probe pulse travels incontrovertibly under the influence of control field from $0 \leq \mathcal{Z} \leq 2.4$ as shown in Fig. 2.5 (1st row). The presence of control field creates a population distribution of $\rho_{11} = \rho_{33} = 0, \rho_{22} = 1$ as shown in Fig. 2.5 (2nd, 3rd, and 4th row), which serves as an absorbing, dispersive medium for the probe pulse. Hence, the probe undergoes noticeable absorption and delay within $0 \leq \mathcal{Z} \leq 2.4$ as shown in Figs. 2.5(a) - 2.5(c). The probe absorption coefficient, α' can be calculated

from the imaginary part of the probe susceptibility, χ of the medium. The probe susceptibility, χ is written in terms of the atomic coherence as:

$$\chi = \frac{\eta'}{\Omega_p}\rho_{12} \quad \left(\eta' = \frac{3N\lambda^3\gamma}{32\pi^3}\right), \tag{2.16a}$$

$$\rho_{12} = \frac{-\Omega_p\left[|\Omega_p|^2 + \gamma(\gamma_{23} - i\Delta_p)\right]}{(\gamma - i\Delta_p)\left[\gamma(\Delta_p + i\gamma_{23}) + i|\Omega_p|^2\right] + i\gamma|\Omega_c|^2}, \tag{2.16b}$$

where ρ_{12}, in (2.16b), comes from the steady state solutions of (2.10) with $\Delta_c = 0$, under the weak probe ($\Omega_p^0 \ll \Omega_c^0$) approximation. The steady state boundary condition used for the derivation of (2.16b) is $\rho_{11} = \rho_{33} = 0$, and $\rho_{22} = 1$ as evident from Fig. 2.5 (1^{st} column). The probe absorption coefficient is defined as $\alpha' = 2\pi\omega\text{Im}[\chi]/c$, which is made dimensionless as $\alpha^{(d)} = \gamma\alpha'/\eta$. At two photon resonance ($\Delta_p = \Delta_c = 0$),

$$\alpha^{(d)} = 1 - \frac{|\Omega_c|^2}{\gamma\gamma_{23} + |\Omega_c|^2 + |\Omega_p|^2}. \tag{2.17}$$

For the parameters mentioned in Fig. 2.2, $\alpha^{(d)} \approx 6.9 \times 10^{-5}$, which is close to the value obtained numerically, 6.5×10^{-5}. It is well known that, after propagating for a distance, z inside an absorbing, dispersive medium, a Gaussian pulse of the form:

$$\Omega_p(0,t) = \Omega_p^0 \exp\left[\frac{-t^2}{2\sigma_0^2}\right], \tag{2.18}$$

gets modified as:

$$\Omega_p(z,t) = \Omega_p^0\sqrt{\frac{\sigma_0^2}{\sigma_0^2 - ik_0''z}}\exp\left[\frac{-(t-k_0'z)^2}{2(\sigma_0^2 - ik_0''z)} - \alpha' z\right], \tag{2.19}$$

where $k_0' = \frac{\partial k(\omega)}{\partial\omega}\big|_{\omega_0}$ and $k_0'' = \frac{\partial^2 k(\omega)}{\partial\omega^2}\big|_{\omega_0}$ with $k(\omega)$ and ω_0 being the propagation vector and carrier frequency of the field, respectively. Equation (2.19) shows that the Gaussian pulse gets delayed by a time, $\tau_d = k_0'z$ and the pulse width gets modified as $\sigma^2(z) = \sigma_0^2 - ik_0''z$, after traveling a distance z inside any dispersive medium. The parameters k_0' and k_0'' are written in terms of the probe susceptibility χ, as:

$$k_0' = \left(1 + 2\pi\omega\frac{\partial\chi}{\partial\omega}\bigg|_{\omega_0}\right)/c, \quad k_0'' = \frac{2\pi\omega_0}{c}\frac{\partial^2\chi}{\partial\omega^2}\bigg|_{\omega_0}, \tag{2.20}$$

which are made dimensionless as $\kappa_1 = \gamma^2 k_0'/\eta$ and $\kappa_2 = \gamma^3 k_0''/\eta$ respectively. Substituting Eqs. [(2.16a), (2.16b)] in (2.20) gives:

$$\kappa_1 = \frac{\gamma^2|\Omega_c|^2 - (\gamma\gamma_{23} + |\Omega_p|^2)^2}{(\gamma\gamma_{23} + |\Omega_c|^2 + |\Omega_p|^2)^2}, \tag{2.21a}$$

$$\kappa_2 = 2i\{\gamma^2|\Omega_c|^2\left[\gamma(2\gamma_{23} + \gamma) + 2|\Omega_p|^2\right] - (\gamma\gamma_{23} + |\Omega_p|^2)^3\}/(\gamma\gamma_{23} + |\Omega_c|^2 + |\Omega_p|^2)^3. \tag{2.21b}$$

For the parameters mentioned in Fig. 2.2, (2.21a) gives $\kappa_1 = 0.0625$, which is close to the numerically obtained value, 0.0623. The theoretical value of $\kappa_2 = 7.83 \times 10^{-3}i$,

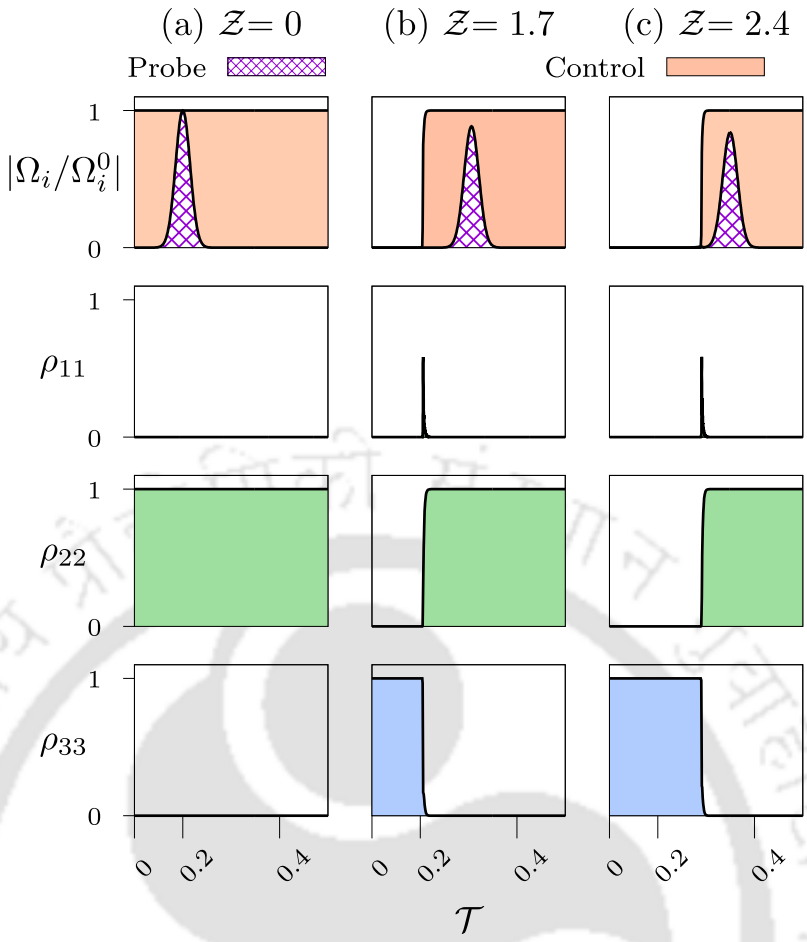

Figure 2.5: 1st row: Probe ($i = p$, crisscross) and control ($i = c$, solid) field magnitude vs time, $\mathcal{T}$ are plotted column wise for $\mathcal{Z} = 0$, 1.7, and 2.4 in (a), (b), (c) respectively. Other rows: Population distributions at the corresponding propagation lengths. The probe is shown traveling inside a medium with population distribution $\rho_{11} = \rho_{33} = 0$ and $\rho_{22} = 1$. Normalization of field magnitudes and parameters used are same as Fig. 2.2. Figures belonging to a particular row and column have a common vertical and horizontal axes, respectively.

for the parameters mentioned in Fig. 2.2, is very small to cause any significant change in the pulse width $\sigma(z) = \sqrt{\sigma_0^2 - ik_0''z}$. This is why in Fig. 2.5 (1st row), from $0 \leq \mathcal{Z} \leq 2.4$ no noticeable change in the pulse width is observed.

The parameter κ_1 can be perceived as the rate at which the probe pulse proceeds along time axis, $\mathcal{T}$ with increasing $\mathcal{Z}$. For the parameters mentioned in Fig. 2.2, the aforementioned value of $\kappa_1 = 0.0625$, obtained using (2.21a), is less than $\beta = 0.125$ (see Table 2.1). Therefore, the control field's leading end moves forward along time axis at a greater rate than the probe pulse as evident from Fig. 2.5 (1st row).

In Fig. 2.5 (3rd column), beyond $\mathcal{Z} \geq 2.4$, control field's leading end begins to overlap with the probe pulse, thereby initiating the process of pulse reshaping and amplification, which continues till the control field's leading end completely overtakes the probe pulse at $\mathcal{Z} = 4.2$. The process of probe amplification is explained in the next section.

2.3.3 Probe reshaping and amplification

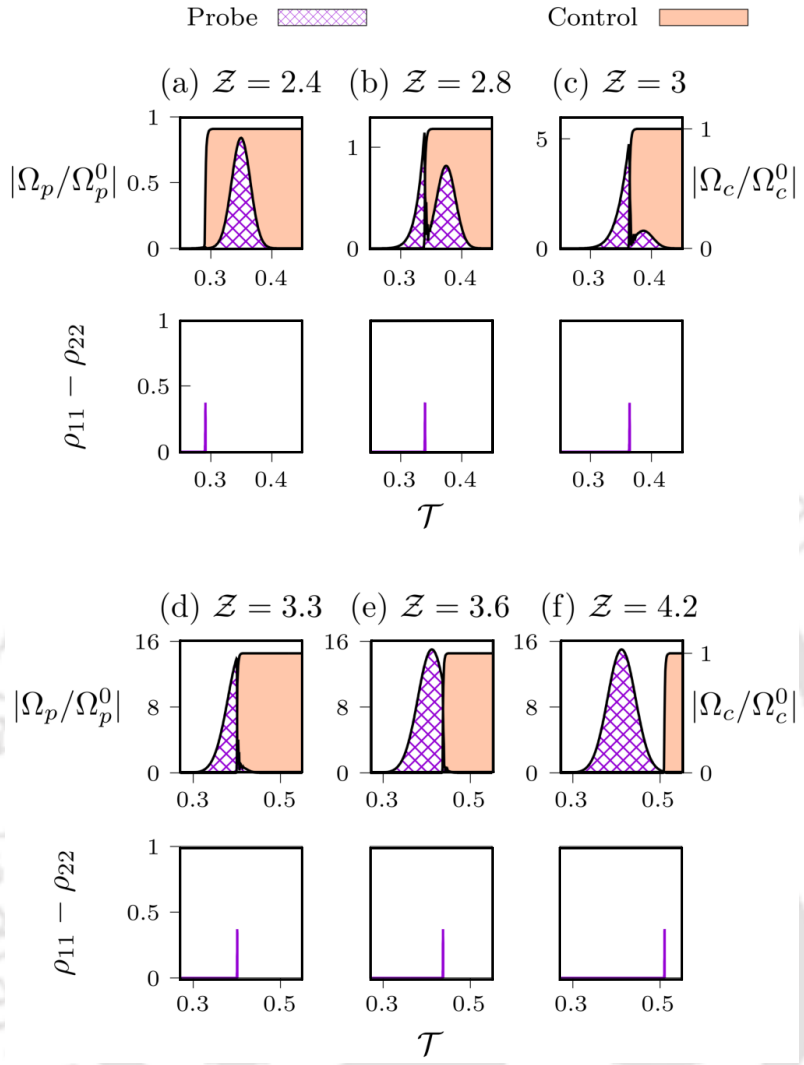

Figure 2.6: 1st row of figures, (a) - (f): Temporal profiles of probe (crisscross) and control (solid) field magnitude are plotted column wise at different propagation length, $\mathcal{Z}$. 2nd row of figures, (a) - (f): $(\rho_{11} - \rho_{22})$ vs time $\mathcal{T}$, at the corresponding propagation lengths. The plot illustrates how the positive peak of $(\rho_{11} - \rho_{22})$ at the position of control field's leading end causes probe amplification at every (ζ, τ). Normalization of field magnitude and the parameters used are same as Fig. 2.2. In the top row of all Figs. 2.6(a) - 2.6(f), the left and right vertical axes denote normalized probe and control field magnitudes respectively. Plots belonging to a particular column have a common time axis. The tics on the vertical axis for $(\rho_{11} - \rho_{22})$ vs $\mathcal{T}$, and $|\Omega_c/\Omega_c^0|$ vs $\mathcal{T}$ plots remain same along a row. However, the plots for $|\Omega_p/\Omega_p^0|$ vs $\mathcal{T}$ have different tics on the vertical axis along a row due to amplification of probe pulse with increasing propagation length, $\mathcal{Z}$.

As seen earlier in Fig. 2.3 (2nd row), there occurs a momentary population transfer from the ground state $|3\rangle$ to excited state $|1\rangle$ at the position of control field's leading end on time axis. This leads to a positive peak in $(\rho_{11} - \rho_{22})$, indicating population inversion in the $|1\rangle \leftrightarrow |2\rangle$ channel at the position of control field's leading end on

time axis [see 2nd row of Figs. 2.6(a) - 2.6(f)]. Hence, in presence of the probe field there is stimulated emission of probe photons in the $|1\rangle \leftrightarrow |2\rangle$ channel causing probe amplification. This is illustrated in Fig. 2.6, where the temporal profiles of probe and control field magnitudes along with $(\rho_{11} - \rho_{22})$ are plotted column wise at different propagation lengths. In Fig. 2.6, with increasing $\mathcal{Z}$, both the positive peak of $(\rho_{11} - \rho_{22})$ and control field's leading end, proceed collinearly at a greater rate than the probe pulse along time axis. At $\mathcal{Z} = 2.4$, the leading end of both probe and control fields, the peak of peak of $(\rho_{11} - \rho_{22})$, all coincide on the time axis. From $2.4 \leq \mathcal{Z} \leq 4.2$, the control field's leading end or in other words, the positive peak of $(\rho_{11} - \rho_{22})$ grazes through the probe pulse on time axis. This causes probe amplification due to stimulated emission, at the position of the positive peak of $(\rho_{11} - \rho_{22})$ on time axis for every space time coordinate from ($\mathcal{T} = 0.3$ to 0.5, $\mathcal{Z} = 2.4$ to 4.2), respectively. In Fig. 2.6(f), beyond $\mathcal{Z} \geq 4.2$, both the positive peak of $(\rho_{11} - \rho_{22})$ and the control field's leading end completely overtakes the probe pulse, halting further amplification. Our model system is phase-insensitive between probe and control fields due to on open loop Λ-system[41]. The probe pulse then travels at the speed of light in vacuum, without any delay, distortion, and absorption, whilst retaining its initial Gaussian shape but with a larger pulse width. This stable propagation of the probe pulse is explained in the next section.

2.3.4 Stable probe propagation

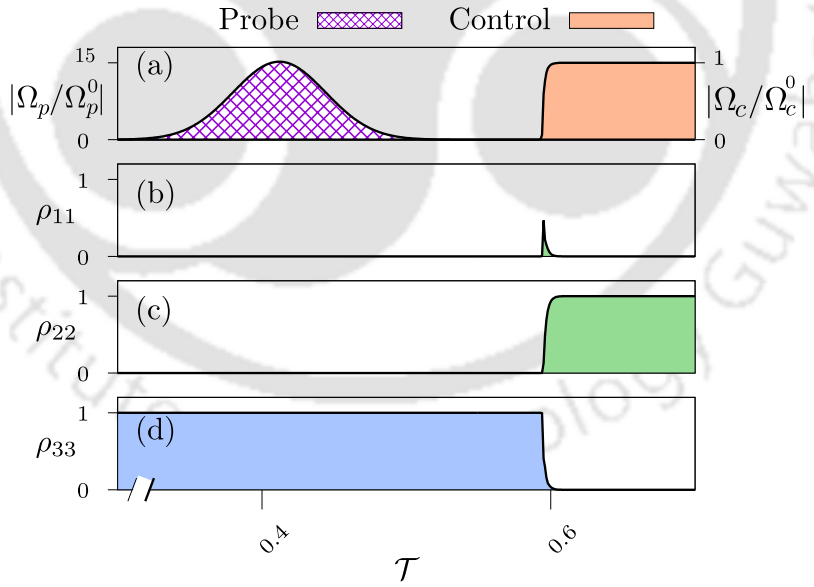

Figure 2.7: (a) Temporal profiles of probe (crisscross) and control (solid) field magnitudes at $\mathcal{Z} = 4.9$. (b), (c), (d) Population distribution of $|1\rangle$, $|2\rangle$ and $|3\rangle$ respectively. The plot illustrates the population distribution, $\rho_{11} = \rho_{22} = 0, \rho_{33} = 1$ as seen by the probe after the control field's leading end completely overtakes it. Normalization of field magnitudes, and parameters used are same as Fig. 2.2. In figure (a), the left and right vertical axes denote normalized probe and control field magnitudes respectively. All figures have a common time axis, $\mathcal{T}$.

The technique of pulse amplification at hand, ensures a stable pulse propagation upon completion of amplification. This is made possible due to the population distributions created by the control field as it propagates through the medium. Figure 2.7 shows the temporal profiles of the fields along with population distribution at a position $\mathcal{Z} = 4.9$ after the completion of amplification process. In Fig. 2.7, within $0 \leq \mathcal{T} \leq 0.6$, the probe pulse sees a population distribution $\rho_{11} = \rho_{22} = 0, \rho_{33} = 1$ [see Figs. 2.7(b) - 2.7(d)], *i.e.*, all population gets settled in the dark state $|3\rangle$ [15]. Therefore, the general state $|\psi\rangle$ of the system within the time interval $0 \leq \mathcal{T} \leq 0.6$ can be written as:

$$|\psi\rangle = a_1|1\rangle + a_2|2\rangle + a_3|3\rangle = |3\rangle, \tag{2.22}$$

where a_i $(i = 1, 2, 3)$ represent the probability amplitudes of state $|i\rangle$. Equation (2.22) implies $a_1 = a_2 = 0, a_3 = 1$. Therefore, from the definition of density matrix elements $\rho_{12} = a_1^* a_2 = 0$. The propagation equation for the probe pulse [see (2.11a)] then becomes:

$$\frac{\partial \Omega_p(\zeta, \tau)}{\partial \zeta} = i\eta\rho_{12}(\zeta, \tau) = 0, \tag{2.23}$$

which resembles a free space propagation equation. Thus at the end of amplification process, the probe pulse travels freely, unattenuated and undistorted at the speed of light in vacuum, even in the presence of medium.

2.3.5 Probe pulse broadening

Apart from the negligible pulse broadening due to dispersion in the region $0 \leq \mathcal{Z} \leq 2.4$ [Fig. 2.5 (1^{st} row)], the probe pulse is subjected to a noticeable pulse broadening during amplification within $2.4 \leq \mathcal{Z} \leq 3.9$ [1^{st} row of Figs. 2.6(a) - 2.6(c)]. This section provides a qualitative explanation for such a pulse broadening. Figure 2.8, shows the temporal profiles of the fields along with population distribution at a position amidst the amplification process. During the amplification process, the probe pulse sort of splits into two portions as indicated by the crisscross and oblique line patterns in Fig. 2.8(a). The crisscross pattern indicates the amplified portion of probe and the oblique line pattern represents the portion of probe which is yet to be amplified. In Figs. 2.8(b) - 2.8(d), the oblique line portion sees a population distribution $\rho_{11} = \rho_{33} = 0, \rho_{22} = 1$, and the crisscross portion sees a different population distribution $\rho_{11} = \rho_{22} = 0, \rho_{33} = 1$. The former serves as an absorbing, dispersive medium, while the later behaves like dark state, as discussed earlier in Sec. 2.3.2 and 2.3.4, respectively. Therefore, the crisscross portion propagates freely without experiencing any delay, distortion and absorption. But the oblique line portion continues to experience noticeable delay, with small absorption and insignificant broadening due to dispersion. It's due to this delay, experienced by the oblique line portion, the probe pulse gets elongated while the control field grazes through it along time axis, with increasing propagation length. The small absorption experienced by the oblique line portion is compensated by amplification and doesn't lead to any noticeable shape distortion.

2.3.6 Evaluation of probe pulse width

To check the predictability of the system, a formula for the probe pulse width at the end of amplification process is derived in terms of experimentally available

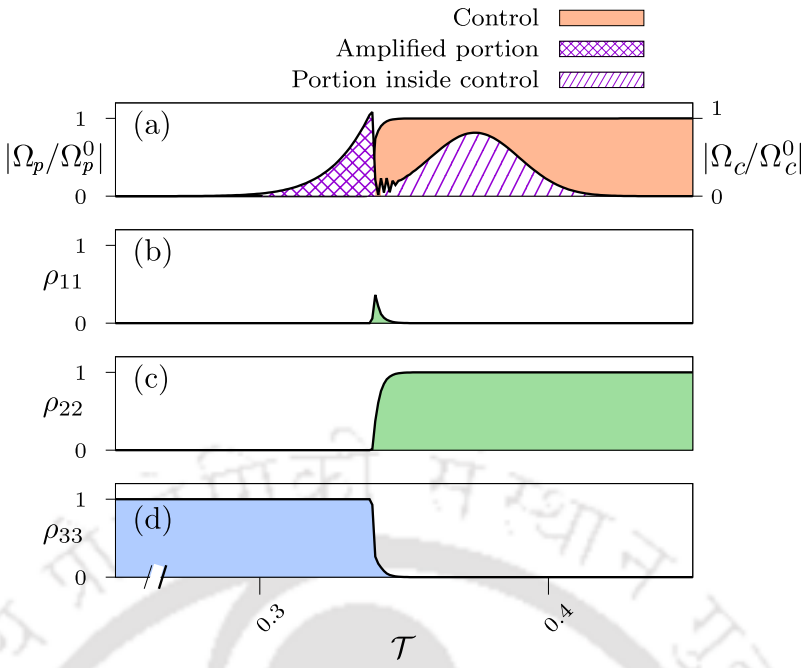

Figure 2.8: (a) Temporal profiles of probe (crisscross and oblique line patterns) and control (solid) field magnitudes at $\mathcal{Z} = 2.8$. (b), (c), (d) Population distribution of $|1\rangle$, $|2\rangle$ and $|3\rangle$ respectively. The plot shows how the portion of the probe pulse behind the control field's leading end [crisscross pattern in (a)] sees a population distribution $\rho_{11} = \rho_{22} = 0$, $\rho_{33} = 1$. Whereas, the portion of probe pulse inside the control field [oblique line pattern in (a)] sees a different population distribution $\rho_{11} = \rho_{33} = 0$, $\rho_{22} = 1$. The former behaves like dark state, while the later serves as a bright state. Hence the oblique line portion continues to experience delay, absorption and dispersion, while the crisscross portion undergoes free space propagation. Normalization of field magnitudes, and parameters used are same as Fig. 2.2. In figure (a), the left and right vertical axes denote normalized probe and control field magnitudes respectively. All figures have a common time axis, $\mathcal{T}$.

parameters. To simplify the derivation, an analogy to a simple classical problem is drawn in Fig. 2.9.

In Fig. 2.9(a), the bars indicated by "A" and "B" move forward along x axis at rates v_1 and v_2 respectively ($v_2 > v_1$). The bars "A" and "B" coincide in an elapsed time, "t" after traveling a distance $A'A$ and $B'B$ respectively [Fig. 2.9(b)]. Analogously, in Fig. 2.9(c), the trailing end of probe pulse and the control field's leading end move forward along the dimensionless time axis ($\mathcal{T}$) at rates κ_1 and β ($\beta > \kappa_1$) respectively, with increasing dimensionless propagation length $\mathcal{Z}$. Thus, we can represent the control field's leading end by the bar "A" and, the trailing end of probe pulse by the bar "B". As discussed in section 2.3.2, the control field's leading end moves forward along time axis with increasing propagation length at a higher rate compared to the probe pulse, *i.e.*, $\beta > \kappa_1$. Therefore, at a particular propagation distance, the leading end of both control field and the probe pulse would touch each other as shown in Fig. 2.9(c), where, $\mathcal{Z}_c$ denotes the propagation length at which both the leading end of probe and control coincide on time axis. In Fig. 2.9(d), after propagating a distance say, $\mathcal{Z}'$, the control field's leading end completely

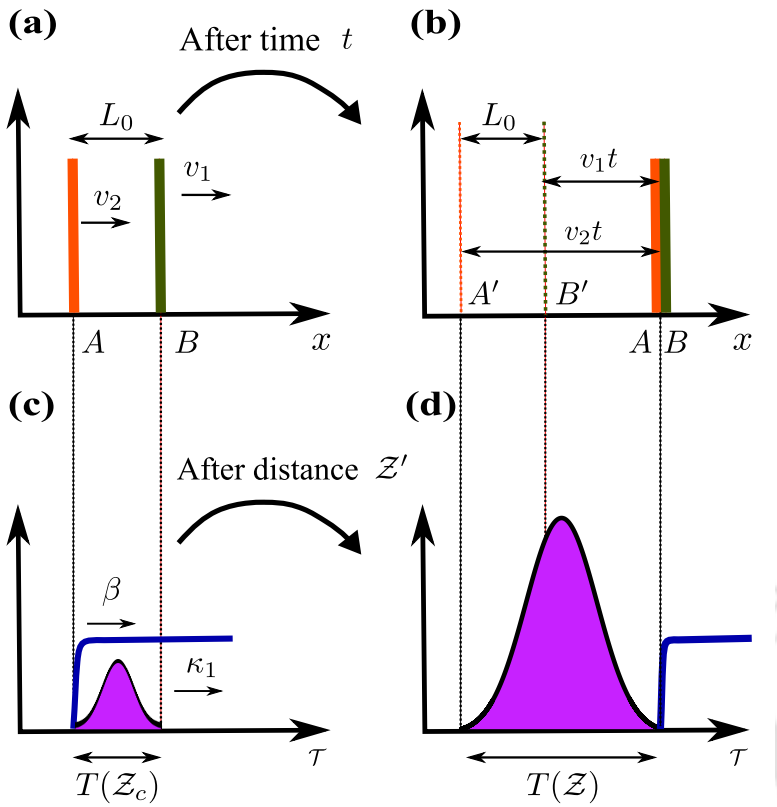

Figure 2.9: A diagram illustrating an analogy of the problem to a similar classical problem.

overtakes the probe, leaving behind a broadened, amplified Gaussian probe pulse. From observation, the full extent of the probe pulse, $T(\mathcal{Z})$ [Fig. 2.9(d)], after the amplification process, is simply the time taken by control field's leading end to overtake the trailing end of probe pulse on time axis.

From Fig. 2.9(b), with simple manipulation $A'A$ can be written as:

$$A'A = \frac{v_2 L_0}{(v_2 - v_1)}. \tag{2.24}$$

Since, figures 2.9(a) and 2.9(b) are analogous to figures 2.9(c) and 2.9(d) respectively, the following quantities can be considered equivalent to each other:

$$A'A \equiv T(\mathcal{Z}), \quad v_2 \equiv \beta, \quad v_1 \equiv \kappa_1, \quad L_0 \equiv T(\mathcal{Z}_c). \tag{2.25}$$

Substituting (2.25) in (2.24) gives

$$T(\mathcal{Z}) = \frac{\beta T(\mathcal{Z}_c)}{(\beta - \kappa_1)}. \tag{2.26}$$

With some simple algebra, $\mathcal{Z}_c$ can be written as:

$$\mathcal{Z}_c = \frac{-B - \sqrt{B^2 - 4C}}{2}, \tag{2.27}$$
$$B = -\frac{8(\beta - \kappa_1)\gamma\tau_0 + \kappa_2 a}{4(\beta - \kappa_1)^2} \quad \left[a = 2\sqrt{2\ln(10^3)}\right],$$

$$C = \frac{4\gamma^2\tau_0^2 - \gamma^2\sigma_0^2 a^2}{4(\beta - \kappa_1)^2}.$$

The dimensionless pulse width, $\sigma(\mathcal{Z})$ can be calculated by using the relation (see appendix A of this thesis):

$$T(\mathcal{Z}) = 2\sqrt{2\ln(10^3)}\sigma(\mathcal{Z}), \tag{2.28}$$

where, dimensionless pulse width, $\sigma(\mathcal{Z})^2 = (\sigma_0\gamma)^2 - i\kappa_2\mathcal{Z}$. Substituting the earlier obtained values of $\kappa_1 = 0.06233$, $\kappa_2 = 7.83 \times 10^{-3}$ (see Sec. 2.3.2) and $\beta = 0.123$ (see Table 2.1) in Eqs. [(2.26) - (2.28)] gives $T(\mathcal{Z}) = 0.235099$, which is close to the numerically obtained value, 0.237545.

As seen in Eqs. [(2.15), (2.21a), (2.21b)] the value of β and κ_1, κ_2 (for $\Omega_p^0 \ll \Omega_c^0$) are merely dependent on $|\Omega_c|$ and independent of the initial pulse width σ_0, which makes $T(\mathcal{Z})$ [(2.26)] independent of σ_0. Therefore, for a particular control field intensity, the ratio $T(\mathcal{Z})/T(0)$ is expected to remain constant for any arbitrary σ_0.

Table 2.2: Table shows the ratio of $T(\mathcal{Z})$, to the initial full extent of probe pulse $T(0)$.

$\sigma_0\gamma$	Ω_p^0/γ	$T(8.9)^*$	$T(0)^*$	$T(8.9)/T(0)$
15	10	237.545	111.51	2.13
30	7.071	463.522	223.02	2.078
45	5.774	693.604	334.53	2.073
60	5	919.856	446.04	2.062

*In the normalized, dimensionless time axis $\mathcal{T}$, these columns have a multiplicative factor of 10^{-3} (see definition of $\mathcal{T}$ in 1st para. of sec. 2.3).

Keeping $\Omega_c^0 = 4\gamma$ and area of probe pulse constant, the ratios $T(\mathcal{Z})/T(0)$, obtained numerically for different values of σ_0 are tabulated in Table 2.2. In Table 2.2, the ratio $T(\mathcal{Z})/T(0) \approx 2$, *i.e.*, it remains constant for different initial probe pulse width σ_0, which matches the expected result. Therefore, the formula in (2.26) correctly estimates the probe pulse width at the end of amplification process, countenancing the correctness of the numerical simulation.

2.3.7 Ancillary results

The propagation of a sech^2, square and a complex shaped pulse, are investigated indiscriminately in presence of a continuous control field. The complex shaped pulse and sech^2 pulse are given as:

$$\Omega_p(0,t) = \Omega_p^0\left(e^{-(\tau-\tau_1)^2/\sigma_1^2} + \text{sech}[-(t-\tau_2)/\sigma_2]\right),$$
$$\Omega_p(0,t) = \Omega_p^0\text{sech}^2[-(\tau-\tau_3)/\sigma_3].$$

In presence of a continuous control field, both the complex and sech^2 pulses show similar amplification and elongation (Fig. 2.10) as obtained earlier with a Gaussian pulse. The control field also shows similar absorption as before. The square pulse shows similar elongation but doesn't retain it's square shape at end of amplification process. Therefore, our method can be used to amplify arbitrary pulse shapes without loss of generality.

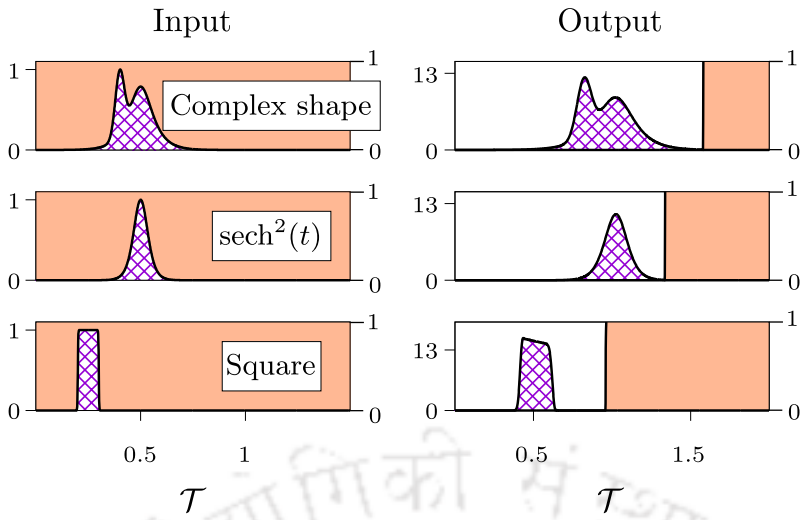

Figure 2.10: Left column: Temporal profiles of probe (crisscross) and control (solid) field magnitude at $\mathcal{Z} = 0$, for different probe pulse shapes. Right column: Corresponding temporal profiles of probe and control field magnitudes at the end of amplification process. Field magnitude normalization, and parameters used are same as Fig. 2.2, with the additional parameters: $\sigma_1 = 30/\gamma$, $\sigma_2 = 40/\gamma$, $\sigma_3 = 45/\gamma$, $\tau_1 = 400/\gamma$, $\tau_2 = 500/\gamma$, $\tau_3 = 500/\gamma$. The left and right vertical axes of each plot correspond to normalized probe and control field magnitude respectively. Figures belonging to a particular column have a common time axis.

Next, the propagation of a Gaussian pulse in presence of a continuous control field is investigated for different control magnitudes. As explained earlier in Fig. 2.8, the amplified portion of the probe (crisscross), being uninfluenced by the control, isn't subject to pulse broadening due to dispersion, but the portion of probe under the influence of control (oblique line pattern) continues to experience broadening. Therefore, if κ_2, which is responsible for pulse broadening, is large, then the oblique line portion of probe will experience significant broadening, resulting in an asymmetric pulse shape posterior to the amplification process. This is shown in Fig. 2.11(a), where $\kappa_2 = 31.651i$ for $\Omega_c^0/\gamma = 0.5$, results in an asymmetric output pulse shape. Whereas, the output pulse shape for $\kappa_2 = 4.89 \times 10^{-3}i$ corresponding to $\Omega_c^0/\gamma = 4.5$ in Fig. 2.11(d), shows closer semblance to the input Gaussian shape. The parameter κ_2 decreases with increase in Ω_c^0. Therefore, from Fig. 2.11(a) - (d), as Ω_c^0/γ is increased from 0.5 to 4.5, the output pulse shape becomes more close to the input Gaussian shape.

In Fig. 2.11(a) - (e), as Ω_c^0/γ is increased from 0.5 to 5, the amplification also increases. Raising Ω_c^0, beyond a certain value, *e.g.*, $\Omega_c^0 = 5\gamma$ in Fig. 2.11(e), results in an unstable output probe pulse. The explanation for this is given in the appendix A of this thesis.

Therefore, choice of input control field intensity plays a crucial role in deciding the amount of amplification and the shape of probe pulse at the end of amplification process. A relatively small value of Ω_c^0 leads to small amplification and asymmetries in the output pulse shape. Again, a large value of Ω_c^0 results in instabilities caused by huge gain. The sweet spot lies somewhere in the middle as seen in Fig. 2.11.

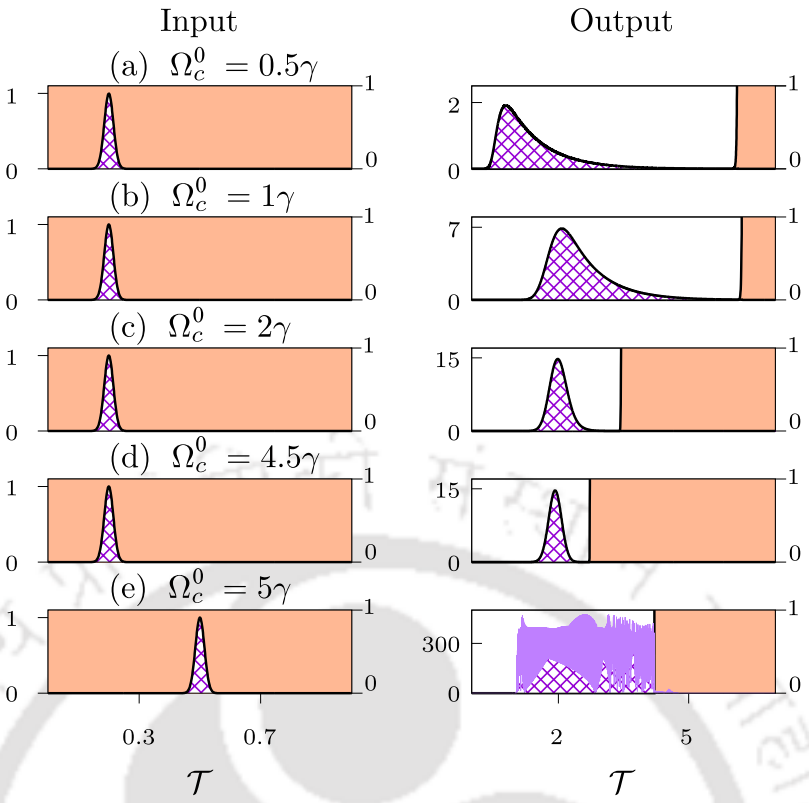

Figure 2.11: Left column: Temporal profiles of probe (crisscross) and control (solid) field magnitudes at $\mathcal{Z} = 0$, for different values of Ω_c^0/γ. Right column: Corresponding temporal profiles of probe and control field magnitudes at the end of amplification process. Field magnitude normalization and relevant parameters remain same as Fig. 2.2. The left and right vertical axes of each plot correspond to normalized probe and control field magnitude respectively. Figures belonging to a particular column have a common time axis.

2.4 Conclusion

In conclusion, the propagation of a weak probe pulse through the Λ system in a resonant gain configuration is investigated. The gain configuration is different from the EIT system in a way that the control and probe fields are swapped with one another. This configuration makes provision for population inversion in the transition coupled by the probe field. Thus, causing probe amplification through stimulated emission. This broadening can be easily compensated using compressors. With a careful choice of control field intensity, the probe pulse although broadened, retains its initial shape and travels at the speed of light in vacuum, without any delay, absorption and dispersion after the amplification process. With this scheme, an arbitrary shaped probe pulse can propagate through the medium without loss of generality at the end of amplification. This mechanism is also applicable to an inhomogeneously broadened atomic system. Therefore, the proposed model system could be useful in optical communication as one of the methods to amplify various signals, for possibly assisting long distance communication.

Chapter 3

Pulse amplification in a closed loop Λ system with permanent dipole moment

3.1 Introduction

All experimental and theoretical studies associated with EIT have been mostly done with atomic energy levels. In the past couple of years, there have been studies based on polar molecules. The presence of permanent dipole moments (PDM) in polar molecules gives rise to new phenomena which are significantly different from the ones in absence of PDM. For e.g., Kmetic *et al.* [98] showed that in a two-level system with a nonzero difference in the PDMs of its levels, enables two-photon transition which is forbidden by parity selection rules in the atomic counterpart. In the case of two fields interacting with a two-level system with unequal PDMs of the levels, Band *et al.* [99] show that Raman scattering, two-photon absorption, and wave mixing of arbitrary order are achievable. The essential difference between the presence and absence of PDM is briefly discussed in the following paragraph.

Molecules can be classified mainly into centrosymmetric and noncentrosymmetric. Centrosymmetric molecules have a spatial inversion center while noncentrosymmetric molecules (e.g. all polar molecules) don't. Due to which, the energy eigenfunctions, ψs for centrosymmetric molecules are parity eigenstates, meaning they are either even or odd functions. Whereas wave functions for noncentrosymmetric molecules are neither even nor odd. Thus, the diagonal elements of the dipole moment matrix, $\mu_{jj} \propto \int_{-\infty}^{\infty} \psi_j \vec{r} \psi_j dr$, are zero for centrosymmetric molecules and non zero for non centrosymmetric molecules. These diagonal matrix elements represent the permanent dipole moments as indicated in Fig. 3.1. Also in the case of centrosymmetric molecules $\mu_{jk} \neq 0$ only if ψ_j and ψ_k are of different parity i.e., if one of them is odd then the other must be even and vice versa, therefore a two-photon transition between $|\psi\rangle_j \rightarrow |\psi\rangle_k$ is possible via an intermediate state $|\psi\rangle_i$ provided $|\psi\rangle_j$ and $|\psi\rangle_k$ have the same parity, in which case they are single-photon forbidden. Therefore, for centrosymmetric molecules, the single-photon allowed transitions are not two-photon allowed and vice versa. But in the case of noncentrosymmetric molecules, due to broken spatial symmetry, ψ's are neither odd nor even therefore both single and two-photon excitation is possible for the same transition. In addition to multi-photon excitation, the breaking of spatial symmetry due to presence

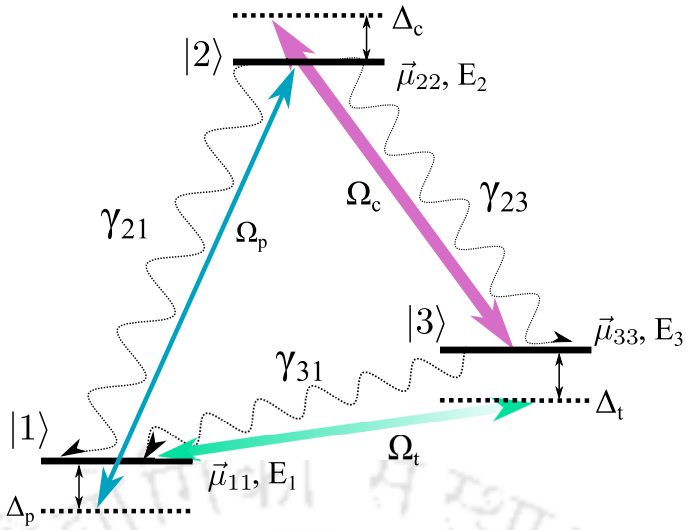

Figure 3.1: Schematic diagram of a closed loop three level Λ-system with PDMs. Here, $|2\rangle$ is the excited state, $|3\rangle$ is an intermediate meta stable state and $|1\rangle$ the ground state, with energy set to zero. The molecular transitions, $|1\rangle \leftrightarrow |2\rangle$, $|3\rangle \leftrightarrow |2\rangle$, and $|1\rangle \leftrightarrow |3\rangle$ are coupled by a weak probe field, $\vec{E}_p$ with frequency, ω_p, a strong control field, $\vec{E}_c$ with frequency, ω_c, and a third field, $\vec{E}_t$ with frequency, ω_t, respectively. The population decay rate from state, $|i\rangle$ to $|j\rangle$ is denoted by γ_{ij}. The detunings, and Rabi frequencies of the fields are denoted by Δ_i, and Ω_i respectively ($i = p, c, t$ represents probe, control, and the third field, respectively). The energies of $|i\rangle$ ($i = 1, 2, 3$) are denoted by E_i and the PDMs are denoted by μ_{ii}.

of PDM leads to higher harmonic generation in two-level system [100], having application in attosecond pulse generation [101], and enhancement of many well known nonlinear effects [102].

So far, there has been studies on the effects of PDMs on EIT [103, 104, 105], STIRAP [106, 107], pulse propagation [108], molecule cavity quantum electrodynamics [109], Goos–Hänchen shift manipulation [110], higher harmonic generation [100], population inversion [111] and optical bistability [112]. In this work, we study the propagation of a weak probe pulse through a closed loop three level Λ system with PDMs in presence of a strong control field and a third field.

3.2 Theory

To study the effect of PDMs on pulse propagation, we consider a closed loop three level Λ system with PDMs as given in Fig. 3.1. In Fig. 3.1, the molecular transitions $|1\rangle \leftrightarrow |2\rangle$, $|3\rangle \leftrightarrow |2\rangle$, and $|1\rangle \leftrightarrow |3\rangle$ are coupled by a weak probe field, $\vec{E}_p$ with frequency, ω_p, a strong control field, $\vec{E}_c$, with frequency, ω_c, and a third field, $\vec{E}_t$ with frequency, ω_t, respectively. The electric fields are considered to be propagating along z direction and are defined considering a plane wave approximation as:

$$\vec{E} = \sum_{j=p,c,t} \hat{e}_j \mathcal{E}_j f_j(t) \cos(\omega_j t) \tag{3.1}$$

where $\hat{e}_j$ are the unit polarization vectors, $\mathcal{E}_j$ are the field amplitudes, $f_j(t)$ are the slowly varying envelope functions, and ω_j are the field carrier frequencies of the fields. The index $j = p, c, t$ represents probe, control, and the third field, respectively. Let $|\psi(t)\rangle = \sum_i^3 a_j(t)|j\rangle$ be a general state for the Λ system in Fig. 3.1 such that the Schrödinger equation for the Λ system, in terms of the probability amplitudes a_j, can be written as:

$$i\frac{\partial \mathbf{a}(t)}{\partial t} = \hbar^{-1}\left[\mathbf{E} - \boldsymbol{\mu}.\vec{E}(t)\right]\mathbf{a}(t), \tag{3.2}$$

where, $(\mathbf{a}(t))_j = a_j(t)$, $(\mathbf{E})_{jk} = E_j\delta_{jk}$, and $(\boldsymbol{\mu})_{jk} = \vec{\mu}_{jk} = \langle j|\boldsymbol{\mu}|k\rangle$. To write the Hamiltonian in a time independent form, the following transformation [103, 104, 113] is used:

$$\mathbf{a(t)} = \mathbf{T}\mathbf{b}(t), \tag{3.3}$$

where

$$T_{jk} = \delta_{jk}\exp[-i\frac{E_j}{\hbar}(t - t_0)]\exp[i\beta_{jk}], \tag{3.4}$$

and

$$\beta_{jk} = \frac{\vec{\mu}_{jk}}{\hbar}.\int_0^t \vec{E}(t')dt', \tag{3.5}$$

Using Eqs. [(3.4), (3.5)] and substituting Eq. (3.3) into Eq. (3.2) gives:

$$i\frac{\partial \mathbf{b}(t)}{\partial t} = \mathbf{H}^b(t)\mathbf{b}(t), \tag{3.6}$$

with

$$\mathbf{H}^b_{jk}(t) = -\frac{\vec{\mu}_{jk}.\vec{E}(t)}{\hbar}\exp[-\frac{iE_{kj}}{\hbar}t]\exp[i(\beta_{kk} - \beta_{jj})], \tag{3.7}$$

where, $\mathbf{H}^b_{jk}(t) = 0$, $(\forall\ j = k)$ and $E_{k,j} = E_k - E_j$. Putting (3.5) in (3.7), expanding the cosine functions in terms of exponentials, and using $\exp(iz\sin x) = \sum_{n=-\infty}^{\infty} J_n(z)\exp(inx)$ [$J_n(z)$ is the first kind Bessel function of integer order n], gives:

$$\begin{aligned}\mathbf{H}^b_{jk}(t) = -\sum_{n_i=-\infty}^{\infty}\left(\sum_i \frac{n_i\vec{\mu}_{jk}.\hat{e}_i\mathcal{E}_i}{\hbar z^i_{kj}}\right)\prod_i J_{n_i}\left(z^i_{kj}f_i(t)\right) \\ \times\exp\left[-i\left(\frac{E_{kj}}{\hbar} - \sum_{n_i} n_i\omega_i\right)t\right], \quad (i = p, c, t)\end{aligned} \tag{3.8}$$

Now applying RWA (Rotating wave approximation), the far-off-resonant terms in the exponentials are neglected. It is also assumed that the probe transition involves the absorption of n_p probe photons, zero photons of control and the third field. The same rule applies to the transitions corresponding to control and the third field. Finally, the Hamiltonian for the system becomes:

$$\mathbf{H}^b(t) = -\left(\tilde{\Omega}_p e^{i\Delta_p t}|1\rangle\langle 2| + \tilde{\Omega}_t e^{i\Delta_t t}|1\rangle\langle 3| + \tilde{\Omega}^*_c e^{-i\Delta_c t}|2\rangle\langle 3|\right) + \text{h.c.}, \tag{3.9}$$

where, $\Delta_p = n_p w_p - E_{21}/\hbar$, $\Delta_c = n_c w_c - E_{23}/\hbar$, and $\Delta_t = n_t w_t - E_{31}/\hbar$ are the respective field detunings, and $\tilde{\Omega}_i$ $(i = p, c, t)$ are the effective Rabi frequencies of probe (p), control (c) and the third (t) field, respectively, in presence of PDMs. The modified Rabi frequencies of the three fields can be expressed as:

$$\tilde{\Omega}_p = \frac{n_p \Omega_p J_{n_p}(z_{21}^p f_p(t)) J_0(z_{21}^c f_c(t)) J_0(z_{21}^t f_t(t))}{z_{21}^p}, \tag{3.10a}$$

$$\tilde{\Omega}_c = \frac{n_c \Omega_c J_0(z_{23}^p f_p(t)) J_{n_c}(z_{23}^c f_c(t)) J_0(z_{23}^t f_t(t))}{z_{23}^c}, \tag{3.10b}$$

$$\tilde{\Omega}_t = \frac{n_t \Omega_t J_0(z_{31}^p f_p(t)) J_0(z_{31}^c f_c(t)) J_{n_t}(z_{31}^t f_t(t))}{z_{31}^t}, \tag{3.10c}$$

with

$$\Omega_p = \frac{\vec{\mu}_{12}.\hat{e}_p \mathcal{E}_p}{\hbar},\ \Omega_c = \frac{\vec{\mu}_{32}.\hat{e}_c \mathcal{E}_c}{\hbar},\ \Omega_t = \frac{\vec{\mu}_{13}.\hat{e}_t \mathcal{E}_t}{\hbar},\ \text{and}\ z_{jk}^{\alpha} = \frac{\vec{d}_{jk}.\hat{e}_\alpha \mathcal{E}_\alpha}{\hbar w_\alpha}\ (\alpha = p, c, t). \tag{3.11}$$

In Eq. (3.11), $\vec{d}_{jk} = \vec{\mu}_{jj} - \vec{\mu}_{kk}$ $(j, k = 1, 2, 3)$. In Eqns. (3.10a), (3.10b), and (3.10c) the indices n_p, n_c, n_t determines whether the probe, control, and the third field transitions, respectively are one or multiphoton transitions. For example, $n_p = n_c = n_t = 1$ refers to all three transitions being one photon transitions. While, $n_p = n_c = n_t = 2$, would mean, all three transitions are two photon transitions. From experimental perspective, "two photon excitation" of all three transition simply means detuning the three lasers as: $\Delta_p = \omega_{21}/2$, $\Delta_c = \omega_{23}/2$, and $\Delta_t = \omega_{31}/2$, respectively. Here, ω_{ji} represents the transition frequency of $|i\rangle \leftrightarrow |j\rangle$ transition. Similarly, a "three-photon" excitation of any transition refers to the carrier frequencies of the corresponding coupling laser being $1/3^{\text{rd}}$ of the transition frequency, so on and so forth. The molecular level system given in Fig. 3.1, can be realized using the vibrational energy levels of HCN. The energies and PDMs of relevant HCN vibrational energy levels are listed in table 3.1.

$\|i\rangle$	ν_1, ν_2, l, ν_3	E_i (a.u)	μ_{ii} (a.u)
$\|1\rangle$	$0, 0, 0, 0$	0	1.17061
$\|2\rangle$	$3, 1, 1, 0$	0.047038	1.181391
$\|3\rangle$	$0, 1, 1, 0$	0.003269	1.151803

Table 3.1: HCN→HNC isomerization data.

The transition dipole moments in atomic units (a.u) are: $\mu_{12} = 1.25906 \times 10^{-5}$, $\mu_{13} = 0.074363184$, $\mu_{32} = 3.93 \times 10^{-5}$. The above paramenters and data given in table 3.1 are taken from HCN→HNC isomerization data [114, 115].

3.2.1 Density matrix equations

The dynamics of molecular energy state population and molecular coherences are governed by the following Liouville equation:

$$\frac{\partial \rho}{\partial t} = -i\hbar[\boldsymbol{H}^b(t), \rho] + \mathcal{L}_\rho. \tag{3.12}$$

The Liouville operator $\mathcal{L}_\rho$, describes all incoherent processes and can be expressed as:

$$\mathcal{L}_\rho = -\sum_{i=2}^{3}\sum_{\substack{j=1,\\ j\neq i}}^{3} \frac{\gamma_{ij}}{2}\left(|i\rangle\langle i|\rho - 2|j\rangle\langle j|\rho_{ii} + \rho|i\rangle\langle i|\right), \tag{3.13}$$

To get rid of the exponential factors in Eq. (3.9), the following transformations are used: $\rho_{12} = \rho_{12}e^{i\Delta_p t}, \rho_{23} = \rho_{23}e^{-i\Delta_c t}, \rho_{13} = \rho_{13}e^{i\Delta_t t}$; and $\rho_{jj} = \rho_{jj}$ $(j = 1, 2, 3)$. The equations of motion for the molecular state populations and coherences of the three level Λ-system are then given as:

$$\dot{\rho}_{11} = \gamma_{21}\rho_{22} + \gamma_{31}\rho_{33} + i\left(\tilde{\Omega}_p\rho_{21} - \tilde{\Omega}_p^*\rho_{12} + \tilde{\Omega}_t\rho_{31} - \tilde{\Omega}_t^*\rho_{13}\right), \tag{3.14a}$$

$$\dot{\rho}_{22} = -(\gamma_{21} + \gamma_{23})\rho_{22} - i\left(\tilde{\Omega}_p\rho_{21} - \tilde{\Omega}_p^*\rho_{12} + \tilde{\Omega}_c\rho_{23} - \tilde{\Omega}_c^*\rho_{32}\right), \tag{3.14b}$$

$$\dot{\rho}_{33} = \gamma_{23}\rho_{22} - \gamma_{31}\rho_{33} - i\left(\tilde{\Omega}_c^*\rho_{32} - \tilde{\Omega}_c\rho_{23} + \tilde{\Omega}_t\rho_{31} - \tilde{\Omega}_t^*\rho_{13}\right), \tag{3.14c}$$

$$\dot{\rho}_{12} = -\left(\Gamma_{12} + i\Delta_p\right)\rho_{12} - i\left[e^{i\delta t}\left(\tilde{\Omega}_c\rho_{13} - \tilde{\Omega}_t\rho_{32}\right) + \tilde{\Omega}_p\left(\rho_{11} - \rho_{22}\right)\right], \tag{3.14d}$$

$$\dot{\rho}_{13} = -\left(\Gamma_{13} + i\Delta_t\right)\rho_{13} - i\left[e^{-i\delta t}\left(\tilde{\Omega}_c^*\rho_{12} - \tilde{\Omega}_p\rho_{23}\right) + \tilde{\Omega}_t\left(\rho_{11} - \rho_{33}\right)\right], \tag{3.14e}$$

$$\dot{\rho}_{23} = -(\Gamma_{23} - i\Delta_c)\rho_{23} - i\left[e^{i\delta t}\left(\tilde{\Omega}_t\rho_{21} - \tilde{\Omega}_p^*\rho_{13}\right) + \tilde{\Omega}_c^*(\rho_{22} - \rho_{33})\right], \tag{3.14f}$$

$$\rho_{ij}^* = \rho_{ji}, \quad \text{and} \quad \sum_{j=1}^{3}\rho_{jj} = 1. \tag{3.14g}$$

Here, $\delta = (\Delta_c + \Delta_t - \Delta_p)$ is the three photon detuning. The above equations are normalized with respect to γ_{21} and solved using 5^{th} order Runge Kutta method with initial conditions: $\rho_{11} = 1, \rho_{22} = \rho_{33} = 0$ $\forall z$. In Eq. (3.14), the overdots stand for time derivatives and "*" denotes complex conjugate. The decay rate of population form state $|i\rangle$ to $|j\rangle$ are denoted by γ_{ij} and the decoherence rate of ρ_{12}, ρ_{23}, ρ_{13} are given as $\Gamma_{12} = (\gamma_{21} + \gamma_{23})/2$, $\Gamma_{23} = (\gamma_{21} + \gamma_{23} + \gamma_{31})/2$, $\Gamma_{13} = \gamma_{31}/2$, respectively. The data for longitudinal and transverse relaxation rates pertaining to the vibrational levels given in table. 3.1 are unavailable. However, we assume $\gamma_{21} = \gamma_{23} = \gamma_{31} = \gamma \approx 10^{12}Hz$, which is of the order of the reorientation rate of molecules in solution [116].

3.2.2 Propagation equations

To study the spatiotemporal evolution of the probe pulse and the CW control field, the following Maxwell-Bloch equations are obtained under the slowly varying envelope approximation (SVEA),

$$\left(\frac{\partial}{\partial z} + \frac{1}{c}\frac{\partial}{\partial t}\right)\tilde{\Omega}_p(z,t) = i\eta_p'\rho_{21}(z,t), \tag{3.15a}$$

$$\left(\frac{\partial}{\partial z} + \frac{1}{c}\frac{\partial}{\partial t}\right)\tilde{\Omega}_c(z,t) = i\eta_c'\rho_{23}(z,t). \tag{3.15b}$$

Here η_i' $(i = p, c)$ are called the coupling constants of the respective fields:

$$\eta_p' = n_p \eta_p \left| \frac{J_{n_p}(z_{21}^p f_p(t)) J_0(z_{21}^c f_c(t)) J_0(z_{21}^t f_t(t))}{z_{21}^p} \right|^2,$$
$$\eta_c' = n_c \eta_c \left| \frac{J_0(z_{23}^p f_p(t)) J_{n_c}(z_{23}^c f_c(t)) J_0(z_{23}^t f_t(t))}{z_{23}^c} \right|^2,$$

where $\eta_i = 3N\lambda_i^2\gamma/8\pi$, with N being the number of molecules per unit volume, and λ_i, the wavelength of respective fields. To facilitate numerical integration of Eq. (3.15), a frame moving at the speed of light in vacuum, c is used. The necessary coordinate transformations for that are $\tau = t - z/c$, and $\zeta = z$. This allows for the round bracketed terms of Eq. (3.15) to be replaced by partial derivatives with respect to the single independent variable ζ. The propagation dynamics of the third field have been ignored for simplicity.

3.3 Results

In presence of PDM, the usual Rabi frequencies, Ω_i get modified as, $\tilde{\Omega}_i$, inside the medium. Figure 3.2 shows the variation of modified Rabi frequencies of the probe, control, and the third field concerning the usual control Rabi frequency. In Fig. 3.2,

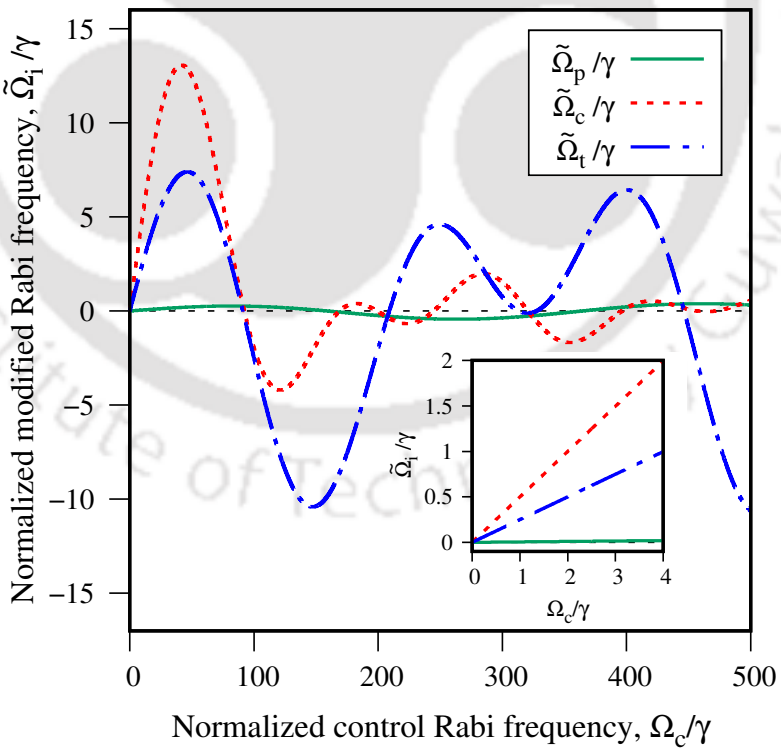

Figure 3.2: $\tilde{\Omega}_i/\gamma$ vs Ω_c/γ. Parameters used: $n_p = n_c = n_t = 1$ (meaning all three corresponding to probe, control and the third field are one photon transitions, respectively), $\Omega_p = 0.01\Omega_c$, $\Omega_t = 0.5\Omega_c$, $\Delta_p = \Delta_c = \Delta_t = 0$.

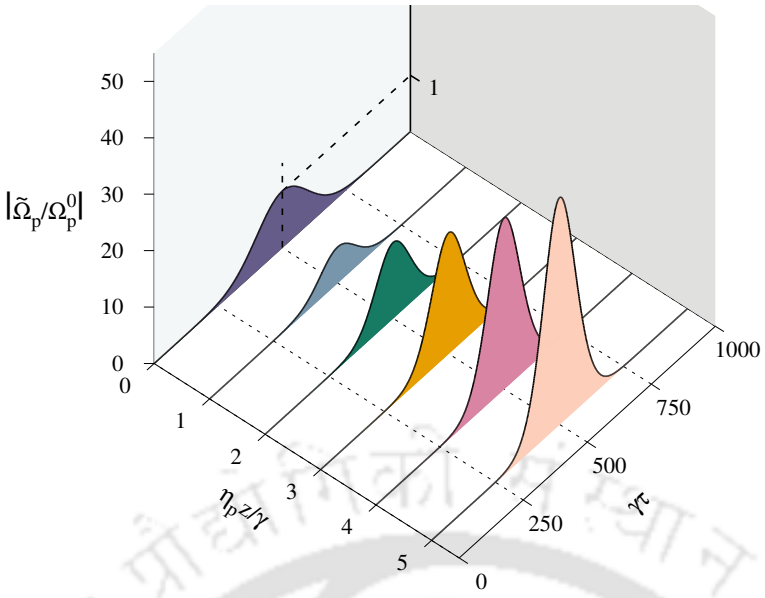

Figure 3.3: $\left|\tilde{\Omega}_p/\Omega_p^0\right|$ vs $\gamma\tau$ at different normalized propagation length, $\eta_p z/\gamma$. Parameters used: $n_p = 1, n_c = n_t = 1$ (meaning all three transitions are one photon), $\Omega_p = 0.01\Omega_c$, $\Omega_t = 0.5\Omega_c$, $\Omega_c = 1\gamma$, $\Delta_p = \Delta_c = \Delta_t = 0$, $\sigma_0 = 100/\gamma$, $\tau_0 = 500/\gamma$. Here, Ω_p^0 denotes the usual probe Rabi frequency at $z = 0$. The right and left z axes represent normalized probe field magnitude at $z = 0$ and $z > 0$, respectively.

the modified Rabi frequencies show oscillatory behavior with respect to Ω_c/γ due to the presence of Bessel functions in the expressions of $\tilde{\Omega}_i$ as seen in Eq. (3.10). However, within the experimentally feasible value of Ω_c, the variation of $\tilde{\Omega}_i$ with Ω_c is linear as shown in the inset plot of Fig. 3.2.

We shall investigate the propagation of a weak Gaussian probe pulse in presence of a continuous wave (CW) control and the third field, i.e.,

$$f_p(\tau) = \exp[-\frac{(\tau-\tau_0)^2}{2\sigma_0^2}],\ f_c(\tau) = 1,\ \text{and}\ f_t(\tau) = 1. \tag{3.16}$$

Here, σ_0 and τ_0 are the probe pulse width and delay, respectively at the entrance of the medium. We first consider the one photon excitation case, i.e., all three fields are considered to exciting one photon transitions ($n_p = n_c = n_t = 1$). Figure 3.3 shows the temporal profile of the Gaussian probe pulse at different normalized propagation length, $\eta_p z/\gamma$. In Fig. 3.3, the probe pulse can be seen getting amplified without any broadening and delay. Figure 3.4 shows the temporal profile of the CW control field at different normalized propagation length, $\eta_p z/\gamma$. In Fig. 3.4, the continuous control field amplitude depletes with increasing propagation length as a consequence of the decay of population from state $|3\rangle$ to $|1\rangle$. Also its envelop gets distorted inwards in the shape of the Gaussian probe pulse due to the interdependence of the modified control Rabi frequency on the time profile of the probe as seen in Eq. (3.10b). The probe amplification can be understood by considering the population distribution in the three states. Figure 3.5 shows the population distribution in the states, $|1\rangle$, $|2\rangle$, and $|3\rangle$, respectively at the normalized propagation length $\eta_p z/\gamma = 5$. Unlike an usual three level Λ system in atomic vapour, the $|1\rangle \leftrightarrow |3\rangle$ transition in Fig. 3.1 is not dipole forbidden for a polar molecular system, and the interaction

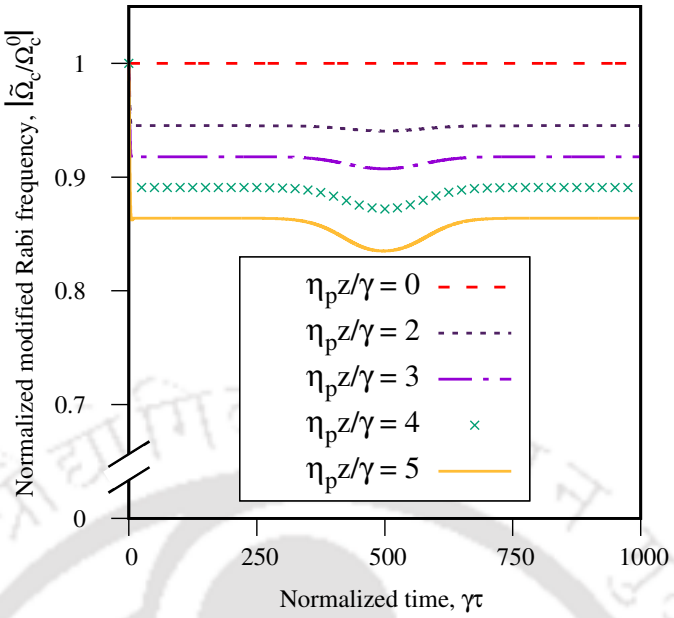

Figure 3.4: $\left|\tilde{\Omega}_c/\Omega_c^0\right|$ vs $\gamma\tau$ at different normalized propagation length, $\eta_p z/\gamma$. Parameters used are same as Fig. 3.3. Here, Ω_c^0 denotes the probe Rabi frequency at $z = 0$.

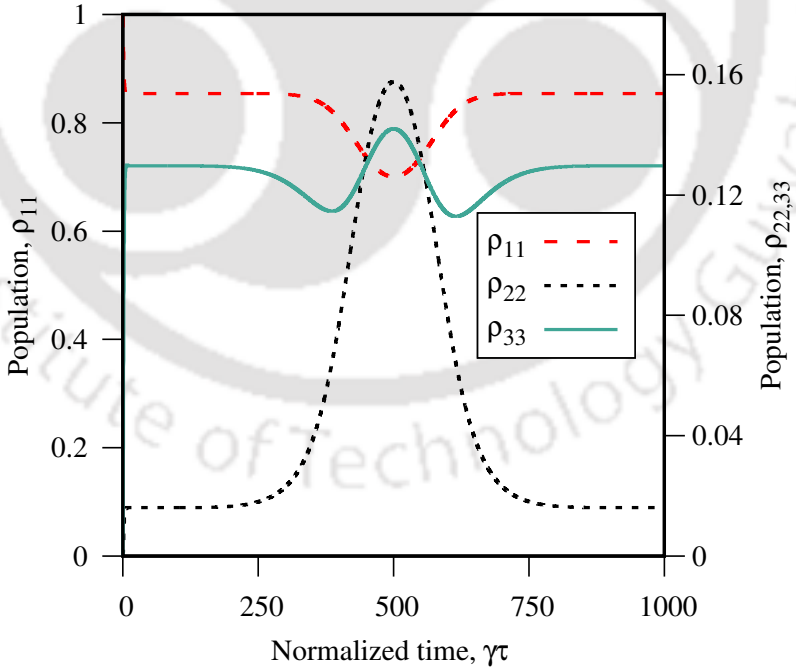

Figure 3.5: Population, ρ_{ii} vs $\gamma\tau$ at normalized propagation length, $\eta_p z/\gamma = 5$. Parameters used are same as Fig. 3.3.

strength of the third field with the induced dipole moment for $|1\rangle \leftrightarrow |3\rangle$ transition is

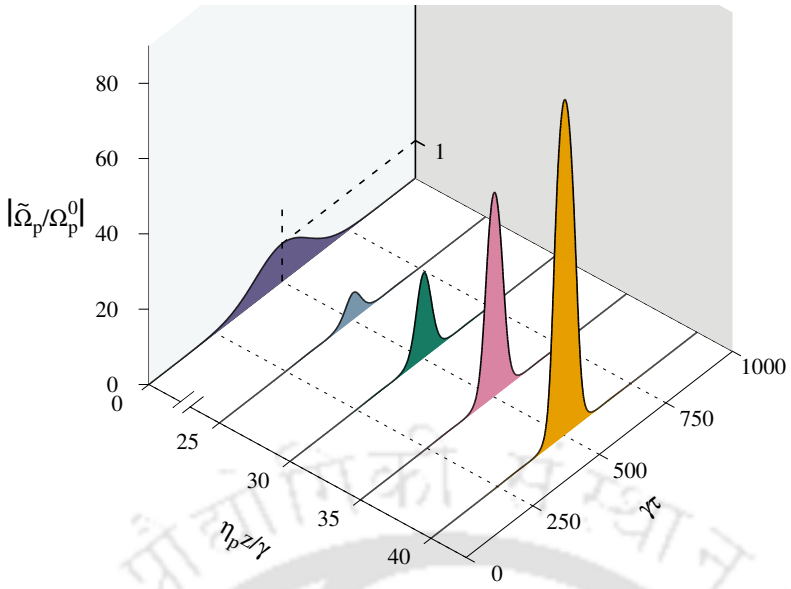

Figure 3.6: $\left|\tilde{\Omega}_p/\Omega_p^0\right|$ vs $\gamma\tau$ at different normalized propagation length, $\eta_p z/\gamma$. Parameters used: $n_p = 1, n_c = n_t = 2$, meaning probe transition is one photon, while rest two are two photon. All parameters remain same as Fig. 3.3, except control field Rabi frequency at $z = 0$ is taken to be, $\Omega_c = 2\gamma$. The right and left z axes represent normalized probe field magnitude at $z = 0$ and $z > 0$, respectively.

high enough to cause population transfer from $|1\rangle$ to $|3\rangle$. The population from $|3\rangle$ is then excited to the state $|2\rangle$ due to the presence of strong control field in $|3\rangle \leftrightarrow |2\rangle$ channel. The nonzero population in the excited state, $|2\rangle$ can then decay to state $|1\rangle$ via stimulated emission in presence of the probe pulse, causing probe amplification. The nonzero population in the excited state can be seen in Fig. 3.5.

Next we consider the case where the control and the third field transitions are two-photon transitions while the probe transition is one photon, i.e., $n_p = 1$, $n_c = n_t = 2$. Figure 3.6 shows the temporal profile of the probe pulse at different normalized propagation length, $\eta_p z/\gamma$. In Fig. 3.6, the probe pulse is amplified with increasing propagation length due to the same population redistribution process mentioned earlier in Fig. 3.5. However, here the probe field has a frequency of ω_{21} while the control field has a frequency, of $\omega_{23}/2$ which is close to half of the probe frequency from table 3.1. Thus in presence of PDM, due to unprohibited two-photon excitation, it is possible to amplify a probe signal with the help of another signal whose frequency is half of the probe signal's frequency.

3.4 Conclusion

In conclusion, we have investigated the propagation of a weak Gaussian probe pulse through a closed-loop Λ system with permanent dipole moments (PDM) in presence of a strong continuous wave control field and a third field. The presence of PDMs leads to modified Rabi frequencies of the fields inside the medium which show oscillatory behavior with respect to their corresponding Rabi frequencies in absence of PDM. In presence of PDMs, all phenomenons are required to be explained in

terms of these modified Rabi frequencies instead of the usual Rabi frequencies to get correct results. The presence of PDMs enables multiphoton excitation for the probe, control, and the third field transitions which are not possible in absence of PDMs. This allows for the possibility to amplify a probe signal, with a frequency that is twice the control field. In case of atomic vapor medium, closed Λ system or triangular ($\triangle$) system has been extensively studied, for example: Wilson *et al.* [117] studied the absorption and dispersion spectrum for the $\triangle$ system, both theoretically and experimentally. They reported the presence of three transparency windows and explained their results through dressed state analysis. Li *et al.* [118] experimentally showed in triangular system that the EIT can be controlled by changing the relative phase between the optical and the microwave fields. Eilam *et al.* [119] theoretically studied storage and retrieval of light pulse in triangular system and showed that the retrieved pulse can be amplified depending on the phase of the microwave field. Davuluri *et al.* [120] have theoretically proposed an experiment to generate coherent backward and forward microwave in Rb vapor using forward-propagating optical fields in Λ system. Korociński *et al.* [121] studied pulse propagation in triangular system without three photon resonance condition and showed that an input Gaussian pulse develops a multi-peak spectrum as it propagates through the triangular system. A similar study of pulse propagation has been done in a higher level, closed double Λ configuration by Raczyński *et al.* [122]. For a collective study on commonly considered closed multilevel systems, the work by Kosachiov *et al.* [123] is a comprehensive article, where they showed the dependence on phases of electromagnetic fields in closed level system.

Chapter 4

Vector beam polarization rotation control using magneto optic effect

4.1 Introduction

In this work, we illustrate a scheme to control the rotation of a VB's polarization structure, using the magneto-optic effect [124] in a four-level tripod atomic system [125]. The three transitions of the four-level tripod atomic system are driven by a strong control field and the two left and right circular polarization components of a weak VB. In presence of an external magnetic field, the magneto-optic effect creates a difference in the refractive indices of the two VB polarization components. We have derived an expression relating this difference in refractive indices with the polarization orientation at any point on the VB's transverse plane. The difference between refractive indices of the two VB components can be varied by changing the magnetic field strength. Thus, providing a means to control the rotation of the polarization structure of a VB. This method also makes it possible to switch between radial, azimuthal, and spiral polarization states of a CV beam, by varying the magnetic field strength. Some related works on VB polarization rotation can be found in [126, 127, 128, 129]. The proposed technique is a simple way to fully control the polarization rotation of a weak VB at any propagation length, by merely varying the magnetic field. Due to the EIT of the tripod system, possible absorption during the rotation process is also avoided. At high intensities of VB, polarization rotation per unit change of magnetic field decreases, and nonlinear effects such as "self-focusing" [11] become prominent. In the end, we discuss the effect of inhomogeneous broadening on polarization rotation.

This chapter is organized into the following sections. Sec. 4.2 gives the theoretical formalism for the four-level tripod system and the expression for the polarization rotation angle of the VB. Sec. 4.3 collates all the results with their explanations. Finally, Sec. 4.4 presents our conclusions.

4.2 Theoretical formulation

4.2.1 Level system

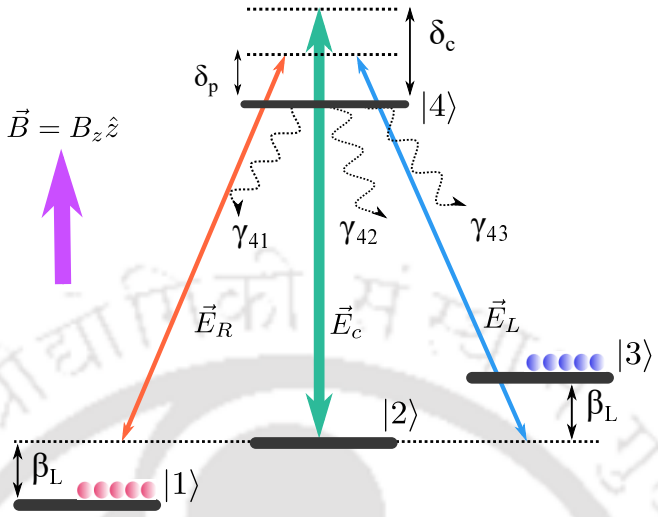

Figure 4.1: Schematic diagram of a four level tripod system. A longitudinal magnetic field, $\vec{B} = B_z\hat{z}$ generates the Zeeman sublevels, $|1\rangle$, $|2\rangle$, and $|3\rangle$ with an energy separation of $\hbar\beta_L$ between them. The energy of $|2\rangle$ is indiscriminately set to zero and $|4\rangle$ is taken as the excited state. The right circularly polarized component, $\vec{E}_R$ and the left circularly polarized component, $\vec{E}_L$, of a weak probe VB couples the transitions, $|1\rangle \leftrightarrow |4\rangle$ and $|3\rangle \leftrightarrow |4\rangle$, respectively. The transition, $|2\rangle \leftrightarrow |4\rangle$ is coupled by a π polarized, strong control field, $\vec{E}_c$. The spontaneous emission decay rate from $|4\rangle$ to $|j\rangle$ $(j = 1, 2, 3)$ is denoted by γ_{4j}. The detunings of the probe and control fields are denoted by δ_p and δ_c, respectively.

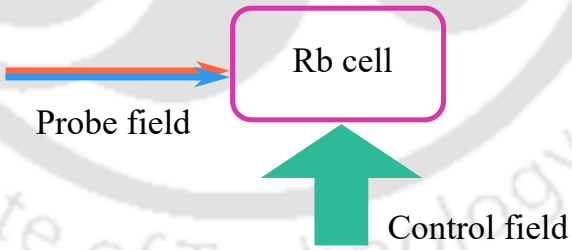

Figure 4.2: Top view of the beam configuration with respect to the vapor medium.

We consider a four level tripod system as shown in Fig. 4.1. A weak probe VB, traveling along the positive z axis, couples both, $|1\rangle \leftrightarrow |4\rangle$ and $|3\rangle \leftrightarrow |4\rangle$ transitions, with its right circularly polarized component, $\vec{E}_R$ and left circularly polarized component, $\vec{E}_L$, respectively. Consequently, by selection rules, the strong control field, $\vec{E}_c$ coupling $|2\rangle \leftrightarrow |4\rangle$ transition is a π polarized wave traveling along x or y axis. The configuration in Fig. 4.1 can be realized with Rubidium (Rb) atomic vapour in presence of an external magnetic field, by choosing the Zeeman sublevels of ^{87}Rb D_2 $(5^2S_{1/2} \rightarrow 5^2P_{3/2})$ transition hyperfine structure as: $|1\rangle = |5^2S_{1/2}, F = 1, m_F = -1\rangle$, $|2\rangle = |5^2S_{1/2}, F = 1, m_F = 0\rangle$, $|3\rangle = |5^2S_{1/2}, F = 1, m_F = +1\rangle$, and the excited state $|4\rangle = |5^2P_{3/2}, F = 0, m_F = 0\rangle$. The probe and control fields are defined as:

$$\vec{E}_p(r,t) = [\hat{e}_R\mathcal{E}_R(r,t) + \hat{e}_L\mathcal{E}_L(r,t)]\, e^{-i(\omega_p t - \vec{k}_p.\vec{r})} + \text{c.c.}, \tag{4.1}$$

$$\vec{E}_c(r,t) = \hat{e}_c\mathcal{E}_c(r,t)e^{-i(\omega_c t - \vec{k}_c.\vec{r})} + \text{c.c.}, \tag{4.2}$$

where $\hat{e}_{R(L)}$, are the right (left) circular polarization unit vectors, $\mathcal{E}_{R(L)}(r,t)$ are the slowly varying envelope functions for right (left) polarization components of the probe VB, $\omega_{p(c)}$ are the field carrier frequency, and $\vec{k}_{p(c)}$ are the wave vector. Similarly, $\hat{e}_c$ and $\mathcal{E}_c(r,t)$ are the polarization unit vector and slowly varying envelope function of the control field.

The time-dependent Hamiltonian of the four-level tripod system in Fig. 4.1, under the electric dipole approximation, is given as:

$$\boldsymbol{H} = \boldsymbol{H}_0 + \boldsymbol{H}_B + \boldsymbol{H}_I, \tag{4.3a}$$

$$\boldsymbol{H}_0 = \hbar\omega_{42}|4\rangle\langle 4|, \tag{4.3b}$$

$$\boldsymbol{H}_B = g_F\mu_B\hat{F}\cdot\vec{B} = \hbar\beta_L\left(|3\rangle\langle 3| - |1\rangle\langle 1|\right), \tag{4.3c}$$

$$\begin{aligned}\boldsymbol{H}_I &= -\,\hat{\boldsymbol{d}}\cdot\vec{E} \\ &= -\Big[|1\rangle\langle 4|\vec{d}_{14}.\left(\hat{e}_R\mathcal{E}_R e^{-i\omega_p t} + \hat{e}_R^*\mathcal{E}_R^* e^{i\omega_p t}\right) + |2\rangle\langle 4|\vec{d}_{24}.\left(\hat{e}_c\mathcal{E}_c e^{-i\omega_c t} + \hat{e}_c^*\mathcal{E}_c^* e^{i\omega_c t}\right) \\ &\quad + |3\rangle\langle 4|\vec{d}_{34}.\left(\hat{e}_L\mathcal{E}_L e^{-i\omega_p t} + \hat{e}_L^*\mathcal{E}_L^* e^{i\omega_p t}\right)\Big] + \text{h.c.},\end{aligned} \tag{4.3d}$$

where, "$*$" denotes complex conjugate, ω_{42} is the frequency separation between state, $|4\rangle$ and ground state, $|2\rangle$, $\vec{d}_{i4} = \langle i|\hat{\boldsymbol{d}}|4\rangle$ $(i = 1,2,3)$ are matrix elements of the dipole moment operator $\hat{\boldsymbol{d}}$, representing the induced dipole moments of $|i\rangle \leftrightarrow |4\rangle$ transition. The magnitude of Zeeman shift between the states $|1\rangle$, $|2\rangle$, $|3\rangle$ is given by $\beta_L = g_F\mu_B B/\hbar$, where g_F and μ_B are the Lande g factor and Bohr magneton, respectively. To write the Hamiltonian in a time independent form, the following unitary transformation is used:

$$\hat{\boldsymbol{U}} = \exp\left[-i\omega_p t|4\rangle\langle 4| - i(\omega_p - \omega_c)t|2\rangle\langle 2|\right]. \tag{4.4}$$

The effective Hamiltonian obeying the Schrödinger equation, in the transformed basis is given by $\boldsymbol{\mathcal{H}} = \hat{\boldsymbol{U}}^\dagger\boldsymbol{H}\hat{\boldsymbol{U}} - i\hbar\hat{\boldsymbol{U}}^\dagger\partial_t\hat{\boldsymbol{U}}$, which under the rotating wave approximation gives:

$$\begin{aligned}\frac{\boldsymbol{\mathcal{H}}}{\hbar} = -\Big[&\beta_L|1\rangle\langle 1| + (\delta_p - \delta_c)\,|2\rangle\langle 2| - \beta_L|3\rangle\langle 3| + \delta_p|4\rangle\langle 4| \\ &+ \Omega_R|4\rangle\langle 1| + \Omega_c|4\rangle\langle 2| + \Omega_L|4\rangle\langle 3|\Big] + \text{h.c},\end{aligned} \tag{4.5}$$

In Eq. (4.5), the one photon detunings, $\delta_{p(c)}$ and Rabi frequencies, Ω_i of the fields are given by:

$$\delta_{p(c)} = \omega_{p(c)} - \omega_{42}, \quad \Omega_i = \frac{\vec{d}_{4j}.\hat{e}_i\mathcal{E}_i}{\hbar}, \ (i = R,c,L, \text{ and } j = 1,2,3 \text{ respectively}). \tag{4.6}$$

The dynamics of atomic state populations and coherences is governed by the following Liouville equation:

$$\partial_t\boldsymbol{\rho} = -\frac{i}{\hbar}[\boldsymbol{\mathcal{H}}, \boldsymbol{\rho}] + \boldsymbol{\mathcal{L}}_\rho, \tag{4.7}$$

where, the density matrix, $\boldsymbol{\rho}$ is given by $\boldsymbol{\rho} = \sum_{i,j=1}^{4} \rho_{ij}|i\rangle\langle j|$. The diagonal elements, ρ_{ii} represent the population of state $|i\rangle$ and obey the population conversation equation, $\sum_{i=1}^{4} \rho_{ii} = 1$. The nondiagonal elements obey, $\rho_{ij}^{*} = \rho_{ji}$. The Liouville operator, $\boldsymbol{\mathcal{L}}_{\rho}$ describes all incoherent processes and can be expressed as: $\boldsymbol{\mathcal{L}}_{\rho} = -\sum_{j=1}^{3} \gamma_{4j}/2\left(|4\rangle\langle 4|\boldsymbol{\rho} - 2|j\rangle\langle j|\rho_{44} + \boldsymbol{\rho}|4\rangle\langle 4|\right)$, where γ_{4j} represents the radiative decay rates from the excited state, $|4\rangle$ to state, $|j\rangle$. For simplicity, we assume, $\gamma_{4j} = \gamma$.

4.2.2 Propagation equations

The beam propagation equations for $\vec{E}_{R(L)}$ are derived from the Maxwell's equation, under the slowly varying envelope and paraxial wave approximations. The propagation equations in terms of the respective field envelopes are given as:

$$\frac{1}{2ik_R}\nabla_{\perp}^{2}\mathcal{E}_R + \frac{\partial \mathcal{E}_R}{\partial z} = 2\pi i\mathcal{N}k_p d_{14}\rho_{41}, \quad \frac{1}{2ik_L}\nabla_{\perp}^{2}\mathcal{E}_L + \frac{\partial \mathcal{E}_L}{\partial z} = 2\pi i\mathcal{N}k_p d_{34}\rho_{43}, \tag{4.8}$$

where $\mathcal{N}$ is the atomic density of the medium. The definitions of the remaining quantities in Eq. (4.8) are same as mentioned in Sec. 4.2.1. The strong control field, $\vec{E}_c$ being a plane wave, its propagation dynamics are ignored in presence of the weak fields, $\vec{E}_{R,L}$.

4.2.3 Refractive index of medium

Under the weak probe approximation $\left(|\vec{E}_c| >> |\vec{E}_{R(L)}|\right)$, at steady state, $\rho_{11} = \rho_{33} = 1/2$ and $\rho_{22} = \rho_{44} = \rho_{42} = \rho_{24} = 0$. Under this steady state condition, the coherences, ρ_{41} and ρ_{43}, are given as:

$$\rho_{41} = -\frac{\Omega_R}{2}\left[\frac{1 + \frac{|\Omega_L|^2}{A}}{\Delta_{14} + \frac{|\Omega_c|^2}{\Delta_{12}^{*}} + \frac{|\Omega_L|^2}{\Delta_{13}^{*}}\left(1 + \frac{|\Omega_R|^2}{A}\right)}\right], \tag{4.9a}$$

$$\rho_{43} = -\frac{\Omega_L}{2}\left[\frac{1 - \frac{|\Omega_R|^2}{B}}{\Delta_{34} - \frac{|\Omega_c|^2}{\Delta_{23}} - \frac{|\Omega_R|^2}{\Delta_{13}}\left(1 - \frac{|\Omega_L|^2}{B}\right)}\right] \tag{4.9b}$$

$$A = \Delta_{34}^{*}\Delta_{13}^{*}\left[1 - \left(\frac{|\Omega_R|^2}{\Delta_{34}^{*}\Delta_{13}^{*}} + \frac{|\Omega_c|^2}{\Delta_{34}^{*}\Delta_{23}^{*}}\right)\right]$$

$$B = \Delta_{14}^{*}\Delta_{13}\left[1 + \left(\frac{|\Omega_L|^2}{\Delta_{14}^{*}\Delta_{13}} + \frac{|\Omega_c|^2}{\Delta_{14}^{*}\Delta_{12}}\right)\right]$$

In Eq. (4.9), $\Delta_{1(3)4} = \delta_p \mp \beta_L + i\Gamma_{1(3)4}$ and $\Delta_{24} = \delta_c + i\Gamma_{24}$, $\Delta_{12} = \beta_L - (\delta_p - \delta_c) + i\Gamma_{12}$, $\Delta_{13} = 2\beta_L + i\Gamma_{13}$, and $\Delta_{23} = \beta_L + (\delta_p - \delta_c) + i\Gamma_{23}$. Here Γ_{ij} and Γ_{i4} are the decoherence rates of ρ_{ij} and ρ_{i4}, respectively $(i < j;\ i, j = 1, 2, 3)$. The refractive indices corresponding to $\vec{E}_{R(L)}$ can then be written in terms of medium susceptibility as:

$$n_R = 1 + 2\pi \mathrm{Re}[\chi_{41}] \quad \text{and} \quad n_L = 1 + 2\pi \mathrm{Re}[\chi_{43}], \tag{4.10}$$

where, the medium susceptibility corresponding to $\vec{E}_{R(L)}$ are given as: $\chi_{41(3)} = \tilde{\eta}\rho_{41(3)}/\Omega_{R(L)}$ with $\tilde{\eta} = 3\mathcal{N}/2k_p^3$.

4.2.4 Polarization rotation angle

A VB can be represented as a vector superposition of two orthogonally polarized, Laguerre-Gaussian modes. In the circular polarization basis, a VB is written as:

$$\vec{E}(r,\phi,z) = \mathcal{E}_L(r,\phi,z)\hat{e}_L + \mathcal{E}_R(r,\phi,z)\hat{e}_R, \tag{4.11}$$

where,

$$\mathcal{E}_L(r,\phi,z) = \cos(\alpha)LG_0^{l_L}, \text{ and } \mathcal{E}_R(r,\phi,z) = e^{i\theta}\sin(\alpha)LG_0^{l_R}, \tag{4.12}$$

are the left and right circularly polarized field components of the VB. Here, α and θ determines the relative amplitude and phase between the two modes, respectively, and $LG_0^{l_i}$ $(i = R, L)$ are the Laguerre-Gaussian modes, with the radial index set to zero for simplicity;

$$\begin{aligned} LG_0^{l_i}(r,\phi,z) =& C_l \left(\frac{r\sqrt{2}}{w(z)}\right)^{|l_i|} \exp\left[\frac{-r^2}{w(z)^2}\right] \exp\left[\frac{ik_p^f n_i r^2 z}{2(z^2+n_i^2 z_R^2)}\right] \\ &\times \exp\left[il_i\phi - i(|l_i|+1)\eta(z) + ik_p^f n_i z\right]. \end{aligned} \tag{4.13}$$

The coefficient, $C_l = E_i^{(0)}\sqrt{2/\pi|l_i|!}$ with $E_i^{(0)}$ being the field amplitude, l_i is the OAM index, and ϕ is the azimuthal angle. The free space Rayleigh length is defined as $z_R = k_p^f w_0^2/2$, where w_0 is the beam waist and k_p^f is the free space wave number. The beam radius at a propagation distance z is $w(z) = w_0\sqrt{1+z^2/n_i^2 z_R^2}$, where n_i is the refractive index. The Gouy phase is given by $(|l_i|+1)\eta(z)$ with $\eta(z) = \tan^{-1}(z/n_i z_R)$. The Stokes parameters in the circular polarization basis are given by:

$$S_0 = |\mathcal{E}_R|^2 + |\mathcal{E}_L|^2,\ S_1 = 2\mathrm{Re}[\mathcal{E}_R^*\mathcal{E}_L],\ S_2 = 2\mathrm{Im}[\mathcal{E}_R^*\mathcal{E}_L],\ S_3 = |\mathcal{E}_R|^2 - |\mathcal{E}_L|^2. \tag{4.14}$$

The ellipticity, ζ and orientation, ξ of the polarization at each point on the transverse plane can be calculated using:

$$\frac{S_1}{S_0} = \cos(2\zeta)\cos(2\xi),\ \frac{S_2}{S_0} = \cos(2\zeta)\sin(2\xi),\ \frac{S_3}{S_0} = \sin(2\zeta) \tag{4.15}$$

From Eq. (4.14) and Eq. (4.15), orientation, ξ is given by:

$$\xi = \frac{1}{2}\tan^{-1}\left(\frac{S_2}{S_1}\right) = \frac{1}{2}\tan^{-1}\left(\frac{\mathrm{Im}[\mathcal{E}_R^*\mathcal{E}_L]}{\mathrm{Re}[\mathcal{E}_R^*\mathcal{E}_L]}\right). \tag{4.16}$$

Substituting Eqns. [(4.12), (4.13)] in Eq. (4.16) gives:

$$\begin{aligned} \xi(z) = -\frac{1}{2}\Bigg[&\theta + \eta(z)\Delta(|l_{L,R}|) + \phi\Delta(l_{L,R}) + k_p^f z\Delta(n_{R,L}) \\ &+ \frac{k_p^f z r^2}{2}\left(\frac{n_R}{z^2+n_R^2 z_R^2} - \frac{n_L}{z^2+n_L^2 z_R^2}\right)\Bigg], \end{aligned} \tag{4.17}$$

where $\Delta|l_{L,R}| = |l_L| - |l_R|$, $\Delta l_{L,R} = l_L - l_R$, and $\Delta(n_{R,L}) = n_R - n_L$. From Eq. (4.17), after propagating a distance z through the medium, the polarization at each point on the VB's transverse plane would rotate by an angle:

$$\begin{aligned} \Delta\xi = \xi(z) - \xi(0) = -\frac{1}{2}\Delta|l_{L,R}|\eta(z) - \Bigg\{&\frac{1}{2}k_p^f z\Delta(n_{R,L}) \\ &+ \frac{k_p^f z r^2}{4}\left(\frac{n_R}{z^2+n_R^2 z_R^2} - \frac{n_L}{z^2+n_L^2 z_R^2}\right)\Bigg\}. \end{aligned} \tag{4.18}$$

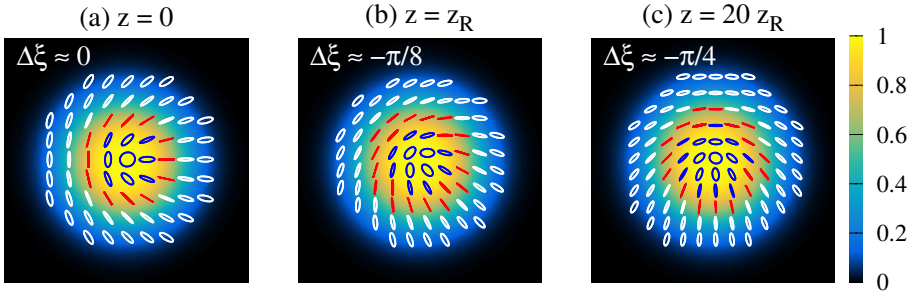

Figure 4.3: (a), (b), (c): Transverse intensity and polarization distribution for a VB with "lemon" polarization structure ($l_L = 0$, $l_R = 1$, $\theta = 0$, $\alpha = \pi/4$) at $z = 0$, $z = z_R$, and $z = 20z_R$, respectively. Throughout the chapter, the beam waist is taken as, $w_0 = 60$ μm and the white, red, blue colors of polarization correspond to right circular, linear, and left circular polarisation, respectively. Also, beam diffraction doesn't affect polarization rotation, hence it has been ignored in all figures similar to Fig. 4.3 for visual clarity. The field intensity has been normalized to unity.

4.3 Results and analysis

4.3.1 Free space propagation

In free space, where $n_L = n_R = 1$ or inside any medium where $n_L = n_R$, Eq. (4.18) gives:

$$\Delta\xi = -\frac{1}{2}\Delta|l_{L,R}|\eta(z). \tag{4.19}$$

The above equation suggests that VBs with $|l_R| = |l_L|$, *e.g.*, CV beams, are polarization invariant in a media where $n_R = n_L$. On the other hand, VBs with $|l_R| \neq |l_L|$, *e.g.*, FP beams, undergo a Gouy phase dependent rotation of their polarization structure. In free space, at $z = z_r$, $\eta(z_r) = \pi/4$, thus for a VB with "lemon" polarization distribution ($l_L = 0$, $l_R = 1$, $\theta = 0$, $\alpha = \pi/4$), the polarization rotation angle would be:

$$\Delta\xi = -\frac{\pi}{8}\Delta|l_{L,R}| = -\frac{\pi}{8}. \tag{4.20}$$

The negative sign in Eq. (4.20) represents clockwise rotation. Figure 4.3 shows the polarization rotation of a VB with "lemon" polarization distribution at different propagation lengths. In Fig. 4.3(b), after a free space propagation of one Rayleigh length, the entire polarization structure has rotated by an angle $\pi/4$ instead of $\pi/8$ as predicted in Eq. (4.20). This is because the rotation of the polarization structure as a whole depends on the rotational symmetry of the polarization pattern. Nonetheless, the polarization at each point on the transverse plane does rotate by $\pi/8$. In the far field regime ($z \to \infty$), for the "lemon" polarization distribution, Eq. (4.19) gives, $\Delta\xi \to -\pi/4$. Figure 4.3(c) shows the transverse polarization distribution at $z = 20z_R$, representing the far field regime. In Fig. 4.3(c), the polarization structure has rotated clockwise by $\pi/2$, and not $\pi/4$, for the same reason as Fig. 4.3(b). The results shown in Fig. 4.3 are consistent with some of the related works [126, 127]. In the following sections, we will discuss how the four level tripod system (Fig. 4.1) can be used to achieve full control over the polarization rotation.

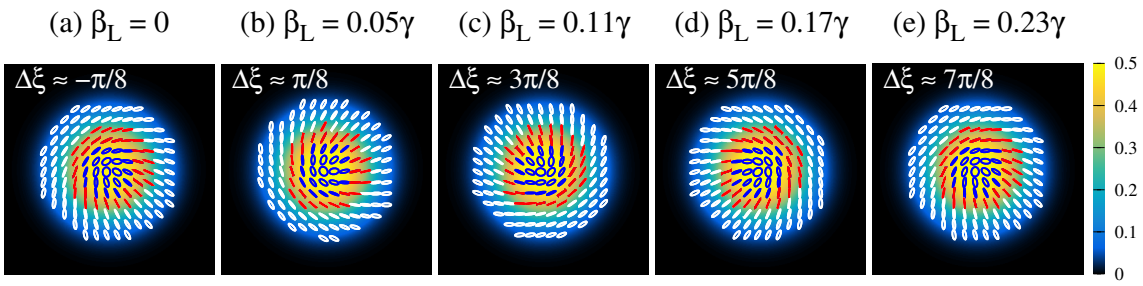

Figure 4.4: (a)-(e): Transverse intensity and polarization distribution for a VB with "lemon" polarization structure ($l_L = 0$, $l_R = 1$, $\theta = 0$, $\alpha = \pi/4$) at $z = z_R$, for different values of β_L. All figures from (a) to (e) are obtained, keeping $\delta_c = 0$. The rabi frquencies of the fields at $z = 0$ are taken as $\Omega_c = 4\gamma$, $\Omega_{R(L)} = 0.05\gamma$. The decoherence rates are taken as $\Gamma_{ij} \approx 10^{-3}\gamma$ and $\Gamma_{i4} = 3/2\gamma$ $(i < j,\ i, j = 1, 2, 3)$. The density of atoms, $\mathcal{N} = 2 \times 10^{11}$ cm^{-3}. The field intensity has been normalized with respect to the field intensity at $z = 0$. The negative sign on the polarization rotation angle shown on top of figure (a) signifies clockwise rotation.

4.3.2 Polarization rotation control

In this section, we present a scheme to control the polarization rotation of a VB using the tripod atomic system, shown in Fig. 4.1. In Fig. 4.1, the probe carrier frequency, ω_p, is made equal to the transition frequency, ω_{42}, of $|2\rangle \leftrightarrow |4\rangle$ transition (*i.e.*, $\delta_p = 0$). In this way, $\vec{E}_R$ and $\vec{E}_L$ will be red and blue detuned, respectively by an amount β_L. The parameter β_L is the frequency shift between the Zeeman triplets, $|1\rangle$, $|2\rangle$, and $|3\rangle$. The equal and opposite detunings experienced by $\vec{E}_{R(L)}$ causes them to have unequal refractive indices ($n_R \neq n_L$). This asymmetry in refractive index is the crux of achieving the desired polarization rotation of a VB. Note that the control field is considered resonant ($\delta_c = 0$) throughout the chapter. With the configuration in Fig. 4.1, increasing β_L by varying the magnetic field strength ($|\vec{B}|$), increases the detunings of $\vec{E}_R$ and $\vec{E}_L$ by equal amount, but opposite sign. This inturn increases the difference between the refractive indices, n_R and n_L, causing the polarization at each point on the VB's transverse plane to rotate according to Eq. 4.18. Figures, 4.4(a) - 4.4(e) show the evolution of transverse intensity and polarization distribution of a "lemon" VB with β_L, at a propagation distance of one Rayleigh length inside the medium. In Figs. 4.4(a) - 4.4(e), the magnetic field strength, $|\vec{B}|$ is increased to raise β_L from 0 to 0.23γ. Thus, increasing the red (blue) detunings of $\vec{E}_{R(L)}$ by an amount of β_L, as mentioned earlier. This correspondingly, increases the difference between n_R and n_L, causing the polarization at each point on the VB's transverse plane to rotate anticlockwise, in accordance with Eq. (4.18). Decreasing $|\vec{B}|$ so as to reduce β_L from 0.23γ to 0 would reverse the process, undoing the rotation. The sense of rotation (clockwise or anticlockwise) in moving from Fig. 4.4(a) to 4.4(e), can be altered by increasing β_L in negative direction, *i.e.*, from 0 to -0.23γ. This can be achieved by inverting the magnetic field direction. The process of polarization rotation as shown in Fig. 4.4, can be understood by studying the medium susceptibility, $\chi_{41(3)}$ associated with $\vec{E}_{R(L)}$ as a function of β_L. Figures 4.5(a) and 4.5(b) show the variation of real and imaginary parts of χ_{4i} with β_L. In Fig. 4.5, as well as throughout the chapter, $\delta_c = 0$ is maintained. The imaginary and

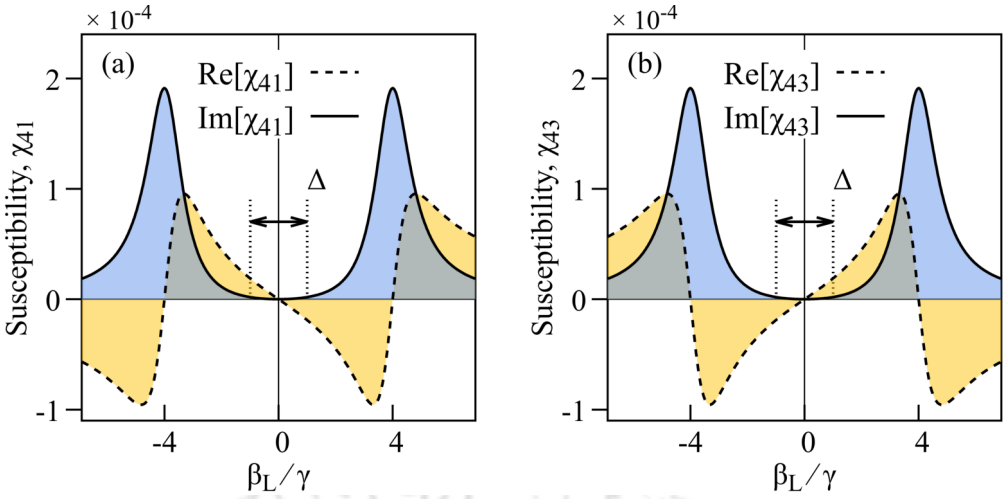

Figure 4.5: (a): Real and imaginary part of χ_{41} vs β_L. (b): Real and imaginary part of χ_{43} vs β_L. The width of EIT window, $\Delta \approx \gamma$. All other relevant parameters used are same as mentioned in Fig. 4.4.

real part of χ_{4i} represents absorption and dispersion, respectively. Figures 4.5(a) and 4.5(b) are laterally inverted mirror images of each other due to the equal and opposite detuning experienced by $\vec{E}_{R(L)}$ as mentioned earlier. In Figs. 4.5(a) and 4.5(b), at any given value of β_L within the EIT window, "Δ", $\mathrm{Re}[\chi_{41}] = -\mathrm{Re}[\chi_{43}]$, making $n_R \neq n_L$ according to Eq. (4.10). Due to $n_R \neq n_L$, there is an additional polarization rotation given by the curly bracketed terms of Eq. (4.18), together with the polarization rotation due to free space propagation, $-\frac{1}{2}\Delta|l_{L,R}|\eta(z)$ [see Eq. (4.19)]. In Figs. 4.5(a) and 4.5(b), at $\beta_L = 0$ (*i.e.*, $\vec{B} = 0$) both the real and imaginary part of χ_{4i} is zero, making $n_{R(L)} = 1$ [see Eq. (4.10)] and absorption zero, respectively, *i.e.*, the medium behaves like free space. Hence, the polarization distribution in Fig. 4.4(a) at one Rayleigh length, is same as Fig. 4.3(b) that shows the polarization distribution after a free space propagation of one Rayleigh length. In Figs. 4.5(a) and 4.5(b), as β_L is raised from 0 to 0.23γ, real parts of both χ_{41}, χ_{43}

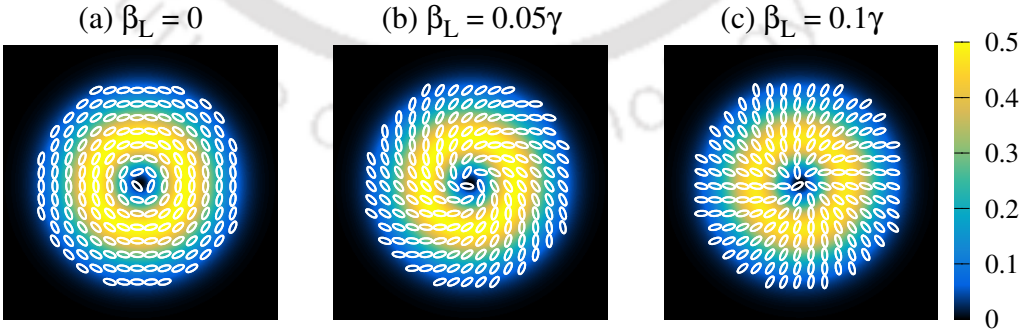

Figure 4.6: (a)-(c): Transverse intensity and polarization distribution for a CVB with azimuthal polarization distribution ($l_L = -1$, $l_R = 1$, $\theta = \pi$, $\alpha = 3\pi/8$) at $z = z_R$ for different values of β_L. The plot shows the transformation of CVB's polarization state from azimuthal at $\beta_L = 0$ [Fig. 4.6(a)], to spiral at $\beta_L = 0.05\gamma$ [Fig. 4.6(b)], and radial at $\beta_L = 0.1\gamma$ [Fig. 4.6(c)]. All other relevant parameters used are same as mentioned in Fig. 4.4.

increases by equal amount, with opposite signs; consequently increasing $\Delta(n_{R,L})$. This causes a polarization rotation at each point on the VB's transverse plane, in accordance with Eq. (4.18), leading to the rotation shown in Figs. 4.4(a) - 4.4(e). To check the fidelity of Eq. (4.18), we measured the rotation angles at random points on the numerically obtained plots such as Fig. 4.4 and then using Eq. (4.18). The numerical and analytical results are in good agreement.

Additionally, it is also possible to transform the polarization state of CV beams to another desired state. Figure 4.6 shows how by varying β_L from 0 to 0.1γ, the polarization structure of the CV beam changes from azimuthal [Fig. 4.6(a)] to spiral [Fig. 4.6(b)] and then to radial [Fig. 4.6(c)]. This sort of transformation is however limited to CV beams and full Poincaré beams or noncylindrical VBs such as lemon, web, and star, don't undergo such transformation.

4.3.3 Effect of control field amplitude

In this section, we discuss the role of control field amplitude in rotating the VB's polarization structure. The choice of Ω_c is determined by the fact that the EIT window width, "Δ" (see Fig. 4.5), should be wide enough to accommodate for a 360^0 polarization rotation with minimal intensity reduction, due to absorption. Figure 4.7(a) shows a plot of polarization rotation angle, $\Delta\xi$ vs β_L/γ for a "lemon" VB, at one Rayleigh length and Fig 4.7(b) shows the corresponding absorption ($\mathrm{Im}[\chi_{41}]$) profile of $\vec{E}_R$ near resonance, for different control field Rabi frequencies. In Fig. 4.7(a), at $\beta_L/\gamma = 0$, all the straight lines intersect at $\Delta\xi = -\pi/8$, which is the polarization rotation angle for free space propagation of one Rayleigh length [see Eq. (4.20)]. This is because at $\beta_L/\gamma = 0$, both $\mathrm{Re}[\chi_{41}] = \mathrm{Re}[\chi_{43}] = 0$ [see Fig. 4.5], making the refractive indices, $n_R = n_L = 1$, according to Eq. (4.10). Thus, causing a polarization rotation of $\Delta\xi = -\pi/8$ after propagation of one Rayleigh length as

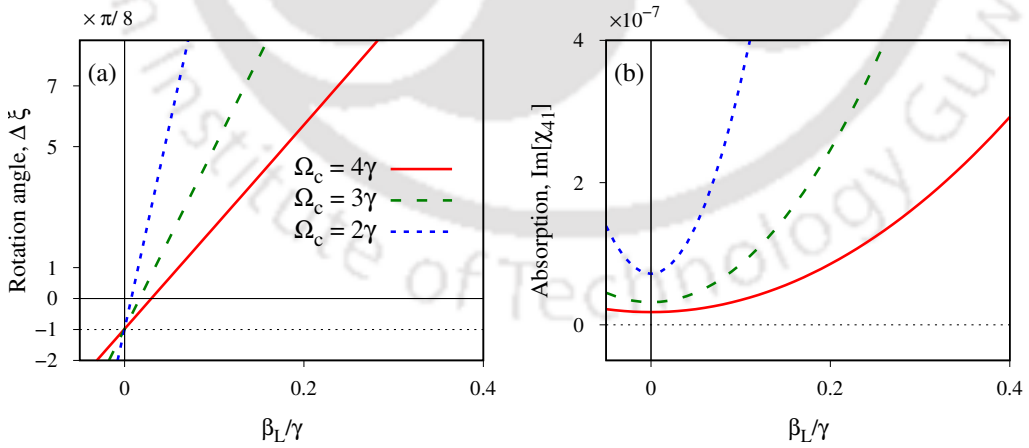

Figure 4.7: (a): Polarization rotation angle, $\Delta\xi$ vs β_L/γ, of a "lemon" VB for different input control Rabi frequencies, at a propagation distance of one Rayleigh length, with a fixed input probe field amplitude. (b): Zoomed plot of $\mathrm{Im}[\chi_{41}]$ vs β_L/γ at the corresponding input control Rabi frequencies. The plot shows the variation of $\Delta\xi$ and $\mathrm{Im}[\chi_{41}]$, with β_L/γ for input control field Rabi frequencies, $\Omega_c/\gamma = 2, 3, 4$. All other relevant parameters and conditions remain same as Fig. 4.4. The negative sign on the vertical axis of figure (a) represents the clockwise rotation of polarization.

shown earlier in Eq. (4.20). The rotation angle from $\Delta\xi = -\pi/8$ to $7\pi/8$ on the left vertical axis of Fig. 4.7(a) represents a 2π anticlockwise rotation of the polarization structure of a "lemon" VB at one Rayleigh length. In Fig. 4.7, as Ω_c/γ is increased from 2 to 4, the slope of the straight lines ($\Delta\xi$ per unit β_L/γ) decreases in Fig. 4.7(a) and the probe absorption within the range, $\beta_L/\gamma \in [0, 0.4]$ becomes flatter in Fig. 4.7(b). We found $\Omega_c = 4\gamma$ to be the optimum value for providing a wide enough EIT window to enable 2π polarization rotation without significant intensity drop due to absorption. For values smaller than $\Omega_c = 4\gamma$, although the rotation rate ($\Delta\xi$ per unit β_L/γ) is higher, the absorption rate (Im[χ_{41}] per unit β_L/γ) is also substantial as seen in Fig. 4.7(b). Hence, as β_L/γ is increased to achieve 2π polarization rotation, field intensity would noticeably deplete towards higher values of β_L/γ. Increasing Ω_c beyond 4γ to get a wider EIT window, would be redundant for achieving the 2π polarization rotation. Therefore, we chose the input control Rabi frequency to be around $\Omega_c = 4\gamma$. In the next section, we discuss the effect of nonlinearity on polarization rotation and VB propagation.

4.3.4 Effect of high probe intensity

At VB intensities, comparable to the control field intensity, the coherences [see Eqs. (4.9a), (4.9b)] calculated using a weak probe approximation $\left(|\vec{E}_{R(L)}| << |\vec{E}_c|\right)$, become invalid. To incorporate the effect of high VB intensity on polarization rotation and beam propagation, the relevant coherences are evaluated numerically by using Gaussian elimination. A comparison between the propagation results for low and

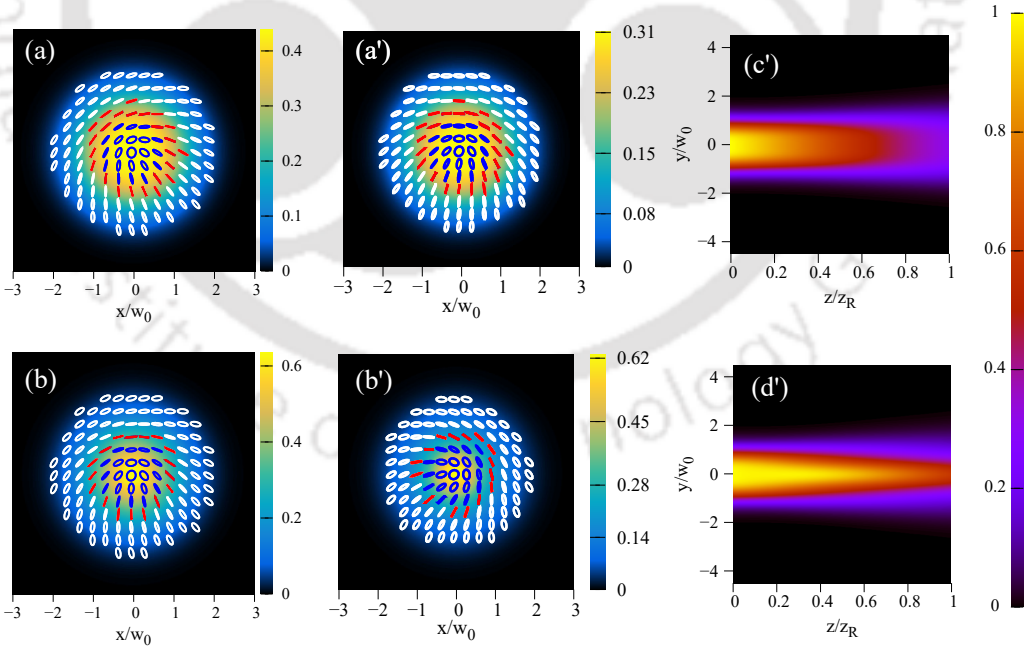

Figure 4.8: Transverse intensity and polarization distribution of a "lemon" VB ($l_L = 0$, $l_R = 1$, $\theta = 0$, $\alpha = \pi/4$) at $z = z_r$, for (a) $\Omega_{R(L)} = 0.1\gamma$ and (b) $\Omega_{R(L)} = 2\gamma$ with $\beta_L = 0.23\gamma$, $\delta_c = 0$, and $\Omega_c = 4\gamma$. Figures (a′) and (b′) are for $\Omega_{R(L)} = 0.1\gamma$ and $\Omega_{R(L)} = 1\gamma$, respectively with $\beta_L = 0.11\gamma$, $\delta_c = 0$, and $\Omega_c = 2\gamma$. Figures (c′) and (d′) are longitudinal intensity profile corresponding to figures (a′) and (b′), respectively. All other parameters, assumptions remain same as Fig. 4.4

high probe intensities is curated in Fig. 4.8. Figures 4.8(a) and 4.8(b) shows a comparison between the transverse intensity profile and polarization rotation of a "lemon" VB for input Rabi frequencies, $\Omega_{R(L)} = 0.1\gamma$ and $\Omega_{R(L)} = 2\gamma$, respectively, with $\Omega_c = 4\gamma$ and $\beta_L = 0.23\gamma$. In Fig. 4.8(b), the polarization rotation for $\Omega_{R(L)} = 2\gamma$ is less compared to $\Omega_{R(L)} = 0.1\gamma$ in Fig. 4.8(a). Also, the beam spot of the high intensity VB [Fig.4.8(b)] is slightly squeezed as compared to the low intensity VB [Fig.4.8(a)], indicating an emergence of the 3rd order nonlinear effect of "self-focusing". The "self-focusing" becomes conspicuous upon lowering the control field intensity, since that leads to a steeper dispersion profile near resonance, and hence higher nonlinear probe ($\vec{E}_{R(L)}$) susceptibility. Figure 4.8(a′)-4.8(d′)shows the transverse intensity and polarization distribution along with the longitudinal intensity profile of a "lemon" VB at one Rayleigh length for an input control field Rabi frequency of $\Omega_c = 2\gamma$, compared to $\Omega_c = 4\gamma$ in Fig. 4.8(a) and 4.8(b). In Fig. 4.8(b′) for a higher intensity VB, its beam spot is distinctively brighter and smaller in diameter than a low intensity VB in Fig. 4.8(a′). Correspondingly, the longitudinal profiles in Fig. 4.8(c′) and 4.8(d′), highlights the "self focusing" in case of the high VB intensity. Therefore, the higher the intensity of VB; the lesser is the polarization rotation at a given, β_L. Moreover, nonlinear effects such as "self-focusing" become evident at high intensities of VB.

4.3.5 Effect of inhomogeneous broadening

In this section, we discuss the effect of "inhomogeneous broadening" [23] on the VB polarization rotation. For an atom moving with velocity $\vec{v}$, the laser frequencies are Doppler shifted in the atom's rest frame by $\vec{k}_i.\vec{v}$, introducing a laser detuning of, $\delta_i + \vec{k}_i.\vec{v}$ $(i = p, c)$. Since different atoms have different $\vec{v}$, they interact inhomogeneously with the laser. This causes an increase in the linewidth of an atomic transition; a phenomenon known as "inhomogeneous broadening". With the modified detuning, the steady-state coherences, ρ_{ij} are given by their average over the one-dimensional

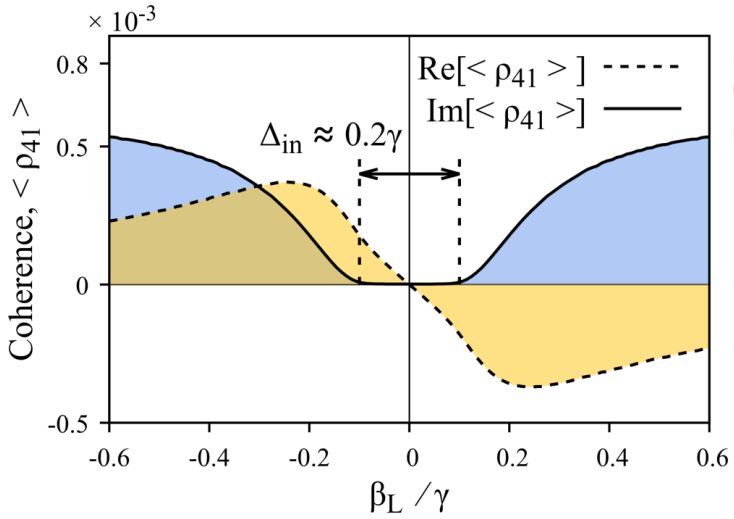

Figure 4.9: Real and imaginary part of Doppler averaged coherence, $< \rho_{41} >$ vs β_L/γ. The temperature is taken as 300 K. All other parameters, assumptions remain same as Fig. 4.4.

Maxwell-Boltzmann velocity distribution [23]:

$$f(v)dv = \sqrt{\frac{M}{2\pi k_B T}} \exp\left(-\frac{Mv^2}{2k_B T}\right) dv, \tag{4.21}$$

where T is the temperature of the gas, M is the mass of each atom, and k_B is the Boltzmann constant. The velocity averaged coherences are then given by $< \rho_{ij} >= \int_{-\infty}^{\infty} \rho_{ij}(v) f(v) dv$.

Figure 4.9 shows the real and imaginary part of $< \rho_{41} >$ vs β_L/γ at a room temperature of $T = 300$ K. All parameters and assumptions used in Fig. 4.9 are same as mentioned in Fig. 4.4. As seen in Fig. 4.9, the width of EIT window for inhomogeneous broadening, $\Delta_{\text{in}} \approx 0.2\gamma$ (see Fig. 4.9), is narrower compared to $\Delta \approx \gamma$ (see Fig. 4.5), in case of homogeneous broadening. Also the absorption (Im$[< \rho_{41} >]$) profile within the EIT window is flatter compared to homogeneous broadening (see Fig. 4.5). In Fig. 4.9, "Δ_{in}" can be made wide enough to achieve a 360^0 polarization rotation by simply increasing the input control Rabi frequency, Ω_c. The presence of inhomogeneous broadening doesn't seem to have any detrimental effect on the flatness of absorption profile within the EIT window as shown in Fig. 4.9. Therefore, it should be possible to perform experiments without the use of cold/ultracold atoms.

4.4 Conclusion

A four-level tripod atomic system exhibits anisotropy in presence of an external magnetic field. This anisotropy creates a difference in the refractive indices of the vector beam's two constituent polarization components. This difference in refractive indices can be varied by changing the magnetic field strength. We show that the polarization orientation at any point on the vector beam's transverse plane has a direct dependence on the difference between the refractive indices of its two polarization components, at that point. Thus, the transverse polarization distribution of a vector beam can be rotated as desired by controlling the external magnetic field strength. This method can also be used to transform the polarization state of cylindrical vector beams between azimuthal, spiral, and radial polarization distributions at any given propagation length inside the medium. During nonlinear propagation, higher intensity of the vector beam leads to a lesser rotation of its polarization structure at a given magnetic field strength and Kerr nonlinearity causes beam focusing. Finally, we show that the polarization rotation procedure is not adversely affected by inhomogeneous broadening and is experimentally viable at room temperature.

Chapter 5

Vector beam guiding using optically written waveguides

5.1 Introduction

In chapter 4 we proposed a scheme to control the polarization rotation of a VB using the anisotropic property of a four level tripod system. In this chapter, we consider a slightly different variation of the same tripod system to achieve waveguiding of VBs inside atomic vapour medium. Our waveguiding method is based on "spatially dependent EIT " [130] and "optically written waveguides" in atomic vapor medium, that was first experimentally demonstrated by Truscott *et al.* [131]. Since then these concepts have been studied for achieving diffraction free propagation [132, 133, 134, 135] and image resolution enhancement [136].

Similar to chapter 4, we consider a four-level tripod system with its three transitions being driven by a strong control field and the two orthogonal polarization components of a probe VB. The strong control field facilitates absorption-less VB propagation through EIT. An external longitudinal magnetic field is employed to induce anisotropy, which creates a difference in the refractive indices of the two orthogonally polarized VB components. This difference in refractive index varies with the magnetic field strength and in turn, enables VB polarization rotation control during propagation. In contrast to the tripod system in chapter 4, here we choose a level configuration that enables both the probe VB and the control beam to co-propagate. With this arrangement, a suitable irradiance profile of the control beam and detuning can create a "core-cladding" type refractive index gradient, facilitating diffraction-less VB propagation for several Rayleigh lengths. The degree of waveguiding can be dynamically controlled via the magnetic field and control field detuning.

This chapter is organized as follows: Sec. 5.2 contains the theoretical formalism used in the work. Sec. 5.3 collates the results of this work with explanations. Finally, Sec. 5.4 contains the conclusion.

5.2 Theoretical formulation

5.2.1 Level system

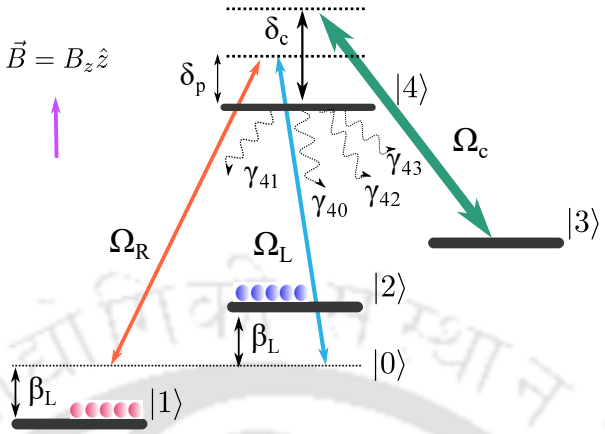

Figure 5.1: Schematic diagram of a four-level tripod system. A magnetic field, $\vec{B} = B_z\hat{z}$ generates the Zeeman sublevels, $|1\rangle$, $|0\rangle$, and $|2\rangle$ with an energy separation of $\hbar\beta_L$ between them. The energy of $|0\rangle$ is indiscriminately set to zero and $|4\rangle$ is taken as the excited state. The right circularly polarized component, $\vec{E}_R$ and the left circularly polarized component, $\vec{E}_L$, of a weak probe VB drives the transitions, $|1\rangle \leftrightarrow |4\rangle$ and $|2\rangle \leftrightarrow |4\rangle$, respectively. The transition, $|3\rangle \leftrightarrow |4\rangle$ is coupled by a strong control field, $\vec{E}_c$. The spontaneous emission decay rate from $|4\rangle$ to $|j\rangle$ $(j = 0, 1, 2, 3)$ is denoted by γ_{4j}. The detunings of the probe and control fields are denoted by δ_p and δ_c, respectively.

Engineering of spatial refractive index in the transverse plane is the key feature for diffraction-free propagation of vector beam through the medium. A suitable modulation of spatial refractive index by the application of spatial dependent control field enables waveguide-like structure inside the medium. In addition, the rotation of the polarization angle in the transverse plane of VB is essentially dependent on the difference in refractive indices of its two components. This variation can be adjusted by a magnetic field. Hence, the manipulation of the spatial refractive index makes it possible to achieve an efficient control over diffraction as well as polarization rotation of VB while it is propagating through the medium. In this regard, a four-level tripod system as shown in Fig. 5.1 is a natural candidate for the fulfillment of the above criteria without absorption. In Fig. 5.1, a longitudinal magnetic field can be used to remove the degeneracy among the states $|1\rangle$, $|0\rangle$ and $|2\rangle$. The energy of $|0\rangle$ is set to be zero and $|4\rangle$ is taken as the excited state. The states $|3\rangle$ and $|4\rangle$ are coupled by a strong control field, $\vec{E}_c$ which is defined as

$$\vec{E}_c(r,t) = \hat{e}_c\mathcal{E}_c(r)e^{-i(\omega_c t - k_c z)} + \text{c.c.}, \tag{5.1}$$

where $\mathcal{E}_c$, $\hat{e}_c$, ω_c, and k_c are the slowly varying envelope, the polarization, the frequency, and the wave vector of the control field, respectively. A weak $\hat{x}$-polarized probe field of frequency ω_p and propagation constant k_p can be decomposed in terms of two orthogonal polarization basis $\hat{\sigma}_i, (i \in R, L)$

$$\vec{E}_p(r,t) = \hat{x}\mathcal{E}_p(\vec{r})e^{-i(\omega_p t - k_p z)} + \text{c.c.} = \sum_{i=R,L} \hat{\sigma}_i\mathcal{E}_i(\vec{r})e^{-i(\omega_p t - k_p z)} + \text{c.c.}, \tag{5.2a}$$

where, the right (left) circularly polarized component, $\mathcal{E}_R$ ($\mathcal{E}_L$) couples $|1\rangle \leftrightarrow |4\rangle$ ($|2\rangle \leftrightarrow |4\rangle$) transition. The level configuration in Fig. 5.1 can be realized with Rubidium (Rb) atomic vapour in the presence of a magnetic field. We choose the Zeeman sublevels of ^{87}Rb D_2 ($5^2S_{1/2} \rightarrow 5^2P_{3/2}$) transition hyperfine structure as: $|1\rangle = |5^2S_{1/2}, F = 1, m_F = -1\rangle$, $|2\rangle = |5^2S_{1/2}, F = 1, m_F = +1\rangle$, which makes $|0\rangle = |5^2S_{1/2}, F = 1, m_F = 0\rangle$. States $|3\rangle$ and $|4\rangle$ can be taken as, $|3\rangle = |5^2S_{1/2}, F = 2, m_F = 1\rangle$ and $|4\rangle = |5^2P_{3/2}, F = 0, m_F = 0\rangle$. The time-dependent Hamiltonian of the system as shown in Fig. 5.1 can be expressed under the electric dipole approximation as

$$\begin{aligned}
\boldsymbol{H} =& \boldsymbol{H}_0 + \boldsymbol{H}_B + \boldsymbol{H}_I, && \text{(5.3a)}\\
\boldsymbol{H}_0 =& \hbar\left(\omega_{40}|4\rangle\langle 4| + \omega_{30}|3\rangle\langle 3|\right), && \text{(5.3b)}\\
\boldsymbol{H}_B =& \hbar\beta_L = g_F\mu_B B, && \text{(5.3c)}\\
\boldsymbol{H}_I =& -\hat{\boldsymbol{d}}\cdot\vec{E}\\
=& -\Big[\vec{d}_{41}\cdot\left(\hat{\sigma}_R\mathcal{E}_R e^{-i\omega_p t} + \text{c.c.}\right)|4\rangle\langle 1| + \vec{d}_{42}\cdot\left(\hat{\sigma}_L\mathcal{E}_L e^{-i\omega_p t} + \text{c.c.}\right)|4\rangle\langle 2|\\
&+ \vec{d}_{43}\cdot\left(\hat{e}_c\boldsymbol{\mathcal{E}}_R e^{-i\omega_c t} + \text{c.c.}\right)|4\rangle\langle 3|\Big] + \text{h.c.}, && \text{(5.3d)}
\end{aligned}$$

where ω_{j0} ($j = 4, 3$) is the frequency separation between state $|j\rangle$ and ground state $|0\rangle$, $\vec{d}_{4i} = \langle 4|\hat{\boldsymbol{d}}|i\rangle$ ($i = 1, 2, 3$) are matrix elements of the dipole moment operator $\hat{\boldsymbol{d}}$, representing the induced dipole moments, corresponding to $|i\rangle \leftrightarrow |4\rangle$ transition. The magnitude of Zeeman shift between the ground state levels are given by $\beta_L = g_F\mu_B B/\hbar$, where g_F and μ_B are the Lande g factor and Bohr magneton, respectively. To remove explicit time dependency in the Hamiltonian H, we use following unitary transformation:

$$\hat{U} = e^{-i\omega_p t|4\rangle\langle 4| - i(\omega_p - \omega_c)t|3\rangle\langle 3|}. \tag{5.4}$$

The effective Hamiltonian obeying the Schrödinger equation, in the transformed basis is given as: $\mathcal{H} = \hat{U}^\dagger H\hat{U} - i\hbar\hat{U}^\dagger\partial_t\hat{U}$, which under rotating wave approximation gives:

$$\begin{aligned}
\frac{\mathcal{H}}{\hbar} =& -\Big[(\delta_p - \delta_c)|3\rangle\langle 3| + \delta_p|4\rangle\langle 4|\Big] + \hbar\beta_L\Big(|2\rangle\langle 2| - |1\rangle\langle 1|\Big)\\
&- \hbar\Big[\Omega_R|4\rangle\langle 1| + \Omega_L|4\rangle\langle 2| + \Omega_c|4\rangle\langle 3|\Big] + \text{h.c.}. && \text{(5.5)}
\end{aligned}$$

In Eq. (5.5), the one photon probe detuning is $\delta_p = \omega_p - \omega_{40}$ and Rabi frequencies for the probe field components are defined as:

$$\Omega_R = \frac{\vec{d}_{41}\cdot\hat{\sigma}_R}{\hbar}\mathcal{E}_R, \text{ and } \Omega_L = \frac{\vec{d}_{42}\cdot\hat{\sigma}_L}{\hbar}\mathcal{E}_L. \tag{5.6}$$

The detuning and Rabi frequency of control is denoted as

$$\delta_c = \omega_c - \omega_{43}, \text{ and } \Omega_c = \frac{\vec{d}_{43}\cdot\hat{e}_c\mathcal{E}_c}{\hbar} \tag{5.7}$$

The dynamics of atomic state populations and coherences are governed by the following Liouville equation:

$$\frac{\partial\boldsymbol{\rho}}{\partial t} = -\frac{i}{\hbar}[\mathcal{H}, \boldsymbol{\rho}] + \mathcal{L}_\rho. \tag{5.8}$$

In the above equation, the Liouville operator, $\mathcal{L}_\rho$ describes all incoherent processes and can be expressed as:

$$\mathcal{L}_\rho = -\sum_{j=1}^{3} \frac{\gamma_{4j}}{2} \left(|4\rangle\langle 4|\rho - 2|j\rangle\langle j|\rho_{44} + \rho|4\rangle\langle 4|\right), \tag{5.9}$$

where γ_{4j} represents the radiative decay rates from the excited state, $|4\rangle$ to ground states, $|j\rangle$. The relevant equations of motion for atomic state populations and coherences of the four-level tripod system are then given by:

$$\dot{\rho}_{44} = -\sum_{i=0}^{3} \gamma_{4i}\rho_{44} + i(\rho_{34}\Omega_c - \rho_{43}\Omega_c^* + \rho_{14}\Omega_R - \rho_{41}\Omega_R^* + \rho_{24}\Omega_L - \rho_{42}\Omega_L^*) \tag{5.10a}$$

$$\dot{\rho}_{41} = i\Delta_{14}\rho_{41} + i\left[\rho_{31}\Omega_c + \rho_{21}\Omega_L + (\rho_{11} - \rho_{44})\,\Omega_R\right] \tag{5.10b}$$

$$\dot{\rho}_{42} = i\Delta_{24}\rho_{42} + i\left[\rho_{32}\Omega_c + \rho_{12}\Omega_R + (\rho_{22} - \rho_{44})\,\Omega_L\right] \tag{5.10c}$$

$$\dot{\rho}_{43} = i\Delta_{34}\rho_{43} + i\left[\rho_{13}\Omega_R + \rho_{23}\Omega_L + (\rho_{33} - \rho_{44})\,\Omega_c\right] \tag{5.10d}$$

$$\dot{\rho}_{11} = \gamma_{41}\rho_{44} + i(\rho_{41}\Omega_R^* - \rho_{14}\Omega_R) \tag{5.10e}$$

$$\dot{\rho}_{12} = i\Delta_{12}\rho_{12} + i(\rho_{42}\Omega_R^* - \rho_{14}\Omega_L) \tag{5.10f}$$

$$\dot{\rho}_{13} = i\Delta_{13}\rho_{13} + i(\rho_{43}\Omega_R^* - \rho_{14}\Omega_c) \tag{5.10g}$$

$$\dot{\rho}_{22} = \gamma_{42}\rho_{44} + i(\rho_{42}\Omega_L^* - \rho_{24}\Omega_L) \tag{5.10h}$$

$$\dot{\rho}_{23} = i\Delta_{23}\rho_{23} + i(\rho_{43}\Omega_L^* - \rho_{24}\Omega_c) \tag{5.10i}$$

$$\dot{\rho}_{33} = \gamma_{43}\rho_{44} + i(\rho_{43}\Omega_c^* - \rho_{34}\Omega_c) \tag{5.10j}$$

$$\rho_{ij} = \rho_{ji}^* \text{ and } \sum_{i=1}^{4} \rho_{ii} = 1. \tag{5.10k}$$

In Eq. (5.10), $\Delta_{14} = \delta_p - \beta_L + i\Gamma_{14}$, $\Delta_{24} = \delta_p + \beta_L + i\Gamma_{34}$, $\Delta_{34} = \delta_c + i\Gamma_{24}$, $\Delta_{12} = 2\beta_L + i\Gamma_{12}$, $\Delta_{13} = \delta_c - \delta_p + \beta_L + i\Gamma_{13}$, $\Delta_{13} = \delta_c - \delta_p - \beta_L + i\Gamma_{23}$. Here, Γ_{ij} and Γ_{i4} are the decoherence rate of ρ_{ij} and ρ_{i4}, respectively. For simplicity, we assume, $\gamma_{4i} = \gamma$. $(i < j;\ i, j \in 0, 1, 2, 3)$.

5.2.2 Refractive index of the medium

A minimum absorption is a prerequisite for VB propagation through the medium. Otherwise, huge absorption can degrade both envelope shape as well as transmission of VB. A strong control field-assisted EIT can make an otherwise opaque medium transparent for a weak probe field. The intensity of the probe field ensures that the perturbation analysis of the system retains the two lowest order contributions while neglecting the higher orders in the expansion under steady-state conditions. Under the assumption of $|\mathcal{E}_c| >> |\mathcal{E}_{R,L}|$, $\rho_{11} = \rho_{22} = 1/2$ and $\rho_{33} = \rho_{44} = \rho_{43} = \rho_{34} = 0$. Hence, the atomic coherences induced by the probe field can be expressed as:

$$\rho_{41} = -\frac{\Omega_R}{2}\left[\frac{1 + \frac{|\Omega_L|^2}{A}}{\Delta_{14} + \frac{|\Omega_c|^2}{\Delta_{13}^*} + \frac{|\Omega_L|^2}{\Delta_{12}^*}\left(1 + \frac{|\Omega_R|^2}{A}\right)}\right], \tag{5.11a}$$

$$\rho_{42} = -\frac{\Omega_L}{2}\left[\frac{1 - \frac{|\Omega_R|^2}{B}}{\Delta_{24} + \frac{|\Omega_c|^2}{\Delta_{23}^*} - \frac{|\Omega_R|^2}{\Delta_{12}}\left(1 - \frac{|\Omega_L|^2}{B}\right)}\right]. \tag{5.11b}$$

The coefficients A and B are defined by

$$A = \Delta_{24}^{*}\Delta_{12}^{*}\left[1 - \left(\frac{|\Omega_R|^2}{\Delta_{24}^{*}\Delta_{12}^{*}} - \frac{|\Omega_c|^2}{\Delta_{24}^{*}\Delta_{23}}\right)\right],$$
$$B = \Delta_{14}^{*}\Delta_{12}\left[1 + \left(\frac{|\Omega_L|^2}{\Delta_{14}^{*}\Delta_{12}} + \frac{|\Omega_c|^2}{\Delta_{14}^{*}\Delta_{13}}\right)\right].$$

The refractive indices for frequencies, $\omega_{R,L}$ can then be written in terms of the coherences given in Eq. (5.11) as:

$$n_R = \sqrt{1 + 4\pi \mathrm{Re}\left[\chi_{41}\right]},\ n_L = \sqrt{1 + 4\pi \mathrm{Re}\left[\chi_{42}\right]} \tag{5.13}$$

where, $\chi_{41(2)} = \tilde{\eta}_{R(L)}\rho_{41(2)}/\Omega_{R(L)}$ is the susceptibility of the medium, and the parameter $\tilde{\eta}_i = 3\mathcal{N}/2k_i^3$ $(i = R, L)$, is a dimensionless constant with $\mathcal{N}$ being the number of atoms per unit volume inside the medium.

5.2.3 Polarization rotation angle

The expression for polarization rotation angle at each point on the VB's transverse plane, after propagation for a distance, z remains same as mentioned in Sec. 4.2.4 of chapter 4, *i.e.*,

$$\Delta\xi(x, y, z) = -\frac{\Delta|l_{L,R}|\eta(z)}{2} - \left\{\frac{k^f z\Delta(n_{R,L})}{2} + \frac{k^f z r^2}{4}\left(\frac{n_R}{z^2 + n_R^2 z_r^2} - \frac{n_L}{z^2 + n_L^2 z_r^2}\right)\right\}, \tag{5.14}$$

where $\Delta|l_{L,R}| = |l_L| - |l_R|$, $\Delta(l_{L,R}) = l_L - l_R$ and $\Delta(n_{R,L}) = n_R - n_L$.

5.2.4 Propagation equations

To investigate the effect of medium properties such as absorption, dispersion, diffraction, and anisotropicity on VB propagation, we study nonlinear Schrödinger equations under the slowly varying envelope and paraxial wave approximations. The beam propagation equations for the right and left circularly polarized components of the probe VB in terms of the respective Rabi frequencies are given as:

$$\frac{\partial\Omega_R}{\partial z} = \frac{i}{2k_R}\nabla_{\perp}^2\Omega_R + \frac{2\pi i k_R\mathcal{N}|d_{14}|^2}{\hbar}\rho_{41}, \tag{5.15a}$$
$$\frac{\partial\Omega_L}{\partial z} = \frac{i}{2k_L}\nabla_{\perp}^2\Omega_L + \frac{2\pi i k_L\mathcal{N}|d_{24}|^2}{\hbar}\rho_{42}. \tag{5.15b}$$

The first terms on the right-hand side stand for the diffraction. The second terms on the right-hand side are responsible for the dispersion and absorption of both the components of probe VB. Note that the two propagation equations are coupled via the susceptibilities ρ_{41} and ρ_{42}. The propagation effect of the control field is neglected since the field is strong and undepleted throughout the length of propagation. Further, the envelope shape of the control field is considered to be diffraction-free Bessel Gaussian.

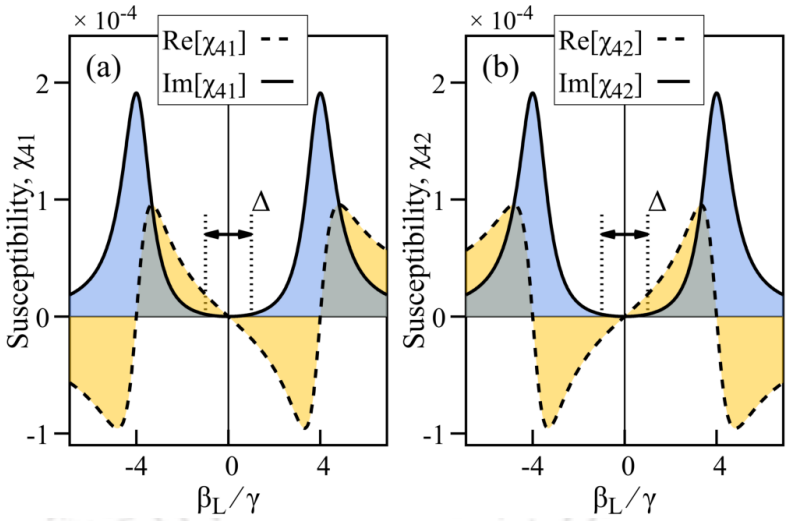

Figure 5.2: (a), (b): Real and Imaginary part of χ_{41} and χ_{42} vs β_L/γ, respectively. Parameters used: $\delta_p = \delta_c = 0$, $\Omega_{R,L} = 0.05\gamma$, $\Omega_c = 4\gamma$, $\Gamma_{ij} = 10^{-3}\gamma$, $\Gamma_{i4} \approx 3/2\gamma$ $(i < j;\ i, j = 1, 2, 3)$ and $\mathcal{N} = 2 \times 10^{11}$ cm^{-3}.

5.3 Results

5.3.1 Polarization rotation control

The orthogonal components of VB must have different refractive indices to produce polarization rotation as stated in the Eq. (5.14). The substantial contrast between n_R and n_L creates large polarization rotation. Hence, the equal and opposite values of $n_{R,L}$ is the basic constraint for producing large polarization rotation. The variation of refractive index in the anisotropic medium is possible by changing the strength of magnetic field. The difference in $n_{R,L}$ can be accomplished by making the probe VB's carrier frequency, ω_p to be resonant with the intermediary state, $|0\rangle$ and excited state, $|4\rangle$ as shown in Fig. 5.1. With this configuration, the magnetic field, responsible for generating Zeeman sublevels, $|1\rangle$, $|0\rangle$, and $|2\rangle$, will red(blue) detune $\Omega_{R(L)}$ by an amount β_L. Due to the equal and opposite nature of detuning experienced by $\Omega_{R(L)}$, their medium responses with respect to β_L become laterally inverted mirror images of each other as shown in Fig. 5.2(a) and 5.2(b), respectively. Therefore, at any given value of β_L, Re$[\chi_{41}]$= −Re$[\chi_{42}]$, as apparent from Figs. 5.2(a) and 5.2(b). This makes, $n_R \neq n_L$ according to Eq. (5.13), giving a nonzero polarization rotation angle, coming from the curly bracketed term in Eq. (5.14). The Zeeman separation, β_L is varied by changing $|\vec{B}|$, to change Re$[\chi_{4i}]$,$(i \in 1, 2)$ as shown in Fig. 5.2(a), 5.2(b), which in-turn causes corresponding changes in $n_{R,L}$ according to Eq. (5.13). Moreover, the requirement of minimum absorption is fulfilled within the range of Δ as depicted in the Fig. 5.2. Thus, enabling control of the polarization rotation angle via magnetic field with zero or minimum absorption.

5.3.2 Vector beam guiding

To guide the VB, the transverse spatial profile of the control beam is to be chosen in such a way that it creates a "core and cladding" type refractive index gradient for the components of VB. To form atomic wave guide structure, the control beam

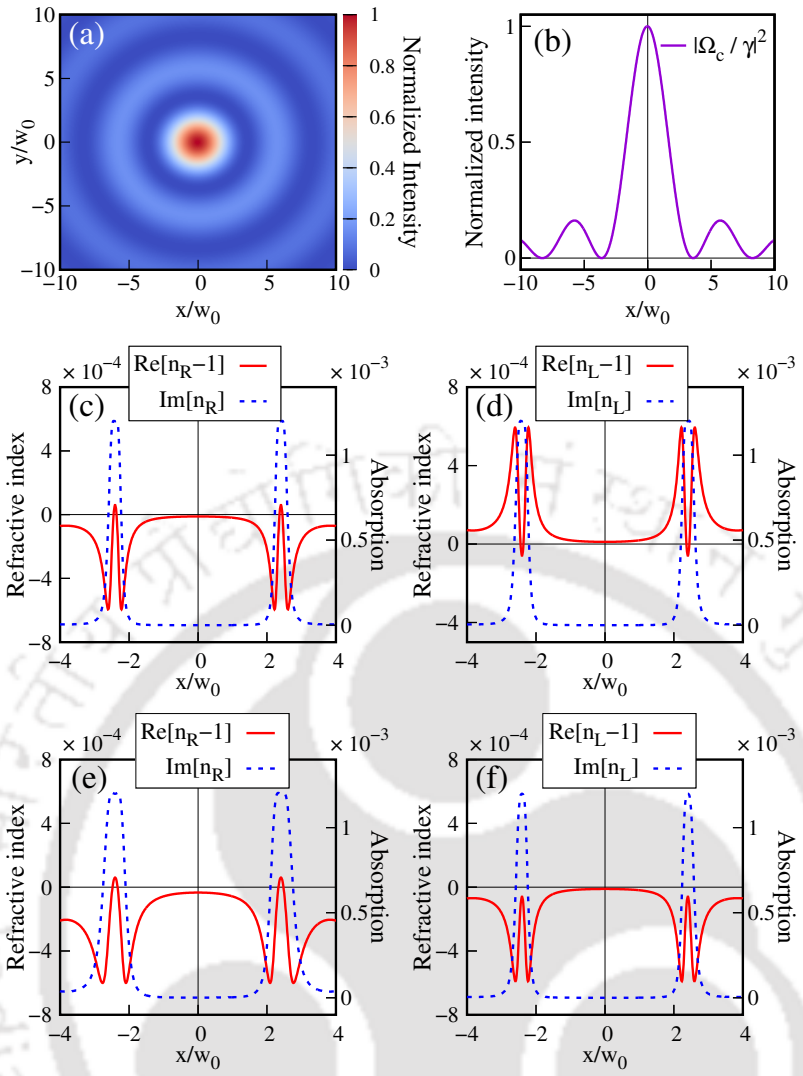

Figure 5.3: (a), (b): Transverse intensity profile of control field. In Figs. (c)-(f), "solid line": Transverse profile of Re[n_i-1] ($i = R, L$) and "dotted line": Transverse profile of Im[n_i] (Absorption). For all the plots, $\delta_p = 0$, $\beta_L = 0.1\gamma$. Plots (c) and (d) are generated with $\delta_c = 0$ while plots (e) and (f), with $\delta_c = 0.2\gamma$. Other parameters used, remain same as mentioned in Fig. 5.2.

profile is taken to be a fundamental zeroth order Bessel beam and is defined as

$$\Omega_c(r, \phi, 0) = \Omega_c^0 \mathcal{J}_0\left(\frac{r}{w_0}\right), r = \sqrt{x^2 + y^2}. \tag{5.16}$$

The input amplitude of the Bessel control beam is denoted by Ω_c^0. The zeroth-order Bessel function of the first kind is denoted as $\mathcal{J}_0(r/w_0)$, where the full width half maximum of the central peak is approximately $2w_0^{-1}$. A Bessel beam undergoes diffractionless propagation inside the medium across several Rayleigh lengths of the probe VB ($> 20z_R$), thus maintaining a consistent refractive index gradient throughout the length of the medium. The envelope shape of the control field is illustrated in Fig. 5.3(a) and 5.3(b). Figs. 5.3(c) and 5.3(d) show the transverse refractive index profile of two orthogonal polarization components of the VB in the presence of a resonant control field, *i.e.*, $\delta_c = 0$, at $\beta_L = 0.1\gamma$. On the other

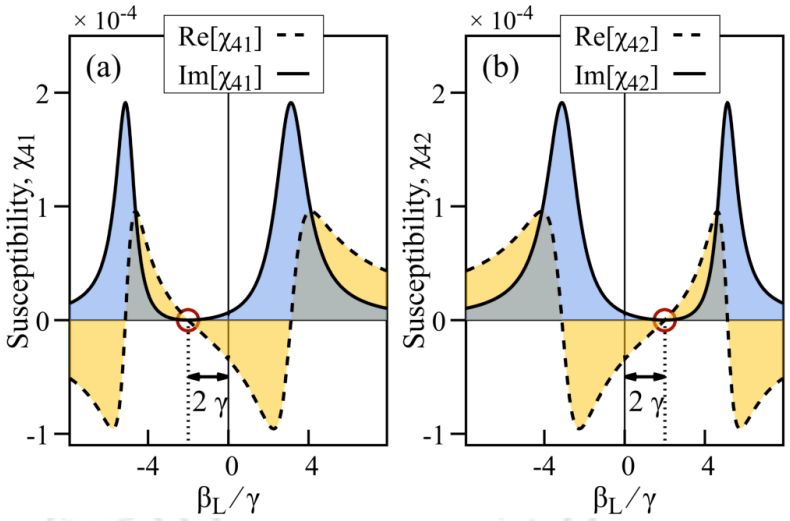

Figure 5.4: (a), (b): Real and Imaginary part of χ_{41} and χ_{42} vs β_L/γ, respectively, with $\delta_p = 0$ and $\delta_c = 2\gamma$. Other parameters used, remain same as mentioned in Fig. 5.2. The small circular markings in (a) and (b) indicates the zero point of $\mathrm{Re}[\chi_{4i}]$ within the EIT window.

hand, Figs. 5.3(e) and 5.3(f), correspond to blue detuned control field $\delta_c = 0.2\gamma$ for same β_L. In Figs. 5.3(c) - 5.3(f), there is a rise or fall in the refractive indices of $\Omega_{R,L}$, around the zeros of the Bessel control beam on x axis. These refractive index extremums and the region between them serve as "cladding" and "core", respectively. For achieving wave guiding features, the core's refractive index needs to be higher than the cladding's, as displayed in Figs. 5.3(c), (e) and (f). Contrarily, there is no guiding when the core's refractive index is smaller than the cladding such as Fig. 5.3(d).

For control field detuning, $\delta_c = 0$, $\mathrm{Re}[\chi_{41}] = -\mathrm{Re}[\chi_{42}]$ at any given value of β_L within the EIT window, Δ as shown in Figs. 5.2(a) and 5.2(b). In Figs. 5.2(a) and 5.2(c), for $\beta_L > 0$, $\mathrm{Re}[\chi_{41}] < 0$ and $\mathrm{Re}[\chi_{42}] > 0$, which makes $n_R < 1$ and $n_L > 1$, in accordance with Eq. (5.13). This is reflected in Figs. 5.3(c) and 5.3(d), where, for $\beta_L = 0.1\gamma > 0$ at $\delta_c = 0$, the transverse profiles of refractive indices, $\mathrm{Re}[n_{R,L}]$ are inverted images of each other. Figs. 5.3(c) and 5.3(d) suggest that the right circularly polarized component, Ω_R will be guided, while the left circularly polarized component, Ω_L will undergo diffraction. Thus, for simultaneous waveguiding of $\Omega_{R,L}$, both $n_{R,L}$ must be less than unity for a given value of β_L and δ_c. This can be achieved by considering a blue detuned control field, $\delta_c > 0$. For example, in Fig. 5.4, at $\delta_c = 2\gamma$, the zero point [marked with small circles] of $\mathrm{Re}[\chi_{41}]$ and $\mathrm{Re}[\chi_{42}]$, within the EIT window, are shifted leftwards and rightwards, respectively by 2γ. As a result, within $-2\gamma < \beta_L < 2\gamma$, both $\mathrm{Re}[\chi_{41}] < 0$ and $\mathrm{Re}[\chi_{42}] < 0$, which implies, $n_{R,L} < 1$. Thus, in general, $\delta_c > 0$ and $-\delta_c < \beta_L < \delta_c$, generates the desired "core-cladding" refractive index profile for both $\Omega_{R,L}$ as shown in Figs. 5.3(e) and 5.3(f), which were plotted by taking $\delta_c = 0.2\gamma > 0$ and $-0.2\gamma < \beta_L = 0.1\gamma < 0.2\gamma$. Again, in Fig. 5.4, for $\delta_c > 0$ and $-\delta_c < \beta_L < \delta_c$, the susceptibilities of $\Omega_{R,L}$ are unequal, *i.e.*, $n_R \neq n_L$. This results in a polarization rotation of the VB during propagation in accordance with Eq. (5.14). With the above parameter constraint in mind, the propagation results for a CV beam are curated in Fig. 5.5. Figs. 5.5(a) and 5.5(b) are the transverse polarization distribution of a CV beam at $z = 0$

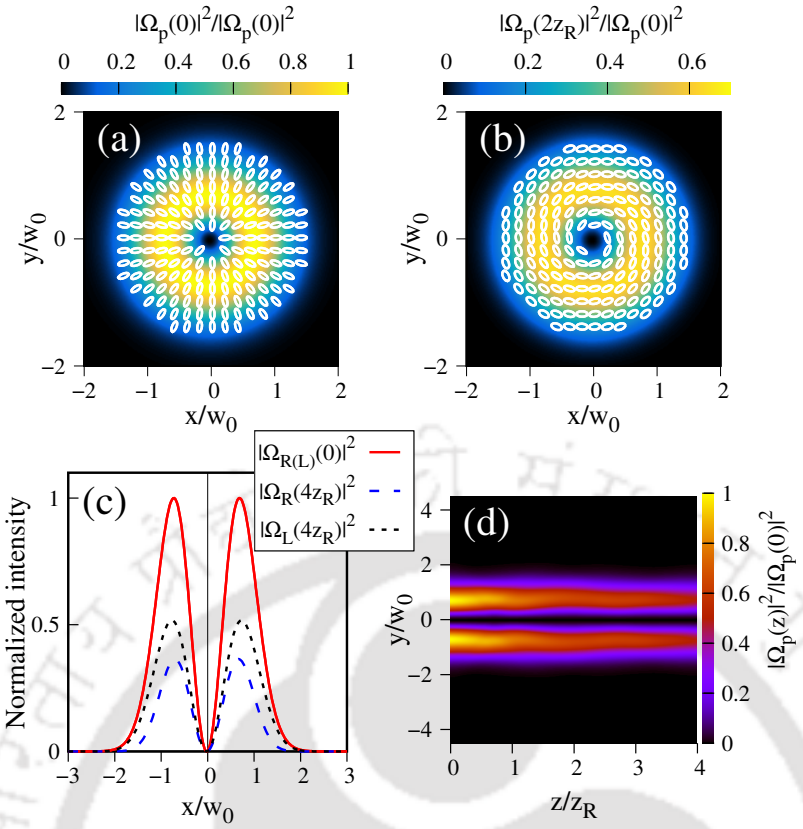

Figure 5.5: (a), (b): Transverse intensity and polarization distribution of a CV beam ($l_L = -1$, $l_R = 1$, $\theta = 0$, $\alpha = \pi/8$) at $z = 0$ and $z = 2z_R$, respectively. (c): Normalized intensity vs x/w_0. (d): Longitudinal intensity profile of the VB. Control field beam waist is taken to be $1.4w_0$, where w_0 is the beam waist of the probe VB. The white color ellipses in (a) and (b) represent left circular polarization. Parameters used: $\delta_c = 0.2\gamma$, $\beta_L = 0.05\gamma$, with rest of the parameters same as Fig. 5.2. Field amplitudes have been normalized with respect to the field amplitude at $z = 0$.

and $z = 2z_R$, respectively. In Fig. 5.5(b) the polarization ellipses at each point on the VB's transverse plane has rotated by a certain angle and its polarization state has changed from radial to azimuthal. With increasing propagation length, the azimuthal distribution will change to spiral and then back to radial in a cyclic manner along the propagation length. This sort of rotation is not observed for CV beams during free space propagation and is a consequence of the magnetic field induced anisotropy. Fig. 5.5(c) shows a comparison between the one dimensional transverse profile of $\Omega_{R,L}$ at a given propagation length. In Fig. 5.5(c), the degree of waveguiding for $\Omega_{R,L}$ are slightly different. This is because within the requisite parameter region for waveguiding, $\delta_c > 0$, $-\delta_c < \beta_L < \delta_c$, the susceptibilities of $\Omega_{R,L}$ are not equal as seen in Fig. 5.4. Fig. 5.5(d) shows the longitudinal profile of the CV beam. In Fig. 5.5(d), the CV beam is smoothly guided upto four Rayleigh lengths, beyond which the VB's intensity noticeably depletes. This is a consequence of the cumulative absorption at the core-cladding boundary [See, Figs. 5.3(e) and (f)] during propagation. In the next section, we shall discuss the factors responsible for smooth waveguiding.

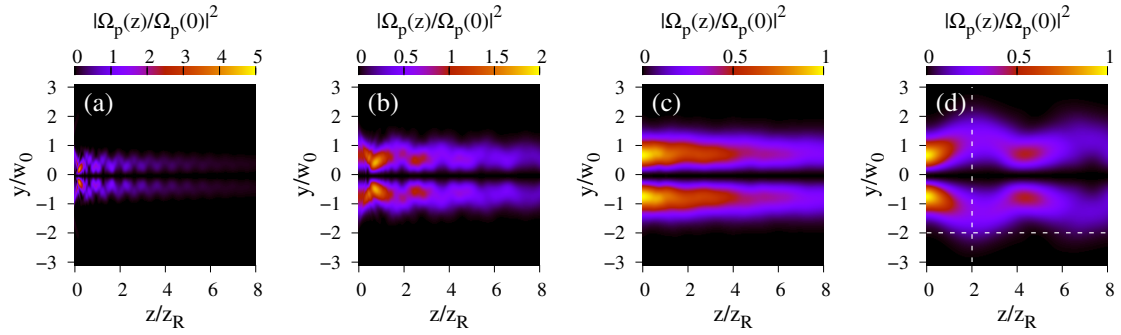

Figure 5.6: (a)-(d): Longitudinal intensity profile of a CV beam ($l_L = -1$, $l_R = 1$, $\theta = 0$, $\alpha = \pi/8$) for control field beam waists $0.5w_0$, w_0, $1.4w_0$, and $2w_0$, respectively. Parameters used: $\delta_c = 0.2\gamma$, $\beta_L = 0.05\gamma$. All other parameters and field amplitude normalization remains same as Fig. 5.5.

5.3.3 Effect of control beam waist

In this section, we discuss how the Bessel control beam's width dictates the guiding of the VB through atomic vapor. The sizes of the Bessel control beam's central lobe and the core of the optically written waveguide are approximately the same. The core's radius can be changed by varying the control beam size. Fig. 5.6, shows the longitudinal profiles of a CV beam for different control beam waists. In Figs. 5.6(a) and 5.6(b), control beam waists are $0.5w_0$ and w_0, respectively. The CV beam exhibits an oscillatory longitudinal variation, closely resembling that of an actual optical fiber. In Fig. 5.6(c), for a control beam waist of $1.4w_0$, the CV beam experiences a smooth guiding. Increasing the control beam waist to $2w_0$ as shown in Fig. 5.6(d), the oscillatory behavior reappears with a larger period compared to Fig. 5.6(a) and 5.6(b). The explanation for Fig. 5.6(d) is as follows: here the Bessel-control beam waist at the medium entrance is $2w_0$, which creates a core of approximately the same radii, $2w_0$. Therefore a probe CV beam of waist, w_0 would undergo broadening due to diffraction until its beam waist becomes equal to the core's radius *i.e.*, $2w_0$. Subsequently, the CV beam would be guided back towards the core's axis due to total internal reflection at the core-cladding boundary. Since the core is a non-absorbing/diffracting media (free space like) as seen in Fig. 5.3(c)-(f); the CV beam would have to propagate approximately two Rayleigh lengths to have a broadened beam waist of, $\approx 2w_0$. This is because the beam waist of an LG beam after free space propagation of two Rayleigh lengths is $\sqrt{5}w_0$ which can be rounded off to $2w_0$. Thus, the CV beam expands and contracts at an interval of two Rayleigh lengths along the longitudinal direction as seen in Fig. 5.6(d). In Fig. 5.6(d), the dotted lines, "$y/w_0 = -2$" and "$z/z_R = 2$", represent the core boundary and position of two Rayleigh length on z axis, respectively. The intersection point of these two lines is where the CV beam is reflected inside the core via total internal reflection. The expansion and contraction observed in Figs. 5.6(a) and 5.6(b) for control beam waists $0.5w_0$ and w_0, respectively is of the same nature as Fig. 5.6(d). In Fig. 5.6(a), the CV beam undergoes rapid compression near the medium entrance due to the core's size being smaller than VB's spot size. After this, the VB undergoes the aforementioned oscillatory longitudinal variation. Same explanation applies to the case in Fig. 5.6(b). In Fig. 5.6(c), the control beam waist is $1.4w_0$ ($\approx \sqrt{2}w_0$), which is approximately the beam waist of an LG beam after

free space propagation of one Rayleigh length. Therefore, the CV beam broadens to about $1.4w_0$ at one Rayleigh length, before undergoing total internal reflection at the core-cladding boundary. The expansion of the CVB from w_0 to $1.4w_0$ is very small and thus results in a smooth guiding. Therefore, to achieve smooth waveguiding, the control beam waist has to lie within a range of approximately $[1.2w_0, 1.6w_0]$. The effect of inhomogeneous broadening on the proposed VB guiding scheme is discussed in appendix B of this thesis.

5.4 Conclusion

In conclusion, we theoretically investigated a vector beam guiding scheme through an atomic vapor medium, with a four-level tripod system. The three transitions of the four-level tripod system are coupled by a strong zeroth-order Bessel control beam and the two orthogonally polarized components of a weak vector beam, in the presence of an external longitudinal magnetic field. With appropriate parameters, the spatial intensity profile of the control beam can create a core and cladding type refractive index gradient along the radial direction from the beam propagation axis. Due to the non-diffractive property of a Bessel beam, the "core-cladding" created by it, remains unchanged across its diffraction-less propagation length. We have shown that a weak vector beam of slightly smaller diameter than the core, is guided through the medium for several Rayleigh lengths. In addition to waveguiding, the magnetic field-induced anisotropy in the four-level tripod system creates a difference in the refractive indices of the vector beam's two orthogonal polarization components. This results in polarization rotation of cylindrical vector beams (CVBs) which are otherwise polarization invariant under free-space propagation. Thus, creating diffraction-less CVBs with polarization gradient across the propagation length, *e.g.*, a radial CVB would change to azimuthal, then to spiral, and back to radial in a periodic manner along the propagation length. Due to the higher focusability of radial over azimuthal CVBs, the ability to change the polarization state of a CVB may be useful in achieving a variable degree of focusing. Furthermore, the vector beam can be squeezed as desired by reducing the control beam's radius. Therefore, as a proof of concept, the proposed scheme can guide a weak vector beam, whilst enabling control over its polarization rotation. Our work may also have applications in polarization-based measurements with vector beams, increasing optical density of a medium, etc. where vector beam focusing, guiding, and polarization rotation control might be simultaneously desired.

Chapter 6

Conclusions and future perspective

In this chapter we summarize the research works in this thesis and mention few potential research ideas.

Conclusion

In this thesis, we have formulated two sets of research problems. The first set is dedicated to the study of pulse amplification in an atomic and molecular vapor medium; discussed in chapters 2 and 3, respectively. The second set deals with polarization manipulation and guiding of vector beams using atomic vapor medium and are covered in chapter 4 and 5, respectively.

In chapter 2, we have proposed a pulse amplification scheme that preserves the input pulse shape and enables absorption free, dispersion free pulse propagation through the medium after amplification. To achieve this, we have considered the Λ system in a resonant gain configuration which is different from the popular EIT configuration, in the sense that, the control and probe fields are swapped with one another. This configuration makes provision for population inversion in the probe transition, causing probe amplification through stimulated emission. With an appropriate control field intensity, the probe pulse is amplified with its initial shape preserved. Posterior to amplification, the pulse travels at the speed of light in vacuum, without any delay, absorption and dispersion, inside the gain medium itself. The proposed scheme also worked for square and sech shaped pulses along with Gaussian. Also, inhomogeneous broadening didn't show any detrimental effect on the amplification process. Therefore, the proposed model system could have applications in optical communication as a signal amplification method for long distance communication.

In chapter 3, we have investigated the propagation of a weak Gaussian probe pulse through a closed-loop Λ system with permanent dipole moments (PDM) in presence of a strong continuous wave control field and a third field. The presence of PDMs leads to modified Rabi frequencies of the fields inside the medium which show oscillatory behavior with respect to their corresponding Rabi frequencies in absence of PDM. In presence of PDMs, all phenomenons are required to be explained in terms of these modified Rabi frequencies instead of the usual Rabi frequencies to get correct results. The presence of PDMs enables multiphoton excitation for the

probe, control, and the third field transitions which are not possible in absence of PDMs. This allows for the possibility to amplify a probe signal, with a frequency that is twice the control field and the third field.

In chapter 4, we proposed a scheme to control the rotation of a vector beam's (VB's) transverse polarization structure. For this, we considered an atomic vapor based four-level tripod system in presence of an external longitudinal magnetic field. The three transitions of the tripod system were coupled by a strong control field and the two orthogonal polarization components of a weak probe VB. The magnetic field induced anisotropy in the four-level tripod atomic system, creates a difference in the refractive indices of the VB's two constituent polarization components. This difference in refractive indices varies with the magnetic field strength and has a direct relation with the polarization orientation at any point on the VB's transverse plane. Thus, the VB's transverse polarization distribution can be rotated as desired by changing the magnetic field strength. With this method, it is possible to waver between azimuthal, spiral, and radial polarization distributions of a cylindrical vector beam (CVB) at any given propagation length inside the medium. The EIT created by the strong control field minimizes any absorption during the polarization rotation procedure. At probe intensities comparable to the control field, we observed self focusing and reduction in polarization rotation, per unit change in magnetic field. Lastly, we showed that, the proposed method is not adversely affected by inhomogeneous broadening and should be experimentally viable at room temperature.

In chapter 4, the probe VB and the strong control field were made to travel orthogonal to each other in compliance with the selection rules of the considered tripod system. In chapter 5, we modified the four-level tripod system so that the probe VB and control field undergo collinear propagation. We then considered the control field to be zeroth-order Bessel beam which is a non-diffracting beam. With appropriate control field detuning, the irradiance profile of the zeroth-order Bessel control beam can create a core and cladding type refractive index gradient for the probe VB, along the radial direction from the beam propagation axis. The "core-cladding" created by the control beam, remains unchanged across the diffraction-less propagation length of the control beam, enabling diffraction less propagation of a weak VB for several Rayleigh lengths. As mentioned in chapter 4, the magnetic field-induced anisotropy in the four-level tripod system leads to polarization rotation of CVBs, which are otherwise polarization invariant under free-space propagation or propagation inside an isotropic medium. This creates a polarization gradient across the propagation length, e.g., a radial CVB would change to azimuthal, then to spiral, and back to radial in a cyclic manner along the propagation length. In conclusion, the proposed scheme can guide a weak VB, whilst enabling some control over its polarization rotation. This could have applications in polarization-based measurements with vector beams, increasing optical density of a medium, etc. where VB focusing, guiding, and polarization rotation control might be simultaneously desired.

Future perspective

Internet has made it possible to collect huge amount of data in various sectors, be it weather data, navigation data, customer purchase data, or any kind of data from

various surveys. These huge data sets, also known as "big data" can be used to train certain computer algorithms to make useful predictions. The branch of computer science dealing with development of such algorithms in popularly known as "*artificial intelligence*" (AI). The ultimate goal of AI is to simulate or even recreate the capabilities of the human mind. The earliest attempt to mathematically formulate the human decision making process was done by logician Walter Pitts and neuroscientist Warren McCullochin in a paper published in 1943. Shortly after that, In 1950, Alan Turning proposed the "*Turing test*", which is test to categorize machines as intelligent or unintelligent. According to the Turing test, when a machine is able to convince a human being that it was also a human, it can be deemed as intelligent. Soon after that, a summer research program on AI held at Dartmouth College, USA in 1956 is now considered as the official birthplace of AI. Since, then the field of AI has seen many ups and downs due to lack of funding, computational power etc. With the developments in computational power and large data bases AI has seen a rebirth during the 2000s.

As of now, AI has been divided into two main subgroups, Machine learning (ML) and deep learning (DL). Machine Learning deals with developing algorithms for computers to be able to perform tasks without the need for explicit programming. Computers are fed structured data (in most cases) and 'learn' to become better at evaluating and acting on that data over time. Deep learning on the other hand tries to model how neurons inside a human brain are fired in performing tasks such as recognizing a cat, a car etc. A deep learning algorithm consists of an interconnected network of artificial neurons, also known as "*artificial neural networks*" (ANN). These ANNs are fed huge amount of data from which the algorithm learns to perform specific task without human aid. The subject of AI seems to be ever growing with its applications being ubiquitous. For example, "Google Translate" an online service from Google, uses machine learning to translate words/sentences from one language to another without human help. Also, In March 2016, "AlphaGo" a computer program using Machine-learning techniques, defeated a world champion in Go, an ancient board game.

In the recent years, ML and DL algorithms have been used for research in physics, chemistry, and biological sciences. We would like to use ML and DL in the topics covered in the thesis, which can be roughly categorized as pulse propagation, Orbital angular momentum (OAM) of light, and vector beams. Few years back, researchers have applied ML (DL) in the aforementioned areas, for example, Boscolo *et al.* [137] used ML to predict the temporal and spectral intensity profiles of pulses for nonlinear propagation in optical fibers. In the field of OAM carrying beams, da Silva *et al.* [138] used Convolutional Neural Network (CNN) for classification of Orbital Angular Momentum (OAM) carrying beams. Similarly, Giordani *et al.* [139] used ML for classification of vector beams. Such applications of ML can eliminate, in some cases, the need for solving the Maxwell's equations or performing experiments. In the context of this thesis, the algorithms used in the aforementioned works, should in principle be applicable in predicting for example, the polarization distribution of vector beams at a given propagation length, without solving the Maxwell's equations. Furthermore, the ML algorithm used by Boscolo et al. for solving the nonlinear Schrödinger equation (NLSE) in time domain could be applied in spatial domain for solving say, the nonparaxial NLSE, which are computationally expensive. The computation time reduction in that case would have noticeable benefit.

Appendix A

Appendix of chapter 2

A.1 Relation between full extent and width of a Gaussian function

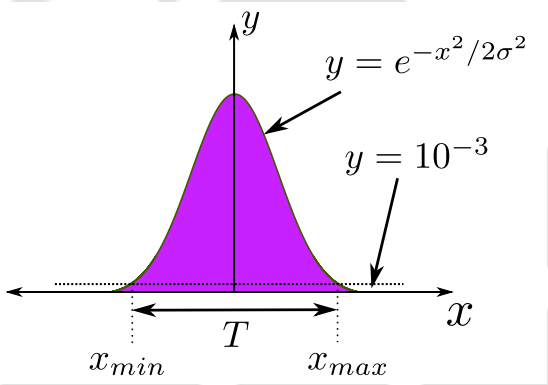

Figure A.1: Gaussian distribution function

In Fig. A.1, the relation between the width, σ of a Gaussian function ($y = e^{-x^2/2\sigma^2}$) and the full extent of the Gaussian function, T (see Fig. A.1) can be approximated by considering an arbitrarily small value say (10^{-3}), and then evaluating the values of x_{min} and x_{max}, where x_{min} and x_{max} are the x coordinates of the intersection points of $y = 10^{-3}$ line with the Gaussian function. From Fig. A.1

$$e^{-x_{min}^2/2\sigma^2} = 10^{-3} \implies x_{min} = -\sqrt{2\sigma^2 \ln(10^3)}, \tag{A.1}$$

and,

$$e^{-x_{max}^2/2\sigma^2} = 10^{-3} \implies x_{max} = \sqrt{2\sigma^2 \ln(10^3)}, \tag{A.2}$$

From Eqs. [(A.1), (A.2)],

$$x_{max} - x_{min} = 2\sqrt{2\sigma^2 \ln(10^3)} \implies T = 2\sqrt{2\ln(10^3)}\sigma. \tag{A.3}$$

A.2 Explanation for noisy output at high control field intensity

For control field amplitudes 5γ or higher, the probe pulse amplification begins a bit earlier as shown in the inset of Fig. A.2, where small traces of amplified probe

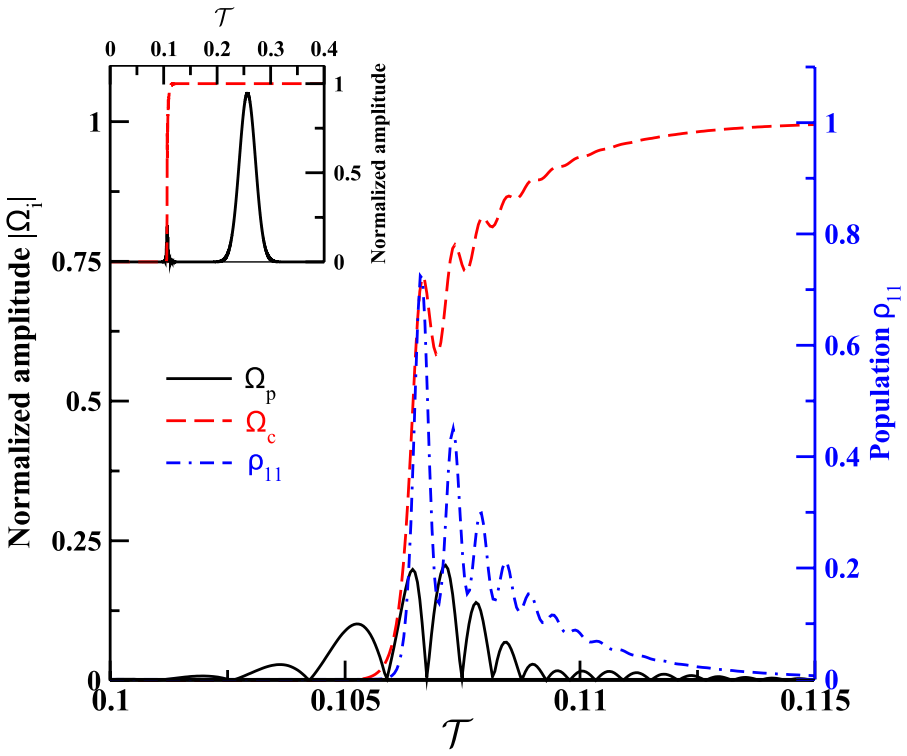

Figure A.2: The normalized field amplitudes ($\Omega_i, i \in p, c$) and population ρ_{11} are plotted against normalized time $\mathcal{T}$ within the medium at $\mathcal{Z} = 2.8$. The inset shows temporal profiles of probe and control amplitudes in the vicinity of $\mathcal{T} = 0.1$.

pulse can be seen at around $\mathcal{T} = 0.1$. In Fig. A.2, at the position of control field's leading end on time axis, ρ_{11} undergoes oscillations. These oscillations are due to the non adiabatic population transfer to the excited state $|1\rangle$ as a result of control field absorption. Such non adiabatic population transfer occurs when there is a steep rise in the control field intensity at its leading end instead of a smooth rise (adiabatic). Similar results have been reported by Harris *et al.* [97] and Laine *et. al.* [140]. In case of a smooth rise of control field intensity, such oscillations are minimal as shown in Fig. A.3(a), whereas prominent oscillations in ρ_{11} is evident from Fig. A.3(b) for the non-adiabatic case. The adiabatic and non-adiabatic switching of the control field is possible by considering a control field envelope of the form $0.5 \times (\tanh[(\tau - T_{on})/\alpha] - \tanh[(\tau - T_{off})/\alpha])$ with probe field as a continuous wave. Here, $T_{on/off}$ denotes the switching on and off times respectively. The parameter α determines how smoothly the control field is switched on and off. Larger the value of α, smoother is the switching on and off. In Fig.A.3(a), $\alpha = 2$, causing an adiabatic transition and in Fig.A.3(b), $\alpha = 0.2$ leading to a non adiabatic transition. Figure A.3 is generated by merely solving the time dependent density matrix equations of the three level Λ given in chapter 2, without considering any propagation of the fields. In Fig. A.3(b), it can be seen that the amplitude as well as frequency of population oscillation in the excited state $|1\rangle$ increases as the control field is switched on in a non adiabatic manner. For the Λ system considered in chapter 2, a smooth rise of control field's amplitude is not possible. Due to the nature of absorption experienced by the control field's leading end during propagation, its leading end eventually becomes steep after propagating some distance inside the medium. This happens irrespective

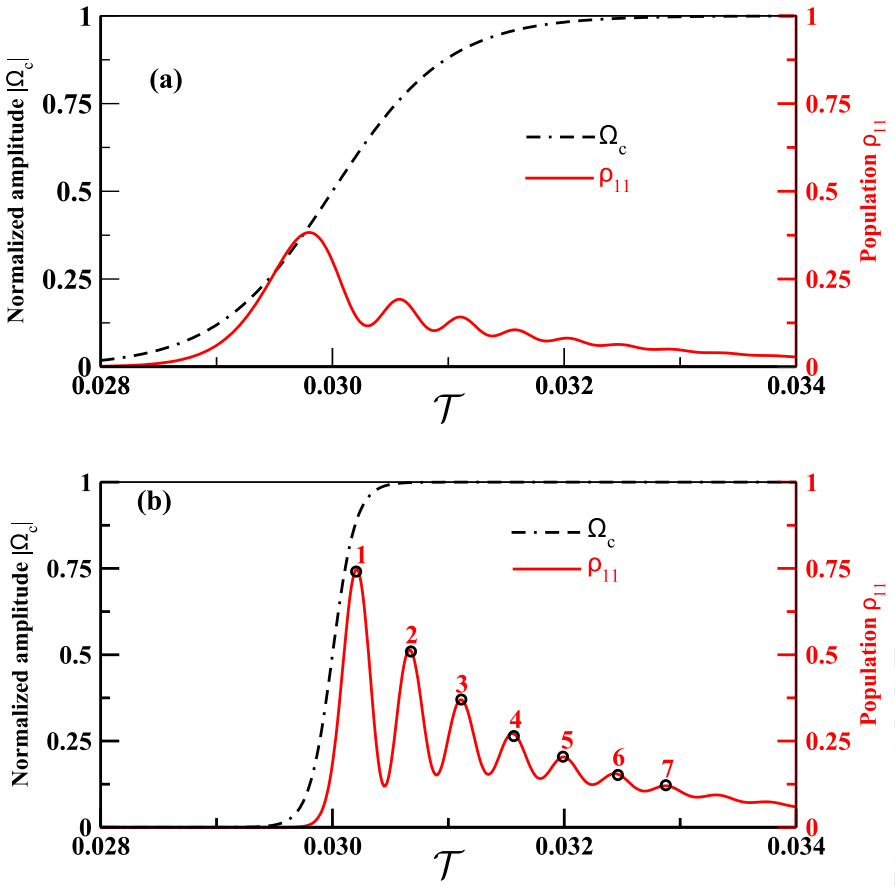

Figure A.3: The normalized field amplitude $|\Omega_c|$ and population ρ_{11} are plotted against normalized time $\mathcal{T}$ by numerically solving the density matrix equations for the three level Λ system given in chapter 2. The relevant parameters used are: $\Omega_c^0 = 7\gamma$, $\Omega_p^0 = 0.01\gamma$, and $\gamma_{23} = 0.001$. In Fig.A.3(a), $\alpha = 2$, representing a adiabatic switching on of the control field, whereas in Fig.A.3(b), $\alpha = 0.2$ representing non adiabatic switching on of the control field. The switching on time is $T_{on} = 30/\gamma$

of the initial time profile of control field at the entrance of the medium. Thus, at any given propagation distance inside the medium, the control field's leading end will mimic a non adiabatic rise in control field intensity, irrespective of how smoothly it is switched on at the entrance of the medium. Therefore, the oscillations in ρ_{11} is inevitable for the current system. Due to the oscillations in ρ_{11}, the generated probe field also oscillates in a similar manner as ρ_{11}. When the input control field amplitude is optimum, the amplitude and frequency of population oscillation in $|1\rangle$ is less pronounced, such that the corresponding small oscillations in the probe field envelope doesn't receive noticeable amplification. But with a larger control field amplitude, *e.g.*, $\Omega_c^0 = 7\gamma$, the amplification is large enough to amplify the oscillations in the probe field's envelope as shown in Fig. A.4. Figure A.4 shows the temporal profiles of the probe and control fields at a larger propagation distance $\mathcal{Z} = 4.5$, where the probe receives significant amplification with noisy oscillations. Upon zooming (inset of Fig. A.4), the probe can be seen oscillating in a similar manner as ρ_{11} in Fig. A.3(b). Such similarity between the oscillations of ρ_{11} and the probe envelope suggests that the modulation in probe amplitude is indeed due to the population oscillation in excited state $|1\rangle$.

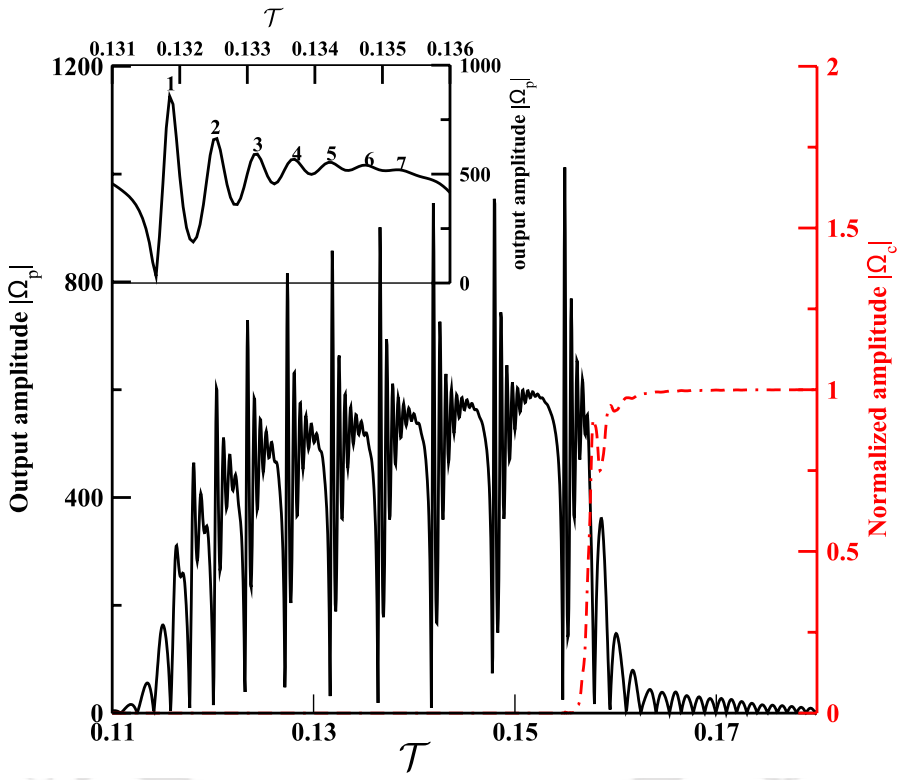

Figure A.4: Plot showing the output probe pulse for $\Omega_c^0 = 7\gamma$ at $\mathcal{Z} = 4.5$. The probe is amplified around 1000 times. Inset shows zoomed image of the probe field in the time interval, $0.131 < \mathcal{T} < 0.135$.

Appendix B

Appendix of chapter 5

B.1 Effect of inhomogeneous broadening

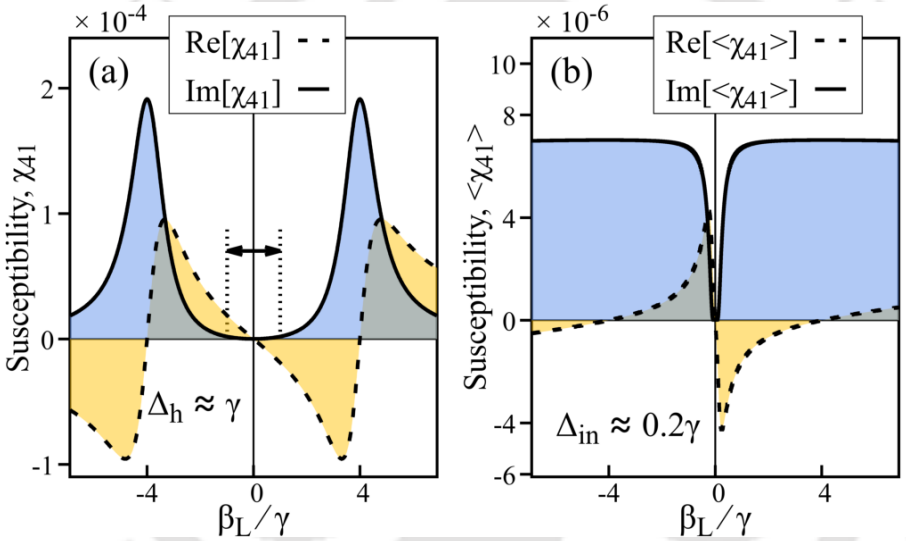

Figure B.1: (a),(b): Real and imaginary part of homogeneously broadened susceptibility, χ_{41} and Doppler averaged susceptibility, $< \chi_{41} >$ vs β_L/γ, respectively. Parameters used: Rabi frequencies, $\Omega_c = 4\gamma$, $\Omega_{R(L)} = 0.05\gamma$; detunings, $\delta_{p(c)} = 0$; decoherence rates, $\Gamma_{ij} \approx 10^{-3}\gamma$, $\Gamma_{i4} = 3/2\gamma$ $(i < j,\ i, j = 1, 2, 3)$; density of atoms, $\mathcal{N} = 2 \times 10^{10}$ cm^{-3}, temperature $T = 300$ K. Here, Δ_h and Δ_{in} represent the width of EIT window for homogeneous and inhomogeneous broadening, respectively.

The Doppler effect causes a laser frequency shit in the atom's rest frame, introducing a laser detuning of $\delta_i + \vec{k}_i.\vec{v}$ $[i = p(\text{probe}), c(\text{control})]$. Here, $\vec{v}$ and $\vec{k}_i$ are the velocity of the atom and wavevector of the laser, respectively. With the aforementioned modified detuning, the steady-state susceptibility, χ_{ij} are given by their average over the one-dimensional Maxwell-Boltzmann velocity distribution:

$$f(v)dv = \sqrt{\frac{M}{2\pi k_B T}} \exp\left(-\frac{Mv^2}{2k_B T}\right) dv, \tag{B.1}$$

where T is the temperature of the gas, M is the mass of each atom, and k_B is the Boltzmann constant. The velocity averaged susceptibilities are then given by $< \chi_{ij} >= \int_{-\infty}^{\infty} \chi_{ij}(v) f(v) dv$.

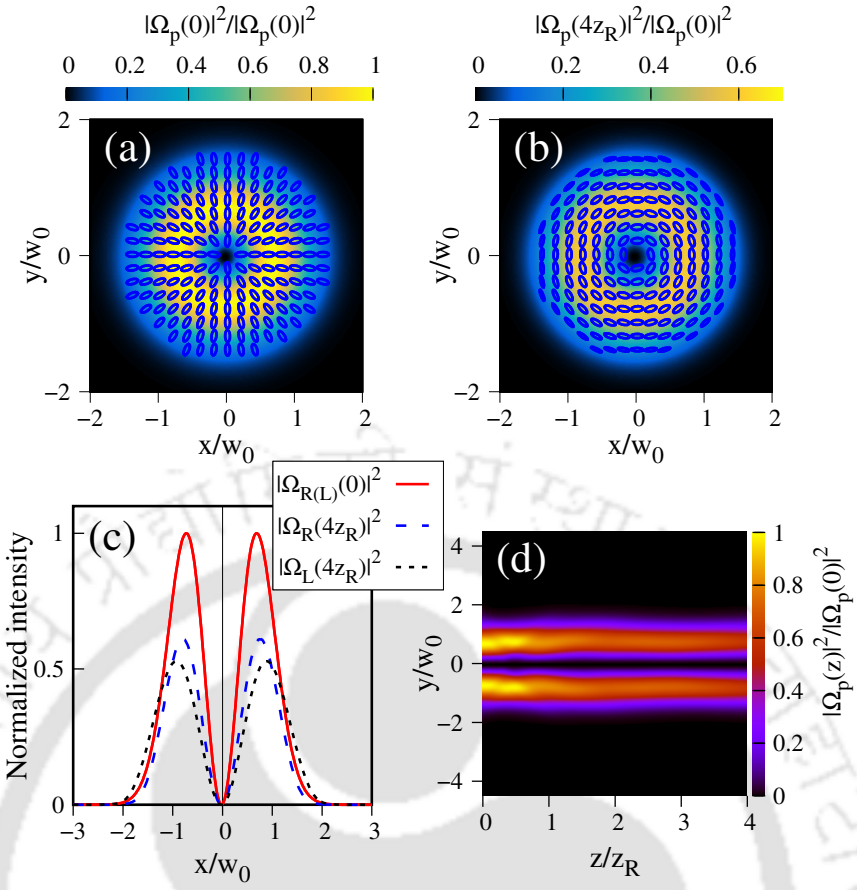

Figure B.2: (a), (b): Transverse intensity and polarization distribution of a CV beam ($l_L = -1$, $l_R = 1$, $\theta = \pi$, $\alpha = 3\pi/8$) at $z = 0$ and $z = 2z_R$, respectively. (c): Normalized intensity vs x/w_0. (d): Longitudinal intensity profile of the VB. Control field beam waist is taken to be w_0, where w_0 is the beam waist of the probe VB. The blue color ellipses in (a) and (b) represent right circular polarization. Parameters used: $\delta_c = 0.1\gamma$,$\delta_p = 0$, $\beta_L = 0.05\gamma$, $\Omega_c = 8\gamma$ with rest of the parameters same as Fig. B.1. Field amplitudes have been normalized with respect to the field amplitude at $z = 0$.

We consider a co-propagating geometry, with both probe and control fields propagating along the $+z$ direction, i.e., $\vec{k}_p/|\vec{k}_p| = \vec{k}_c/|\vec{k}_c| = \hat{z}$. Furthermore, for the control field detunings considered in chapter 5, the wavenumbers, $|\vec{k}_p| \approx |\vec{k}_c|$. As a result the two photon detuning in presence of inhomogeneous broadening becomes,

$$\begin{aligned}\tilde{\delta} &= \tilde{\delta}_p(\vec{v}) - \tilde{\delta}_c(\vec{v}) \\ &= \delta_p + \vec{k}_p.\vec{v} - (\delta_c + \vec{k}_c.\vec{v}) \\ &\approx \delta_p - \delta_c, \end{aligned} \tag{B.2}$$

which is the same as the two-photon detuning for homogeneous broadening. Thus, the copropagating geometry is preferable to reduce the effect of inhomogeneous broadening. In figures B.1(a) and B.1(b), the real and imaginary part of susceptibility, corresponding to the vector beam's right circularly polarized component for homogeneous and inhomogeneous broadening are plotted, respectively. In the case of inhomogeneous broadening, the width of the EIT window ($\Delta_{in} \approx 0.2\gamma$) shrinks as shown in Figs. [B.1(a), B.1(b)]. Furthermore, the magnitude of susceptibility for

inhomogeneous broadening is comparatively larger than homogeneous broadening as shown in in Figs. [B.1(a), B.1(b)]. Due to a very narrow EIT window in case of inhomogeneous broadening, the control field Rabi frequency needs to be larger say $\Omega_c = 8\gamma$, compared to $\Omega_c = 4\gamma$ as mentioned in Fig. B.1, in order to increase the EIT window width. This ensures absorption free guiding through the "core" of the optically written waveguide. The propagation results obtained by considering inhomogeneous broadening are curated in Fig. B.2. The simulation results suggest that vector beam guiding is also possible in the presence of inhomogeneous broadening as illustrated in Fig. B.2(a)-B.2(d) by choosing a larger value of control field Rabi frequency.

Bibliography

[1] P. A. M. Dirac, Proceedings of the Royal Society of London. Series A, Containing Papers of a Mathematical and Physical Character **114**, 243 (1927).

[2] R. P. Feynman, *Quantum Electrodynamics (advanced book classics)* (Springer Berlin Heidelberg, 2009).

[3] M. O. Scully and M. S. Zubairy, *Quantum Optics* (Cambridge University Press, 1997).

[4] D. Dalvit, P. Milonni, D. Roberts, and F. da Rosa, *Casimir Physics* (Springer, 2011).

[5] R. Loudon, *The quantum theory of light*, 3 ed. (Oxford University Press, 2000).

[6] S. Weinberg, *The quantum theory of Fields* (Cambridge University Press, 2005).

[7] C. Cohen-Tannoudji, J. Dupont-Roc, and G. Grynberg, *Atom—Photon Interactions* (John Wiley & Sons, Ltd, 1998).

[8] H.-A. Bachor and T. C. Ralph, *A Guide to Experiments in Quantum Optics*, 3 ed. (John Wiley & Sons, Ltd, 2019).

[9] J. D. Jackson, *Classical Electrodynamics*, 3 ed. (, 1998).

[10] P. W. Milonni and J. H. Eberly, *Laser Physics* (John Wiley & Sons, Inc., 1986).

[11] R. W. Boyd, *Nonlinear Optics*, 3 ed. (Academic Press, Burlington, 2008).

[12] H. Breuer, P. Breuer, F. Petruccione, and S. Petruccione, *The Theory of Open Quantum Systems* (Oxford University Press, 2002).

[13] P. Meystre and M. Sargent, *Elements of Quantum Optics*, 2 ed. (Springer Berlin, Heidelberg, 1991).

[14] L. Allen and J. Eberly, *Optical Resonance and Two-level Atoms*Dover books on physics and chemistry (Dover, 1987).

[15] M. Fleischhauer, A. Imamoglu, and J. P. Marangos, Rev. Mod. Phys. **77**, 633 (2005).

[16] K.-J. Boller, A. Imamoğlu, and S. E. Harris, Phys. Rev. Lett. **66**, 2593 (1991).

[17] G. Alzetta, L. Moi, and G. Orriols, Il Nuovo Cimento B (1971-1996) **52**, 209 (1979).

[18] E. Arimondo, V coherent population trapping in laser spectroscopy, , Progress in Optics Vol. 35, pp. 257–354, Elsevier, 1996.

[19] S. Schiemann, A. Kuhn, S. Steuerwald, and K. Bergmann, Phys. Rev. Lett. **71**, 3637 (1993).

[20] E. S. Fry *et al.*, Phys. Rev. Lett. **70**, 3235 (1993).

[21] S. Knappe *et al.*, Applied Physics Letters **85**, 1460 (2004).

[22] S. H. Autler and C. H. Townes, Phys. Rev. **100**, 703 (1955).

[23] W. T. Silfvast, *Laser Fundamentals*, 2 ed. (Cambridge University Press, 2004).

[24] K. W. Madison, Y. Wang, A. M. Rey, and K. Bongs, *Annual Review of Cold Atoms and Molecules* (World Scientific, 2013).

[25] M. O. Scully, Physics Reports **219**, 191 (1992).

[26] M. O. Scully, Phys. Rev. Lett. **67**, 1855 (1991).

[27] U. Rathe, M. Fleischhauer, S.-Y. Zhu, T. W. Hänsch, and M. O. Scully, Phys. Rev. A **47**, 4994 (1993).

[28] A. Wilson-Gordon and H. Friedmann, Optics Communications **94**, 238 (1992).

[29] M. Fleischhauer *et al.*, Phys. Rev. A **46**, 1468 (1992).

[30] M. Fleischhauer, C. Keitel, M. Scully, and C. Su, Optics Communications **87**, 109 (1992).

[31] Q. Zhan, Adv. Opt. Photon. **1**, 1 (2009).

[32] A. M. Beckley, T. G. Brown, and M. A. Alonso, Opt. Express **18**, 10777 (2010).

[33] L. Allen, M. W. Beijersbergen, R. J. C. Spreeuw, and J. P. Woerdman, Phys. Rev. A **45**, 8185 (1992).

[34] A. M. Yao and M. J. Padgett, Adv. Opt. Photon. **3**, 161 (2011).

[35] G. Fischer, *Mathematical Models: Photograph Volume and Commentary (Advanced Lectures in Mathematics Series)* (Friedrick Vieweg & Son, 1986).

[36] Ruchi, P. Senthilkumaran, and S. K. Pal, International Journal of Optics **2020**, 2812803 (2020).

[37] Y. Kozawa and S. Sato, Chapter two - small focal spot formation by vector beams, , Progress in Optics Vol. 66, pp. 35–90, Elsevier, 2021.

[38] R. Dorn, S. Quabis, and G. Leuchs, Phys. Rev. Lett. **91**, 233901 (2003).

[39] T. A. Klar and S. W. Hell, Opt. Lett. **24**, 954 (1999).

[40] P. Török and P. Munro, Opt. Express **12**, 3605 (2004).

[41] K. S. Youngworth and T. G. Brown, Opt. Express **7**, 77 (2000).

[42] S. N. Khonina and I. Golub, J. Opt. Soc. Am. A **29**, 1470 (2012).

[43] V. G. Niziev and A. V. Nesterov, Journal of Physics D: Applied Physics **32**, 1455 (1999).

[44] Q. Zhan, Journal of Optics A: Pure and Applied Optics **5**, 229 (2003).

[45] Q. Zhan, Trapping nanoparticles with cylindrical polarization, in *Optical Trapping and Optical Micromanipulation*, edited by K. Dholakia and G. C. Spalding Vol. 5514, pp. 275 – 282, International Society for Optics and Photonics, SPIE, 2004.

[46] F. Castellucci, T. W. Clark, A. Selyem, J. Wang, and S. Franke-Arnold, Phys. Rev. Lett. **127**, 233202 (2021).

[47] S. Qiu *et al.*, Photon. Res. **9**, 2325 (2021).

[48] V. Parigi *et al.*, Nature Communications **6**, 7706 (2015).

[49] C. Gabriel *et al.*, Phys. Rev. Lett. **106**, 060502 (2011).

[50] T. Giordani *et al.*, Phys. Rev. Lett. **122**, 020503 (2019).

[51] E. Karimi *et al.*, Phys. Rev. A **82**, 022115 (2010).

[52] G. Milione *et al.*, Opt. Lett. **40**, 1980 (2015).

[53] G. Milione, H. I. Sztul, D. A. Nolan, and R. R. Alfano, Phys. Rev. Lett. **107**, 053601 (2011).

[54] W. J. Firth and D. V. Skryabin, Phys. Rev. Lett. **79**, 2450 (1997).

[55] A. S. Desyatnikov and Y. S. Kivshar, Phys. Rev. Lett. **87**, 033901 (2001).

[56] Z.-H. Zhu *et al.*, Applied Physics Letters **112**, 161103 (2018).

[57] M. S. Bigelow, P. Zerom, and R. W. Boyd, Phys. Rev. Lett. **92**, 083902 (2004).

[58] Y. V. Izdebskaya, J. Rebling, A. S. Desyatnikov, and Y. S. Kivshar, Opt. Lett. **37**, 767 (2012).

[59] F. Bouchard *et al.*, Phys. Rev. Lett. **117**, 233903 (2016).

[60] J. T. Mok and B. J. Eggleton, Nature **433**, 811 (2005).

[61] R. W. Boyd, Journal of Modern Optics **56**, 1908 (2009).

[62] C. Manzoni *et al.*, Laser & Photonics Reviews **9**, 129 (2015).

[63] O. Kocharovskaya and P. Mandel, Phys. Rev. A **42**, 523 (1990).

[64] M. Fleischhauer and M. D. Lukin, Phys. Rev. Lett. **84**, 5094 (2000).

[65] N. V. Vitanov, A. A. Rangelov, B. W. Shore, and K. Bergmann, Rev. Mod. Phys. **89**, 015006 (2017).

[66] E. Arimondo, *V Coherent Population Trapping in Laser Spectroscopy*, Progress in Optics Vol. 35 (Elsevier, 1996).

[67] G. S. Agarwal and T. N. Dey, Laser & Photonics Reviews **3**, 287 (2009).

[68] S. E. Harris and A. V. Sokolov, Phys. Rev. Lett. **81**, 2894 (1998).

[69] R. K. V. and T. N. Dey, Phys. Rev. A **94**, 053851 (2016).

[70] H. Murata, A. Morimoto, T. Kobayashi, and S. Yamamoto, IEEE Journal of Selected Topics in Quantum Electronics **6**, 1325 (2000).

[71] S. Harris, J. Macklin, and T. Hansch, Optics Communications **100**, 487 (1993).

[72] S. L. McCall and E. L. Hahn, Phys. Rev. **183**, 457 (1969).

[73] S. L. McCall and E. L. Hahn, Phys. Rev. Lett. **18**, 908 (1967).

[74] M. J. Konopnicki and J. H. Eberly, Phys. Rev. A **24**, 2567 (1981).

[75] R. Grobe, F. T. Hioe, and J. H. Eberly, Phys. Rev. Lett. **73**, 3183 (1994).

[76] J. H. Eberly, Quantum and Semiclassical Optics: Journal of the European Optical Society Part B **7**, 373 (1995).

[77] A. Rahman and J. H. Eberly, Phys. Rev. A **58**, R805 (1998).

[78] Q.-H. Park and H. J. Shin, Phys. Rev. A **57**, 4643 (1998).

[79] A. Rahman, Phys. Rev. A **60**, 4187 (1999).

[80] G. S. Agarwal and J. H. Eberly, Phys. Rev. A **61**, 013404 (1999).

[81] G. Vemuri, G. S. Agarwal, and K. V. Vasavada, Phys. Rev. Lett. **79**, 3889 (1997).

[82] T. P. Ogden *et al.*, Phys. Rev. Lett. **123**, 243604 (2019).

[83] A. B. Matsko *et al.*, *Slow, Ultraslow, Stored, and Frozen Light*, Advances In Atomic, Molecular, and Optical Physics Vol. 46 (Academic Press, 2001).

[84] S. E. Harris, Phys. Rev. Lett. **70**, 552 (1993).

[85] D. Sun, Z.-E. Sariyanni, S. Das, and Y. V. Rostovtsev, Phys. Rev. A **83**, 063815 (2011).

[86] H. Tanaka *et al.*, Phys. Rev. A **68**, 053801 (2003).

[87] L. J. Wang, A. Kuzmich, and A. Dogariu, Nature **406**, 277 (2000).

[88] G. S. Agarwal, T. N. Dey, and S. Menon, Phys. Rev. A **64**, 053809 (2001).

[89] B. D. Clader and J. H. Eberly, Phys. Rev. A **78**, 033803 (2008).

[90] A. Eilam and A. D. Wilson-Gordon, Phys. Rev. A **98**, 013808 (2018).

[91] H. R. Hamedi, J. Ruseckas, and G. Juzeliūnas, Journal of Physics B: Atomic, Molecular and Optical Physics **50**, 185401 (2017).

[92] K. Tai, A. Hasegawa, and A. Tomita, Phys. Rev. Lett. **56**, 135 (1986).

[93] G. P. Agrawal, Phys. Rev. Lett. **59**, 880 (1987).

[94] K. J. Jiang, L. Deng, and M. G. Payne, Phys. Rev. A **74**, 041803(R) (2006).

[95] H.-j. Li, C. Hang, G. Huang, and L. Deng, Phys. Rev. A **78**, 023822 (2008).

[96] D. Strickland and G. Mourou, Optics Communications **56**, 219 (1985).

[97] S. E. Harris and Z.-F. Luo, Phys. Rev. A **52**, R928 (1995).

[98] M. A. Kmetic and W. J. Meath, Physics Letters A **108**, 340 (1985).

[99] R. Bavli, D. F. Heller, and Y. B. Band, Phys. Rev. A **41**, 3960 (1990).

[100] O. Calderon, R. Gutierrez-Castrejon, and J. Guerra, IEEE Journal of Quantum Electronics **35**, 47 (1999).

[101] P. Hu, Y. Niu, X. Wang, S. Gong, and C. Liu, Journal of Optics **18**, 095504 (2016).

[102] R. Bavli, D. F. Heller, and Y. B. Band, The Journal of Chemical Physics **91**, 6714 (1989).

[103] F. Zhou, Y. Niu, and S. Gong, The Journal of Chemical Physics **131**, 034105 (2009).

[104] N. Singh, Q. V. Lawande, R. D Souza, and B. N. Jagatap, The Journal of Chemical Physics **137**, 104309 (2012).

[105] A. Mishra and B. N. Jagatap, Journal of Modern Optics **67**, 823 (2020).

[106] A. Brown, Chemical Physics **342**, 16 (2007).

[107] L. Deng, Y. Niu, and S. Gong, Phys. Rev. A **98**, 063830 (2018).

[108] Q. Du, C. Hang, and G. Huang, J. Opt. Soc. Am. B **31**, 594 (2014).

[109] J.-Y. Zhao, L.-G. Qin, X.-M. Cai, Q. Lin, and Z.-Y. Wang, Chinese Physics B **25**, 044202 (2016).

[110] M. Sahrai, M. Minaee-Yazdi, S. Ahmadi-Kandjani, and R. Kheradmand, The European Physical Journal D **73**, 217 (2019).

[111] M. Macovei, M. Mishra, and C. H. Keitel, Phys. Rev. A **92**, 013846 (2015).

[112] S. H. Asadpour and H. R. Soleimani, J. Opt. Soc. Am. B **31**, 3123 (2014).

[113] W. J. Meath and E. A. Power, Molecular Physics **51**, 585 (1984).

[114] J. M. Bowman, S. Irle, K. Morokuma, and A. Wodtke, The Journal of Chemical Physics **114**, 7923 (2001).

[115] G. J. Harris, O. L. Polyansky, and J. Tennyson, Spectrochimica Acta Part A: Molecular and Biomolecular Spectroscopy **58**, 673 (2002).

[116] J. P. Lavoine, The Journal of Chemical Physics **127**, 094107 (2007).

[117] E. A. Wilson, N. B. Manson, C. Wei, and Y. Li-Jun, Phys. Rev. A **72**, 063813 (2005).

[118] H. Li *et al.*, Phys. Rev. A **80**, 023820 (2009).

[119] A. Eilam, A. D. Wilson-Gordon, and H. Friedmann, Opt. Lett. **34**, 1834 (2009).

[120] S. Davuluri and Y. Rostovtsev, Phys. Rev. A **88**, 053847 (2013).

[121] J. Korociński, A. Raczyński, J. Zaremba, and S. Zielińska-Kaniasty, J. Opt. Soc. Am. B **30**, 1517 (2013).

[122] A. Raczyński, J. Zaremba, and S. Zielińska-Raczyńska, J. Opt. Soc. Am. B **31**, 2965 (2014).

[123] D. V. Kosachiov, B. G. Matisov, and Y. V. Rozhdestvensky, Journal of Physics B: Atomic, Molecular and Optical Physics **25**, 2473 (1992).

[124] D. Budker *et al.*, Rev. Mod. Phys. **74**, 1153 (2002).

[125] D. Petrosyan and Y. P. Malakyan, Phys. Rev. A **70**, 023822 (2004).

[126] C. J. Gibson, P. Bevington, G.-L. Oppo, and A. M. Yao, Phys. Rev. A **97**, 033832 (2018).

[127] D. Luo *et al.*, Journal of Optics **22**, 115612 (2020).

[128] L. Stern, A. Szapiro, E. Talker, and U. Levy, Opt. Express **24**, 4834 (2016).

[129] B. Wen, G. Rui, J. He, Y. Cui, and B. Gu, Journal of Optics **22**, 085501 (2020).

[130] N. Radwell, T. W. Clark, B. Piccirillo, S. M. Barnett, and S. Franke-Arnold, Phys. Rev. Lett. **114**, 123603 (2015).

[131] A. G. Truscott, M. E. J. Friese, N. R. Heckenberg, and H. Rubinsztein-Dunlop, Phys. Rev. Lett. **82**, 1438 (1999).

[132] T. N. Dey and J. Evers, Phys. Rev. A **84**, 043842 (2011).

[133] L. Zhang, T. N. Dey, and J. Evers, Phys. Rev. A **87**, 043842 (2013).

[134] S. Sharma and T. N. Dey, Phys. Rev. A **96**, 053813 (2017).

[135] P. K. Vudyasetu, D. J. Starling, and J. C. Howell, Phys. Rev. Lett. **102**, 123602 (2009).

[136] O. N. Verma and T. N. Dey, Phys. Rev. A **89**, 033830 (2014).

[137] S. Boscolo and C. Finot, Optics & Laser Technology **131**, 106439 (2020).

[138] B. P. da Silva, B. A. D. Marques, R. B. Rodrigues, P. H. S. Ribeiro, and A. Z. Khoury, Phys. Rev. A **103**, 063704 (2021).

[139] T. Giordani *et al.*, Phys. Rev. Lett. **124**, 160401 (2020).

[140] T. A. Laine and S. Stenholm, Phys. Rev. A **53**, 2501 (1996).

List of publications

- Nilamoni Daloi and Tarak Nath Dey, "Shape-preserving atomic pulse amplifier," J. Opt. Soc. Am. B **38**, 3712-3722 (2021).
- Nilamoni Daloi, Partha Das, Tarak Nath Dey, "Pulse amplification in a closed-loop Λ system with permanent dipole moments", J. Opt. **24** 074001 (2022).
- Nilamoni Daloi and Tarak Nath Dey, "Vector beam polarization rotation control using resonant magneto optics," Opt. Express **30**, 21894-21905 (2022)
- Nilamoni Daloi, Pardeep Kumar, and Tarak Nath Dey, "Guiding and polarization shaping of vector beam in anisotropic media," Phys. Rev. A **105**, 063714 (2022)

Conferences and schools attended

- **SERB School on Frontiers in Quantum Optics**, Organized by the dept. of physics, IIT Guwahati during 1-19 December 2017.
- **Student Conference on Advances in Optics (SCAO)** 2021 held online from TIFR Mumbai on the 4^{th} and 5^{th} of February,2021: We were fortunate to have secured the best poster award.
- **Structured Light and Spin-Orbit Photonics (SLSOP)** 2022 held offline from 29 November 2022 to 2 December 2022, at ICTS Bengaluru, India.